Resonances and Collisions in Circumstellar Debris Discs with an Embedded Planet

Dissertation

zur Erlangung des akademischen Grades

doctor rerum naturalium (Dr. rer. nat.)

seit 1558

vorgelegt dem Rat der Physikalisch-Astronomischen Fakultät
der Friedrich-Schiller-Universität Jena

von Dipl. Phys. Martina Queck
geb. am 15.10.1980 in Halle/Saale

Gutachter:

1. Prof. Dr. Alexander V. Krivov
   Friedrich-Schiller-Universität Jena

2. Prof. Dr. Hervé Beust
   Universite Joseph Fourier, Grenoble (F)

3. Prof. Dr. Hans Scholl
   Observatoire de la Côte d'Azur, Nizza (F)

Tag des Rigorosums: 25. April 2008

Tag der öffentlichen Verteidigung: 29. Mai 2008

Contents

" Aber die Kristallschale, an die der Jupiter angeheftet ist?"

" Ja, wo ist sie jetzt? Wie kann der Jupiter angeheftet sein, wenn andere Sterne um ihn kreisen? Da ist keine Stütze im Himmel, da ist kein Halt im Weltall! Da ist eine andere Sonne!"

B. Brecht, Leben des Galilei

Zusammenfassung

Diese Arbeit behandelt theoretische Modelle zirkumstellarer Trümmerscheiben. Hauptaugenmerk ist die Kombination von strukturbildenden Bahnresonanzen (mean motion resonances) eines Planeten mit zirkumstellaren Kleinkörpern und strukturausgleichenden Kollisionen zwischen letzteren. Es wird untersucht, ob und in welchem Maße Resonanzen das Kollisionsverhalten beeinflussen. Hierzu werden anstelle der oft üblichen, rechenaufwendigen N-Teilchen-Simulation statistische Methoden verwendet, insbesondere die Kinetische Theorie. Diese bedarf eines höheren mathematisch-analytischen Aufwandes, kommt aber mit vergleichsweise geringem Rechenaufwand aus.

Im ersten Teil werden Kollisionsgeschwindigkeiten und -raten für abstrakte, zirkumstellare Trümmerscheiben betrachtet. Abstrakt vor allem deswegen, da verschiedene Bahnelemente der Übersichtlichkeit halber als gleichverteilt angenommen werden, obwohl Beobachtungen anderes nahelegen. Hauptaugenmerk ist hier jedoch nicht die Untersuchung konkreter, beobachteter Scheiben, sondern liegt vielmehr in der Ermittlung und möglichst klaren Darstellung des Einflußes einer Bahnresonanz auf das Kollisionsverhalten. Es zeigt sich, daß dieser sehr viel geringer als erwartet ausfällt. Die Änderungen der Kollisionsgeschwindigkeit durch eine Resonanz, auch eine sehr starke, sind vernachlässigbar klein. Die Kollisionsrate wird stärker beeinflußt. Sie zeigt ein hochgradig nichtlineares Verhalten und entwickelt insbesondere ein Maximum. Aber auch in starken Resonanzen erhöht sie sich um weniger als das 4-fache.

Im zweiten Teil der Arbeit werden zwei Modelle zur Erkärung der in Trümmerscheiben beobachteten Strukturen entwickelt und verglichen. Eines, welches auf dem Transport kleiner Staubteilchen durch Zugkräfte des Poynting-Robertson-Effektes und des Sternenwindes beruht und ein anderes, das auf kaskadenartigen Kollisionen von in der Resonanz gefangenen Planetesimalen beruht. Beide Modelle sind analytischer Form, sie berücksichtigen die wesentlichen Prozesse, werden dabei aber so einfach wie möglich gehalten. Es zeigt sich, daß die Effizienz des ersten Szenarios wesentlich vom quantitativ nur schwer faßbaren stellaren Wind abhängt. Szenario II hingegen wird bestimmt von den Details des Kollisionsprozesses sowie der gesamten Kaskade.

Mit den derzeit zur Verfügung stehenden Beobachtungsdaten ist es nicht möglich, klar zu unterscheiden, ob die beobachteten Strukturen in den zirkumstellaren Scheiben eher nach dem ersten oder eher nach dem zweiten Modell entstehen.

Abstract

This work considers theoretical models of circumstellar debris discs. The main focus is the combination of mean motion resonances between a planet and circumstellar small bodies, which create structures, and collisions among the small bodies, which smear the structures out. It is examined to what degree resonances do influence the collisional behaviour. Instead of the often applied, computer-intensive N-body-simulations we make use of statistical methods, especially the kinetic theory. This requires more effort on the mathematical-analytical side, but involves comparably low computational expense.

In the first part collisional velocities and rates for hypothetical circumstellar debris discs are investigated. Hypothetical especially in the sense that several orbital elements are assumed to be distributed uniformly for simplicity, although observations suggest otherwise. The main focus here is not the analysis of certain, observed discs, but instead the investigation and representation of the influence of a mean motion resonance on the collisional behaviour. The results show, that this influence is much smaller than exspected. The changes of the collisional velocity due to resonance, even a very strong one, are negligibly small. The collisional rate is influenced more strongly. It shows a highly nonlinear dependence and especially develops a maximum. But even for a very strong resonance it increases by less than a factor of 4.

In the second part of this work two models aiming to explain the structures observed in debris discs are developed and compared. One which is based upon the transport of small dust grains by Poynting-Robertson and stellar wind drag forces, and one which is based upon cascade-like collisions of planetesimals residing in a resonance. Both models are analytical ones, they take into consideration the most important effects while being kept as simple as possible at the same time. It turns out that the efficiency of the first scenario depends heavily on the stellar wind, which is most difficult to quantify. Scenario II is determined by the details of the collisional process and the whole collisional cascade.

With the experimental and observational data available today it is not possible to determine if the structures in circumstellar discs originate from the first scenario or second one.

Acknowledgements

Chapter 1

Introduction

Circumstellar discs are nowadays known to be a common phenomenon for a great variety of stars. Which is not surprising, since according to the theory of star formation, stars are born within accretion discs (Strom, 1993). Those accretion discs then give rise to planetary systems. Around young stars with ages below 10 million years planet formation is still going on and the discs are therefore called protoplanetary ones (Safronov, 1969; Marcy et al., 2000). At about 3 to 10 million years planet formation is concluded and the gas of the disc dispersed (Bouwman et al., 2006). It leaves behind a main-sequence star with a disc of small bodies and dust and possibly planets surrounding the star. In its primordial phase the dust disc is still massive, but 10 to 60 million years later it is diminished to a faint, optical thin, so called 'debris disc' (Jewitt, 1994). Due to a violent, perturbative event or by simple aging of the disc the star can be deprived of its circumstellar material. Surveys of Sun-like stars in the Milky Way indicate debris discs around 10% to 20% of them (Decin et al., 2000; Meyer et al., 2007).

All of the spatially resolved discs, today about 14 of them (Meyer et al., 2007), show different kinds of asymmetries and structures such as inner gaps, warps or clumps (Augereau, 2004). The structures might have different origins: on the one hand singular events, e.g. a fly-by of another star (Kalas et al., 2001) or break-up of a large asteroid (Grigorieva et al., 2007), and on the other hand regularly recurring events, such as perturbation by a planet residing in the disc (Mouillet et al., 1997; Liou & Zook, 1999). There have been several attempts to explain observed structures by planetary perturbation quantitatively (e.g. Quillen & Thorndike, 2002; Deller & Maddison, 2005; Wyatt, 2006). Unfortunately the interaction between circumstellar discs and planets is not well known. Mostly due to the only a small overlap of the set of stars observed in search for discs with the set of stars observed in search for planets. That originates from the different observational techniques applied. The search for planets is undertaken by radial velocity measurements, direct imaging or transit observations. The radial velocity method is not hindered by circumstellar discs, it finds, however, large and close-in planets, planets too close to the star to be connected to discs observable today. The direct imaging intrinsically only works for young and thus bright planets around young stars, which do not host a debris disc due to

their age. Transits, finally, would be obscured by pronounced discs, ergo for any observed transit, there is no significant surrounding disc. Therefore most exoplanet host stars are discless (Greaves et al., 2004; Beichman et al., 2005; Moro-Martín et al., 2007; Fiedler, 2007).

Observation of debris discs, on the other hand, is done by the search for emission around a star in the visible (Hubble Space Telescope) as well as infrared (Spitzer Space Telescope), submillimetre (SCUBA at James Clerk Maxwell Telescope) and even millimetre (IRAM at Plateau de Bure interferometer) wavelength region. In the visible wavelengths the scattered light from the dust grains is observed. With the debris discs being dilute the measured flux is relatively small here, although there are some exceptions for the denser ones of the debris discs (e.g. Heap et al., 2000). Most of the information about discs and their structure is obtained in the far-infrared and sub-millimetre wavelengths. Compare e.g. Holland et al. (1998) and Su et al. (2005) for the observation of the Vega disc. Since the spatial resolution of any optical instrument is proportional to $1/\lambda$, the spatial resolution of the disc images taken in long wavelengths is low and only discs several ten AU from the star and large scale structures can be seen.

In very recent observations there have been attempts to observe discs by interferometry thus getting close enough to the star, as to be in the radial-velocity-region. For example, the inner disc of Vega was observed by Absil et al. (2006) with CHARA/FLUOR at Mount Wilson Observatory.

Although not very many, there do exist several stars known to host both planets and a disc. First of all our Solar System – 8 planets plus the Edgeworth-Kuiper Belt. But also other stars, e.g. HD 82943 (Beichman et al., 2005), HD 38529 (Moro-Martín et al., 2007) or HD 69830 (Beichman et al., 2005; Lovis et al., 2006). And last, but not least, ϵ Eridani, where there is an inner planet observed by radial velocity measurements (Hatzes et al., 2000) and a much further out debris disc with quite sophisticated structure in submillimetre observations (Greaves et al., 1998, 2005).

Most of the explanations proposed for the origin of the observed structures in the discs consider the latter as a disc of individual particles, where each single grain is treated separately, and make so called N-body simulations. Those models are not able to treat the collisional interaction within the disc (Liou & Zook, 1999; Kuchner & Holman, 2003; Deller & Maddison, 2005). On the other hand, if the collisions are modelled, then the discs are assumed to be rotationally symmetric and undisturbed (Krivov et al., 2006; Thébault & Augereau, 2007).

A model more realistic from the physical point of view needs to take into consideration both the asymmetries and the collisions and thus descibe a perturbed and at the same time colliding disc.

Chapter 2

Background

This chapter will provide the basic facts and background knowledge about debris discs in general, resonances in special and give a short overview of collisional dynamics necessary for the analysis we are going to perform in the following chapters.

2.1 Debris Discs

2.1.1 Nomenclature

A debris disc, in the frame of this work, consists of dust and small bodies as well as planetesimals.

We call the smallest solid bodies of a size of about or below $1\mu m$ dust, small bodies are labelled those with a size up to $1m$, planetesimals those of the order of $1km$, planets are the largest, circumstellar bodies and hundreds of kilometres in diameter, they have their own gravitational field, sufficient to make long-term influences on the other components. The numerical limits are a matter of convention, they should not be taken as sharp boundaries, but rather understood as a rough orientation in the orders of magnitude.

2.1.2 Origin

According to the theory, debris discs are a by-product of star – and possible planet – formation. Therein a cloud of interstellar gas starts to collapse after a destabilizing perturbation, it fragments, and creates a protostar. The latter accretes from its surrounding envelope and this way develops into a real, "adult" star. Due to angular momentum preservation the envelope flattens and after the star's accretion phase remains as a circumstellar disc. Because this disc may give rise to one or more planets it is called a protoplanetary one. Within the disc star formation repeats itself en miniature, there are instabilities, accretion and chemical processes leading to the growths of smaller and larger grains, later on planetesimals and finally planets. After about 10^7 years most of the original gas has been used up in such processes, the rest is erased from the disc by

photoevaporation, radiation pressure and other dissipative processes and leaves behind a developed, "adult" disc consisting of, not necessarily planets, but definitely small, solid bodies and dust grains.

Therefore, according to the theory of their formation *every* star should own a disc.

But even after the conclusion of planet formation the disc is subject to further development. The solid components tend to collide and break each other up into smaller pieces. Thus they create a collisional cascade leading to a grinding of particles from kilometre to micrometre size. Due to radiation pressure the submicron particles are no longer bound to the primary and leave the system as β-meteoroids.

The collisional cascade permanently creates new small particles and thus steadily replenishes the dust disc and makes it a long lived one. But once all the large parent bodies have been broken down the disc will diminish and leave a disc-less star behind. In addition to this aging process the disc can also be destructed by strong perturbations e.g. from a stellar fly-by or tumbling of the disc in a multiple star system.

2.1.3 Dynamics

While in a planetary system the star harbours most of the mass and the planets the angular momentum, the small bodies and dust cover most of the area and are by far the most numerous.

Dynamically the system is dominated by the gravitational force of the primary, which compels the other bodies to Keplerian orbits around it.

However, the star not only creates the gravitational field in which the disc particles move it also emits the products of its hydrogen burning. First there is the radiation, which illuminates the disc but also carries momentum. When hit by a photon coming from the star any body is accelerated away from the latter. The thus executed force, the so called radiation pressure, is given as

$$\mathbf{F}_{\text{rad}} = \frac{I}{c} \mathfrak{A} \frac{\mathbf{r}}{r}, \tag{2.1}$$

where $\mathfrak{A}$ is the illuminated area, I the flux irradiated onto $\mathfrak{A}$ and c the speed of light. I depends on the angular size of $\mathfrak{A}$ with respect to the star and therefore is a function of distance to the star, $I = f(r) \sim r^{-2}$. So the radiation pressure can be characterized by the dimensionless and distance independent β-ratio

$$\beta := \frac{F_{\text{rad}}}{F_{\text{grav}}} \tag{2.2}$$

and be included into the treatment of the disc in the simple reduction of the effective stellar mass,

$$M_{\text{effective}} = (1 - \beta) M_* . \tag{2.3}$$

Somewhat more tricky is the so called Poynting-Robertson drag. This is an effect of motion through a radiation field. The star emits the radiation isotropically and radially.

But the dust grains are orbiting it, meaning there is a tangential velocity of the dust with respect to the stream of photons. So the stellar radiation hits the dust sideways instead of radially and this in turn leads to friction and deceleration of the dust. In principle the PR effect can be compared to motion in a viscous medium. The strength of the effect is not a function of distance to the star only, but fundamentally depends on the dust grains' orbital velocity. It is given by

$$\mathbf{F}_{\mathrm{PR}} = -\frac{I}{c}\mathfrak{A}\,\frac{\mathbf{v}}{c}\ .$$ (2.4)

Contrary to F_{rad} F_{PR} is not directed along the position but the velocity vector and thus not parallel to the gravity. Consequently it cannot be rewritten in an "effective" formula like (2.3).

With both radiation pressure and Poynting-Robertson drag being relativistic forces, the flux in (2.1) and (2.4) is a special-relativistic one. Let I_0 be the intensity felt by a particle at rest and v_r its radial velocity then the intensity felt by an moving particle is

$$I = I_0\,\sqrt{1-\frac{v_r^2}{c^2}} \approx I_0\left(1-\frac{v_r^2}{2\,c^2}\right) \qquad \text{for } v_r \ll c\ .$$

The strength of both radiative forces is proportional to the size of the particle it acts upon. If s is the latter's diameter both forces grow with s^2, meaning the larger the particle the stronger their effects. On the other hand, the gravitational force is also at work and a function of the particle size, it is proportional to the mass which is density $\times$ volume. The volume, however, grows with s^3. So obviously only for small particles will radiative forces and gravity be comparable. The larger the particles become the more dominant the gravitational influence will be.

In conclusion we have to consider radiation pressure and PR drag only for the smallest bodies in the debris disc, for larger asteroids or even planets, they can be neglected.

The small bodies and especially the dust grains are also affected by the stellar wind, meaning the stream of particles emitted from the star, such as protons, electrons, or α-particles. It causes a further friction and deceleration of the particles. Depending on the activeness of the star this effect might be as strong as the PR drag. It is the one most difficult to quantify since the stellar wind can only be observed indirectly by X-ray scattering, and might lead to contradicting results, compare Augereau & Beust (2006) to Strubbe & Chiang (2006), who found two mass-loss rates, differing by a factor of 30, for one and the same star.

All these radiation and drag forces are functions of the particle size, but depend heavily on characteristics of the host star, its mass, luminosity or mass-loss rate.

We will consider PR and wind drag in more detail later.

2.1.4 Observation

There are two basic means of observing populations of dust. First is the scattered light from the star. This can in principle be observed in any wavelength the star emits in. But
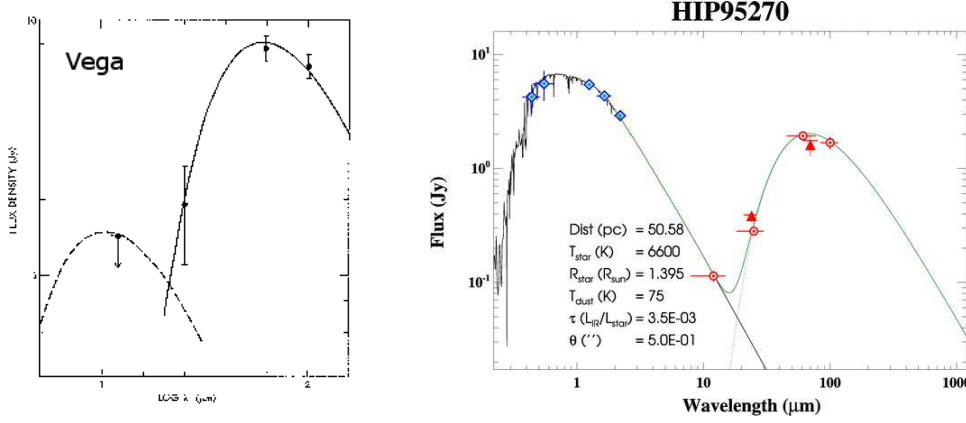
Figure 2.1: Spectra of two debris discs. Left: Vega's disc, the first one ever discovered. The star itself is not plotted here (Aumann et al., 1984). Right: Hipparcos star HIP95270 with a very prominent infrared excess from its debris disc (Rhee et al., 2007).

the light scattered by the dust is much more faint than that coming dircetly from the star, which is why coronographic or interferometric observations are the only sensible ones.

The second means of observing dust is via its thermal emission. As the dust is constantly heated by the star it has a certain temperature T_{dust} larger that 0 K, but considerably smaller than the stars effective temperature $T_{\mathrm{effective}}$. According to Planck's law

$$B_\lambda(T) \quad = \quad \frac{2hc^2}{\lambda^5} \frac{1}{e^{hc/kT\lambda} - 1} \tag{2.5}$$

it will emit continuous radiation with a maximum at $\lambda_{\mathrm{max}} = f(T)$.

That is why in the case of a star with a disc its spectrum will not only show the stars' characteristic lines, the maximum in its continuum at $\lambda_{\mathrm{max}}(T_{\mathrm{effective}})$ but also an additional maximum at $\lambda_{\mathrm{max}}(T_{\mathrm{dust}})$. Because of this additional maximum the measured intensity – in astrophysical context referred to as the flux – exceeds the one expected from the star alone. And because of its position in the infrared it is know as INFRARED EXCESS.

Depending on the brightness of the star and the amount of dust present, the IR excess may even surmount the stellar emission in this part of the spectrum. Obviously, this observation of dust works best at wavelengths corresponding to the dust temperature. Sadly the spatial resolution is rather bad, often the beamsize is comparable to the angular size of the disc.

The first such observation of circumstellar discs reaches back to the 1980's. The INFRARED ASTRONOMICAL SATELLITE (IRAS) made measurements which resulted in the first detection of a debris disc around the star α Lyra, also know as Vega (Aumann et al., 1984).
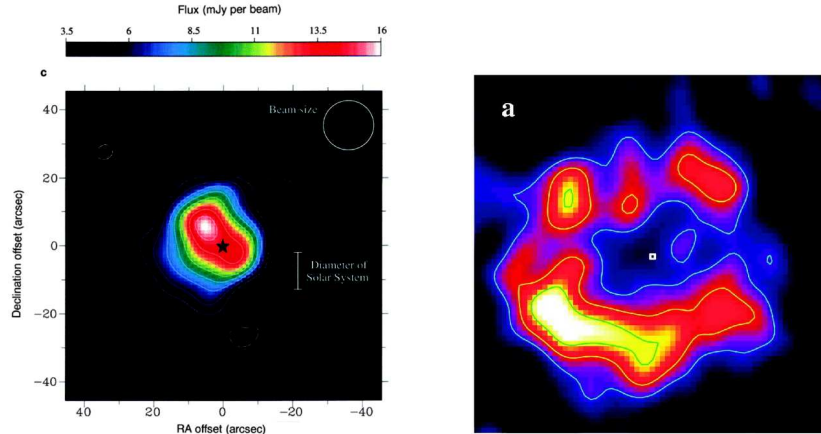
Figure 2.2: Submillimetre images ($850\mu m$) of spatially resolved debris discs from the SCUBA array. Left: Vega again (Holland et al., 1998), right: ϵ Eridani (Greaves et al., 2005). The latter image covers 70" in both directions, the contour lines are drawn at 40%, 66% and 90% of the maximum flux.

2.1.5 Examples

In our Solar System we are able to directly observe the small bodies. Known populations of them are the Asteroid Main Belt between Mars and Jupiter, the Edgeworth-Kuiper Belt outside Neptune's orbit or the Oort Cloud surrounding the whole Solar System. Dust is difficult to observe in the Solar System because of the brightness of all the other objects. In spite of this we know that there exists the Zodiacal Light, located in the inner Solar System and consisting of very small sized objects and dust.

Hundreds of debris discs have been found around other stars, although only 14 of them have been spatially resolved so far (see circumstellardisks.org). Among the first ones for which such a spatially resolved image was published, was again Vega (Holland et al., 1998).

Vega is an A0 V star on the northern hemisphere, its distance about 7.8 parsec. The left panel of Fig. 2.2 shows the submillimetre image of Vega taken with SCUBA at the James Clerk Maxwell Telescope on Mauna Kea, Hawaii. In this image a bright clump north-west of the star's position can be seen. Later images at lower wavelength, however, show a rotationally symmetric disc (Su et al., 2005). A possible explanation is that at different wavelengths we observe different particle sizes. The small ones are more strongly affected by the drag forces than the larger ones and thus their distribution is less structured.

The star with the most elaborated disc found so far is ϵ Eridani. It is a K2 V star at a distance of 3.22 parsec. The star itself holds some scientific interest. The publication of it's first spectrum reaches back to the 1930s (Raphael, 1937). It has a mass of $M_* = 0.8 M_\odot$ and a luminosity $L_* = 0.3 L_\odot$ (Guenther & Demarque, 1986; Saumon et al., 1996). Its

star	$M_*/M_\odot$	$L_*/L_\odot$	$\dot{M}_*/\dot{M}_\odot$	a_p/AU	M_p/M_J	τ_0
ϵ Eri	0.80	0.3	30	3.4	$0.86 \sin i$	
				40	0.1	(10^{-4})
AU Mic	0.59	0.3	$10 \ldots 300$	??	??	??

Table 2.1: Relevant data of star, disc and planet for ϵ Eri and AU Mic. For references see text.

mass-loss rate was determined by Wood et al. (2002) to be $30\dot{M}_\odot$. It is known to host a planet (Hatzes et al., 2000) with a projected mass $M \sin i$ of 0.86 Jupiter masses and orbiting at 3.4 AU.

ϵ Eridani's circumstellar disc was resolved at the same time with the same instrument as Vega's (Greaves et al., 1998) revealing a disc which is even more structured than Vega's. Most striking is an inner gap at a distance of 30 AU from the star and about 6 clumps at 35 to 105 AU. However, follow-up observation from the same group of authors, Greaves et al. (2005), showed that only 3 of the clumps are associated to the star, the others are background objects, neither comoving with ϵ Eridani nor rotating around it. That second paper of Greaves et al. and some others (Liou et al., 2000; Ozernoy et al., 2000; Quillen & Thorndike, 2002; Deller & Maddison, 2005) proclaime a second, further out planet at about 40 AU with an orbital period of 280 or more years. It is believed to be responsible for the observed structure. The radial velocity planet it is too far in to shape the disc at several tens of AU.

The most thoroughly studied disc, however, is that of β Pictoris. The star itself is of spectral type A5V and resides 19.3 parsec from the Solar System. The disc was discovered by IRAS observations also, about the same time as Vega's (Smith & Terrile, 1984). More than 200 papers have been written about it until now, a review is given by Lagrange et al. (2000). The biggest difference of this disc to the two previous ones is the edge-on view, i.e. the disc is lying in the viewplane. Observations have shown a prominent warp (see e.g. Heap et al., 2000, and references therein) and unpaired bright spots (Telesco et al., 2005). Both structures are often associated with planets residing within the disc, recently Freistetter et al. (2007) proposed a system of 3 planets.

Only 4 years ago a disc was discovered around the dwarf star AU Microscopii. It could not be resolved in submillimetre, but in near infrared wavelength (Kalas et al., 2004). The disc is seen edge-on and shows a brightness asymmetry between the north-west and south-east wing. AU Mic is a M1V dwarf star at 9.0 parsec. It has a stellar mass of 0.59 solar masses and a luminosity of $L_* = 0.3L_\odot$ (Pagano et al., 2000). It is one of the most active nearby stars (Smith et al., 2005), which means that there is a strong, but not necessarily constant stellar wind. Three recent papers, Augereau & Beust (2006); Strubbe & Chiang (2006); Fitzgerald et al. (2007), tried to quantify the wind and construct appropriate models to fit the observed spectrum, obtaining very different results. Whereas the first
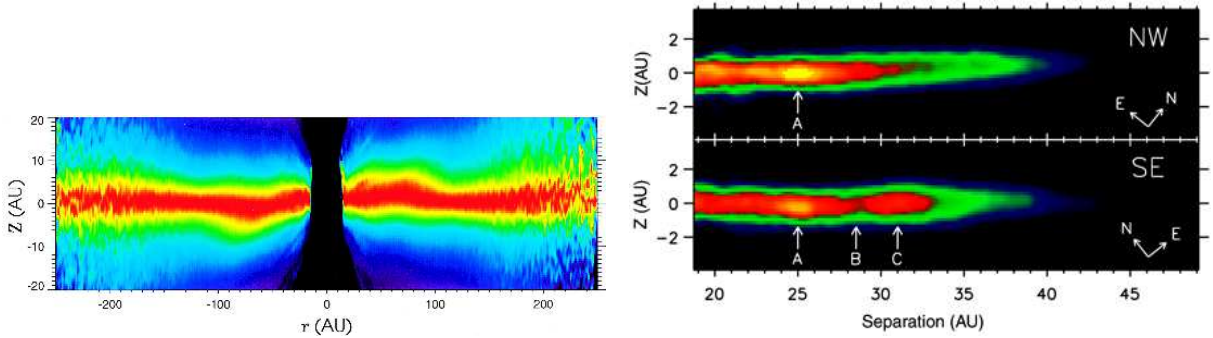
Figure 2.3: Left: Coronographic image of the β Pictoris disc, obtained with STIS at Hubble Space Telescope (Heap et al., 2000). It sums light of wavelengths $0.2 \ldots 1\mu m$. The flux is normalized to the maximum flux, to enhance the warp. Right: Infrared image ($1.63\mu m$) of the AU Microscopii disc obtained at the Keck II Telescope, exemplifying the radial substructure (Liu, 2004). A and C mark brightness enhancements at 25 AU and 31 AU, B a depletion at 29 AU.

authors claim a mass-loss rate of 300 times that of the Sun, the second claim that it is slightly below 10 times the solar loss rate for the second ones. The reason is that there are lots of flares from the star and it is not clear how frequent they are precisely. Augereau & Beust (2006) used their own, recent HST measurements, whereas Strubbe & Chiang (2006) analysed publicly available and thus measurements that are a few years old. This large range given for the stellar properties of course leads to very different results for the amount of circumstellar material.

2.2 Resonance

In basic mechanics a resonance occurs when in an enforced libration the eigenfrequency of the system is equal to that of the exciter. Then the amplitude of the enforced libration rises steeply – to infinity if there is no damping – and the dispersion function diverges.

In celestial mechanics a resonance is the description for the phenomenon when in the orbital motion of two bodies around their mutual primary there is a commensurability in at least one parameter of their orbits. This commensurability leads to a symmetry in their motion and especially in the regular repetition of certain geometrical configurations, which in turn gives a net effect, a summation of otherwise small forces to the orbits. Resonances exist in a variety of regimes of motion, such as the mean motion, secular or Kozai resonances, and thus have a variety of effects, such as spin-orbit-coupling, secular precession, libration of the axis of nodes, increase or decrease of inclination, eccentricity or semimajor axis. The effects can be both stabilizing or destabilizing, depending on the type of resonance. What they all have in common is that they change the dynamics of the system dramatically compared to a similar nonresonant one and that there always is
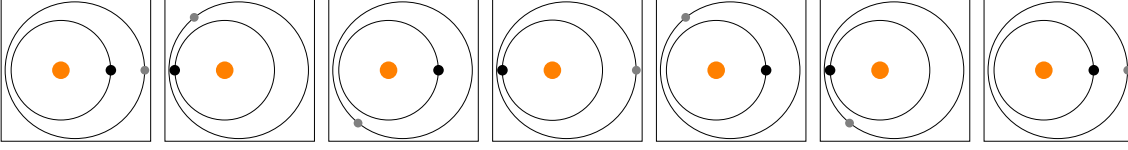
Figure 2.4: Sketch of the orbital motion in an external 3:2 mean motion resonance. The star is the light grey dot in the centre, the planet the black one and the small body (asteroid or dust grain) the small grey one.

a certain combination of angles, called the resonant argument, which librates around a certain value. The which angles are involved and where the centre of libration is, depends on the resonance type.

2.2.1   Mean Motion Resonance

In this work we will focus on mean-motion resonances. This means that the mean motion n, corresponding to the orbital frequency, of two bodies has the simple, algebraic connection,

$$\frac{n_1}{n_2} = \frac{p}{p+q} \,,$$

where p, q are integers.

Here the resonant argument Φ is a combination of mean longitude λ and longitude of pericentre ω,

$$\Phi = (p+q)\lambda_1 - p\lambda_2 - q\omega_1 \,.$$

It librates around a certain value Φ_0, often close to $0°$, $180°$, or $270°$, with a given amplitude A, referred to as the libration width (Murray & Dermott, 1999; Kuchner & Holman, 2003; Wyatt, 2006). Fig. 2.4 depicts a small body in a 3:2 mean motion resonance with a planet. Here $\Phi_0 = \pi$ and A was set to zero.

In the case of the primary 1:1-resonance ($p = 1$, $q = 0$), corresponding to Trojan satellites, the resonant argument simplifies to

$$\Phi = \lambda_1 - \lambda_2$$
$$\text{with } \lambda_2 = \lambda_p$$

and librates around the $\Phi_0 = \pm\pi/3$, which corresponds to the motion in the vicinity of the Lagrange points L_4 and L_5.

In such a mean-motion resonance between a planet and small bodies in a surrounding debris disc the planet plays the role of the exciter enforcing a density wave in the disc. Now this density wave, not the individual small bodies, is comoving with the planet during the latter's orbital motion.

2.2.2   Resonant Locking

To explore the physical workings of a resonance we consider a planet on a circular orbit and a small body, an asteroid for example, in a slightly eccentric orbit with a somewhat larger semimajor axis, its orbital velocity therefore being being smaller than the planet's. Further let their orbital periods be near a commensurability, thus leading to repeated, regular conjunctions. Now consider those conjunctions taking place shortly before the apocentre. When the planet is approaching the asteroid the latter feels the additional gravitational force of the planet from a different direction than that of the primary. The planet's gravity can be split up into one component acting in the direction of the primary and a component tangential to the orbit. Just before conjunction the second component acts in retrograde direction, afterward conjunction in prograde direction with respect to the asteroid's orbits. Since the asteroid is nearing its apocentre it is slowing down at this time, which means the tangential force just after conjunction can affect it for longer than the one before. This means there is a net-force in the direction of the apocentre, resulting into conjunctions nearer to the apocentre after each fly-by. See Fig. 8.5 of Murray & Dermott (1999) for a schematic illustration of these forces.

If, however, the conjunction takes place slightly after the apocentre passage the asteroid will speed up again. Now the retrograde tangential force is the longer acting one, pulling the asteroid backwards, and again the next conjunction will take place nearer to the apocentre.

For conjunctions exactly at the apocentre both tangential forces, prograde and retrograde one, will act for the same time intervals and thus compensate each other. They will no longer change the small body's orbit. It will only be affected by radial gravitational forces now. This situation then is described as a 'resonant lock'. The described resonant locking mechanism works for conjunctions at pericentre, too. Those resonances, however, are not stable.

The efficiency of resonant capture and locking depends on some system parameters, especially the planet-to-star mass ratio M_p/M_* and on the orbital parameters of the small body. Resonant capture is not or hardly possible for highly eccentric particles, because as they near their apocentre and thus slow down, they also diverge from the planet. Thus the latter's influence lessens after conjunctions and there is no resulting force towards the stable apocentre conjunction. The problem has been readressed lately by Quillen (2006). To obtain definite, numerical values for the upper limit on eccentricities for resonance capture quite sophisticated numerical techniques are necessary and the result depends strongly on various parameters, such as e.g. stellar and planetary mass, asteroid's size or inclination.

2.2.3   Consequences

Once locked into a resonance there are no more shear forces onto any small body from the planet but an interplay of centrifugal forces at the fly-bys, enhanced gravity at conjunction and diminished gravity at opposition. If the conjuction takes place at apocentre, i.e. the largest distance between both orbits, the two gravity variations are neglectable and the resonant configuration is a stable one. For conjunctions at pericentre the resonance leads to close encounters of the small body with the planet and thus the latter will scatter and eject the small body from its orbtit.

The lack of shear forces means that the angular momentum and subsequently the semimajor axis of the small body are preserved. A resonance stabilizes the orbit's semimajor axis against any other perturbances at the so called resonant semimajor axis a_{res},

$$a_{\text{res}} \;\; = \;\; \left(\frac{p+q}{p} \right)^{2/3} a_p \; .$$

(2.6)

Here a_p is the planet's semimajor axis and p and q are the two integers of the resonance. If "particles" are small dust grains rather than planetesimals, a_{res} is shifted by a factor of $(1 - \beta)^{1/3}$.

Regarding the inclinations there is a similar effect on them as was on the apocentre distance of conjunctions. If the small body's orbit is inclined to the planet's the latter's gravity will exert a shear force directed towards the plane of the planetary orbit. Thus, within a mean-motion-resonance the inclination will gradually start to decrease. For the eccentricities the story is an entirely different one. The small bodies are subject to the radiation pressure which propels them away from the star. Since at the same time the angular momentum is preserved, the only way to cope with the additional energy is an enhancement of the eccentricity. According to Liou & Zook (1997) it grows as

$$e^2(t) \;\; = \;\; \frac{q}{3p} \left[1 - exp \left(-\frac{3p}{p+q} Bt \right) \right]$$

(2.7)

$$\text{with } B = 2GM_* \beta / (ca^2) \; .$$

(2.8)

In real, physical systems a resonant lock will never be perfect. There will most certainly be slight deviations in the conjunctions, inclinations and semimajor axes. In order to describe the perfection or imperfection of a resonance we introduce the libration width A. This is the half width of the interval in which the resonant argument Φ may librate,

$$\Phi_0 - A \leq \;\; \Phi \;\; \leq \Phi_0 + A$$

In a perfect resonance A would be zero, for not so perfect ones it will be larger, up to the value of π, where there is no resonance at all anymore.

Figure 2.5 gives an impression of these consequences of the resonance for three of a small body's orbital elements as well as the resonant argument. The results were obtained
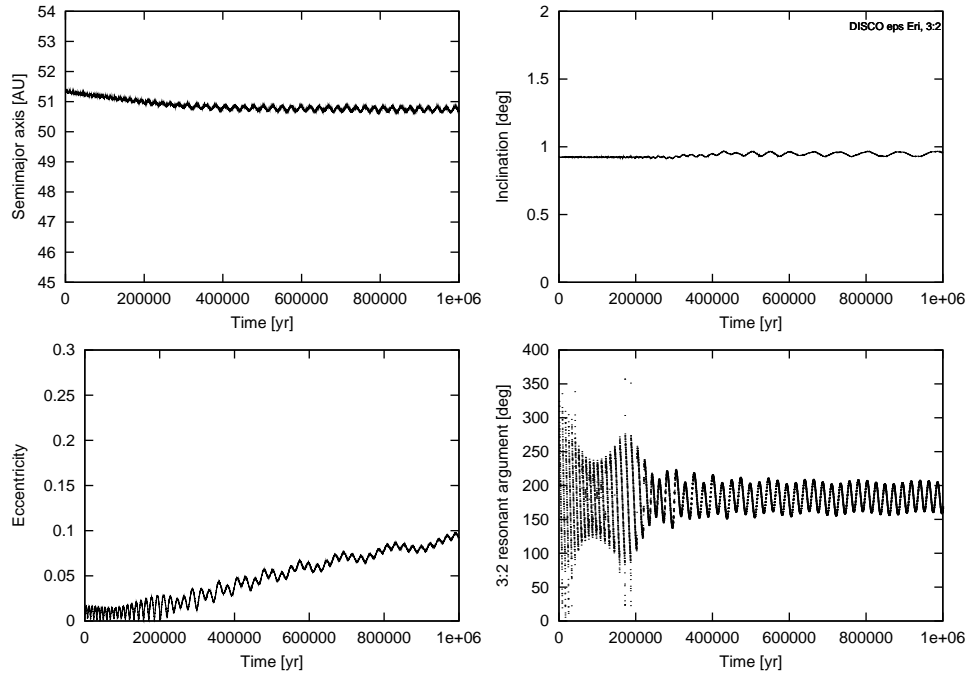
Figure 2.5: Consequences a resonant capture, obtained by numerically integrating the equations of motion. Example star is ϵ Eridani ($M_* = 0.8 \, M_\odot$), planetary data are $M_p = 0.1 \, M_{\mathrm{jup}}$, $e_p = 0.005$, $a_p = 40 AU$. The small body was captured in a 3:2 resonance.

by integrating a massless particle's equation of motion numerically using a prefabricated RADA integrator (Everhart, 1974, 1985).

Applying all these consequences to a whole disc of small bodies perturbed by a planet and being caught in resonances the result – in the idealized case – is the following: The orbits of the small bodies will be aligned, they will all have the same semimajor axis, orbit in the plane of the planet and their eccentricities will be growing. Consequently the overall structure of the disc of small bodies will be reshaped and not be rotationally symmetric anymore. There will be regions of enhanced number density and regions depleted of material. Depending on the parameters of the resonance and orbital parameters of the small bodies this leads to the creation of different structures such as clumps, arcs or rings. Fig. 2.6 and 2.7 show some scatterplots for different eccentricities, libration widths and resonances $(p + q)/p$.

Looking at the first order resonances, i.e. $q = 1$, we see that a $(p + q)/p$ resonance produces p clumps. It becomes clear why when we follow the motion a resonant particle with nonzero eccentricity in a reference frame comoving with the planet. There the particle's path has p turning points, or even loops for high eccentric ones (cf. p. 325 of Murray & Dermott, 1999).

Figure 2.6: Scatterplots of a 3:2 resonance. It shows a snapshot of the resonant population, projected into the planets's orbital plane. In the left panel the maximum eccentricity is 0.2, in the right one it is 0.5, libration width in both cases is $A = 0.1\pi$. The coordinate system is in units of a_p, the planet is located at (1,0), the star at (0,0).

2.2.4 Examples
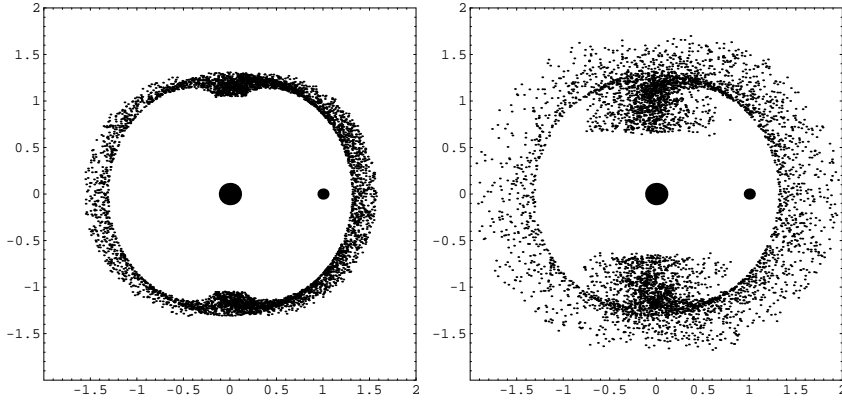
Capture in mean motion resonance is known to be a common phenomenon in the Solar System. Examples are groups of Near Earth Objects caught in 3:1 and 7:2 resonance (Gladman et al., 2000, and references therein) or the various resonances of the Main Belt with Jupiter, among the the Hilda group in a 3:2 or the Koronis family in 5:2 resonance. The resonances in the Main Belt are inner one with Jupiter. Many of them are destabilizing, removing material from the locations $a \approx a_{\mathrm{res}}$. This resulted in the Kirkwood Gaps – regions in the Main Belt depleted of material (Kirkwood, 1867, and references therein). Last, but no least, there are the Twotinos and Plutinos in the Edgeworth-Kuiper Belt which reside in 2:1 and 3:2 resonance with Neptune, respectively (Chiang & Jordan, 2002).

It is generally assumed that similar structures exist in discs around other stars, too. The azimuthal substructure observed in some debris discs, as shown for ϵ Eridani above, is usually attributed to resonances with embedded planets. Thus resonances in debris discs can be used as tracers for otherwise nonobservable planets.

2.3 Collisions

The overall dynamics of a debris disc are dominated by the star and the planets, but the small bodies in there interact in the form of collisions. These are more difficult to describe and model adequately than the resonances. The physics of collisions depend not only on kinematic and geometrical parameters but also on a multitude of parameters of projectile and target, e.g. their size, chemical composition, porosity, crystalline phase and so on. Experiments in order to study the details of collisions are only possible for smaller particles, up to a size of a few centimetres (Nakamura, 2002; Kadono et al., 2005, and
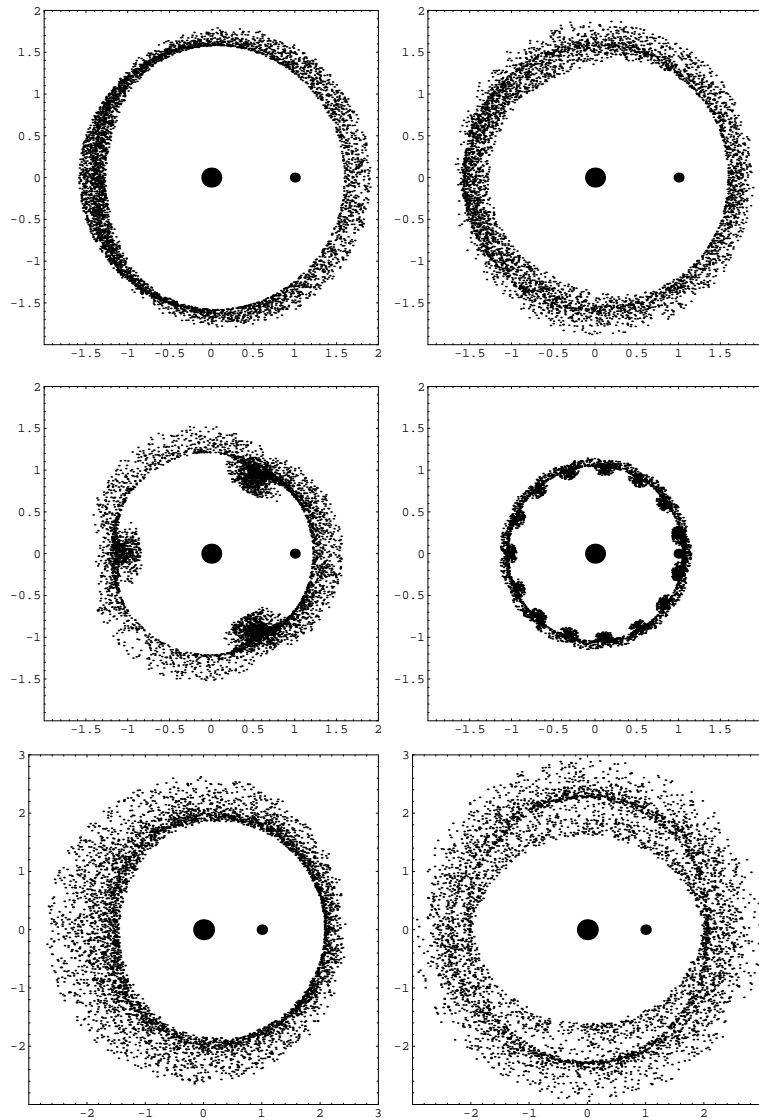
Figure 2.7: Scatterplots of some other resonances. For each one the star is at $(0,0)$, the planet at $(1,0)$. Top panel: 2:1 resonance with maximum eccentricity 0.2, but $A = 0.1\pi$ (left) and 0.4π (right). Middle panel: First order resonances with larger p. 4:3 on the left ($e_{\max} = 0.3$, $A = 0.1\pi$) and 16:15 on the right ($e_{\max} = 0.1$, $A = 0.01\pi$). A and $e_{\max}$ are chosen to show clumpy structure most suitably. Bottom panel: Higher order resonances ($q > 1$), 3:1 on the left and 7:2 on the right ($e_{\max} = 0.3$, $A = 0.1\pi$ both cases).

references therein). Thus theoretical descriptions are needed in order to extrapolate the data up to sizes of several hundred kilometres typical for astronomical ensembles.

2.3.1 Types of Collisions

Depending on the collisional velocity V_{imp} and impact angle there are different types of collisions. For very low velocities the collisions are *elastic*, i.e. the colliders only change direction and speed.

At higher V_{imp} and a wide collision angle the projectile may stick to the target after collision (*sticking* collision), this is especially important for particle growth in protoplanetary discs.

If the impact velocity sufficiently large, the collisions are destructive and produce a variety of fragments. The mildest forms are erosive or *cratering* collisions, where only a small amount of material is chopped off, but the largest part of the target is left intact. By definition, the mass of the largest fragment is larger than half the mass of the original target. If the largest fragment's mass is smaller, the collision is called *catastrophic* or cataclysmic. This again has two types: the shattering, which destroys the target but keeps the fragments in a swarm near the centre of mass at collision. In contrast, a dispersing collision both destroys the target *and* disperses the fragments in space. In the regime of the small particles, which are not gravitationally bound, there is no difference between shattering and dispersing collisions. Once the target is broken up by a collision there is no more binding force to keep the fragments together and they start to disperse in space. For the larger, gravity bound bodies a dispersing collision needs a higher kinetic energy at collision, i.e. a higher impact velocity, than a shattering one (Benz & Asphaug, 1999). Because in addition to the binding forces of the target, also the attractive gravitational force has to be overcome.

In debris discs there is no decelerating/damping gas, so that the collisional velocities are all above the destruction treshold in any case. Thus all collisions are catastrophic one.

2.3.2   Description

In this work we will confine ourselves to catastrophic collisions, i.e. the kinetic energy Q at collision is always larger than the shattering and dispersing border, Q_S^* and Q_D^*, respectively. The first analytic description of such collisions was given by Dohnanyi (1969). Therein he considered a balance equation for the number density of colliding particles of the form

$$\frac{dn(s)}{dt} = -(\text{ loss by erosion }) - (\text{ loss by catastrophic collisions }) \\ + (\text{ gain by erosion and break-up of larger ones })$$

He found that this can be satisfied by a power law,

$$n = \mathcal{N}m^{-1-\alpha}, \tag{2.9}$$

a result which was in good agreement with observations of the Solar System's asteroids. "$1+\alpha$" is called the population index. It can be shown that if it is smaller than $5/3$ the large particles are overabundant, the material loss dominates and a steady-state cannot be reached. If, in contrast, $1+\alpha > 2$ the erosion dominates and likewise a steady-state is not possible. The actual value was determined by Dohnanyi to be

$$1+\alpha = 11/6 \,. \tag{2.10}$$

In Dohnanyi's frame of reference this result is independent of other physical parameters to 1st order.

More recent models of colliding ensembles are hydrodynamical codes as well as improvements of Dohnanyi's statistical approach. Benz & Asphaug (1999) describe a hydrodynamical code which describes the whole size range of the ensembles. It gives easy access to the fragments' parameters such as size, velocity and angular momentum, but it is based upon the knowledge of the density of flaws, the stress tensor and equation of state of the colliders. It assumes compact, crystalline structures, not allowing porous or amorphous material.

The statistical approaches are not hindered by such constrains. For them the description of velocity and momentum is not as straightforward, the observed size distribution is reproduced very well, though.

Campo Bagatin et al. (1994) refined Dohnanyi's simple approach by considering the effect of finite maximum and minimum masses, $m_{\min}$ and $m_{\max}$, respectively. Already Dohnanyi himself pointed out that (2.9) is only true far from the ends of the distribution. If finite borders are incorporated the simple power law size distribution turns "wavy". Meaning when compared to (2.9), where there was no $m_{\min}$, the grains just above this threshold ($m \gtrsim m_{\min}$) are more abundant, because they cannot be destroyed by the somewhat smaller ones anymore. They can, however, destroy the slightly larger ones very well, so those are less abundant than according to (2.9). And so on. The further we get away from $m_{\min}$, the flatter the wave becomes and the distribution approaches the underlying power law.

A second refinement was given by Durda & Dermott (1997), who considered the size dependence of the break-up energy per volume Q_D^*. In Dohnanyi's work it was implicitly assumed to be constant,

$$Q_D^* \equiv constant. \tag{2.11}$$

This energy, however, is a function of the particle size. Durda & Dermott (1997) describe a power law dependence

$$Q_D^* \sim s^k, \tag{2.12}$$

and found that the exponent is a function of size itself,

$$k = f(s). \tag{2.13}$$

This originates in the change of the binding mechanisms along the size scale from km to μm sized bodies. Among the larger planetesimals gravity binds them ('gravity regime') and $k > 0$, among the small dust grains chemical and van-der-Waals forces bind them ('strength regime') and $k < 0$. Dohnanyi's implicit value $k = 0$ is just the transition between the strength and gravity regimes. Since α depends on Q_D, it is thus size dependent, too.

2.3.3 Consequences

Collisions do play an important role in sustaining a debris disc. At any time material, especially in the form of very small dust grains, is lost due to radiation pressure, PR or wind drag, evaporation in the vicinity of the star or gravitational scattering by other particles. Collisional grinding ensures that the size range of circumstellar material stays complete and stable over a long time.

On the other hand, collisional grinding also causes the disc to "age". It does break up big particles with $\beta \approx 0$ into smaller ones with nonzero β, or even $\beta > 0.5$. Where the first ones then fall victim to drag forces and are removed slowly, the latter are below the blow-out limit in size and leave the system immediately. Thus collisions result in a loss of disc material and consequently a decay of the debris disc (see e.g. Löhne et al., 2007).

2.4 Goal of This Work

In order to understand better the origin and evolution of planetary systems we want to study the structure of as many of them as possible. Unfortunately, observation of extrasolar planetary systems is even more complicated than that of the Solar System. The planets themselves can be found either by radial-velocity measurements, transits or direct imaging. Where the first is biased to large, close-in planets (Hot Jupiters), the second is biased to large ones at a special viewing geometry and the third one to bright, young planets. Terrestial planets are not observable today, but might be in the near future, e.g. by CoRoT or Darwin/TPF. Asteroids around other stars are not observable at all. The dust, however, *is* observable, as mentioned before. Observation of circumstellar dust together with a vast theoretical background may make indirect observation of extrasolar asteroid belts and planets possible. Therefore our understanding of the connection of planets, asteroids and dust must be as elaborated as possible.

Collisions are grinding down asteroids, thus producing dust. And resonances pile up material to clumps and certain structures of enhanced particle density, which in turn leads to an enhanced brightness. However, rather high collisional velocity may lead to an expulsion of the material from the resonance and destruction of the structures.

Therefore in this work we will combine resonant dynamics with collisional interaction. We will use analytic treatments and as much generality as possible in order to make our results applicable to as many systems as possible. We will *not* study the features and characteristics of a individual small body population to the smallest detail feasible. We will instead make a parameter study of fiducial ones, which can be used as a stencil when studying an individual, observed debris disc.

We will determine how and to what extent resonances change the collisional velocities and rates of circumstellar small bodies. Further we will investigate how resonant structures might arise and examine two different scenarios of the origin of observable dust populations at resonant clumps.

Chapter 3

Collisional Velocities and Rates

3.1 What *is* Kinetic Theory?

Circumstellar discs are often treated by the particle in a box method or n-body codes with a variety of modifications such as e.g. multiannulus treatment (e.g. Thébault & Augereau, 2007). Those methods treat a swarm of individual particles, following the motion and evolution of each and every one to then combine them to a disc. In many of these codes a rotationally symmetric disc is an essential assumption. In the case of mean motion resonances, however, this is violated totally, as the disc particles locked in a resonance group into clumps, arcs or other highly nonrotationally symmetric structures.

If we additionally want to treat collisions among the disc particles, further problems arise. N-body codes usually can treat only up to $\sim 10^4$ particles, which is far too few to treat collisions amongst them. There are nonetheless methods to incorporate collisions, e.g. by an inflated radius of the particles (Thébault et al., 2003). That, however, leads to other problems because not all the scaling laws are independent of the particle size, as is shown in Durda & Dermott (1997).

In order to combine collisions with resonances consistently, we will use a kinetic approach, which means, we will not treat groups of individual particles but continuous distributions $n(\mathbf{p}, \mathbf{q})$, which contain all the necessary information. $\mathbf{p}$ and $\mathbf{q}$ are vectors of the phase space, they contain e.g. mass, position or velocity. Later we will arrange them so that $\mathbf{p}$ contains the essential, useful variables and $\mathbf{q}$ the ones to be averaged over. Integrating the distribution over both,

$$\iint n(\mathbf{p}, \mathbf{q}) \, d\mathbf{p} \, d\mathbf{q} \;\; = \;\; n \qquad\qquad (3.1)$$

gives the total number of particles n in the ensemble.

Since their actual number is of no consequence as long as there are enough to justify

the use of statistical methods, we introduce normalized distributions ϕ,

$$n(\mathbf{p}, \mathbf{q}) \; = \; n\phi(\mathbf{p}, \mathbf{q}) \tag{3.2}$$

$$\iint \phi(\mathbf{p}, \mathbf{q}) \, d\mathbf{p} \, d\mathbf{q} \; = \; 1 \;. \tag{3.3}$$

Following Krivov et al. (2005), we denote by $\phi(x, y, ...)dxdy...$ the fraction of particles in the disc with arguments $[x, x+dx]$, $[y, y+dy]$, ... Thus we can consider an unconstrained number of disc particles and include certain asymmetries of the ensemble.

The derivation of the distribution is accomplished by solving the equation of balance between losses and gains of disc particles, the so called Master Equation,

$$\frac{dn}{dt} \; = \; \left(\frac{dn}{dt}\right)_{\text{gain}} - \left(\frac{dn}{dt}\right)_{\text{loss}} - \nabla \cdot (\dot{\mathbf{r}}n) \;. \tag{3.4}$$

The last term describes transport of material through the disc. It is important in young, still gas-rich discs only. It can be neglected here since $\dot{\mathbf{r}}n$ is approximately zero compared to the two other terms and the disc is collision dominated.

Material is lost to some extent by radiation pressure or PR drag also, but mainly by collisions. The collisional outcome then is the main source for material gain in debris disc. In terms of the distribution of targets $n(\mathbf{p})$ and projectiles $n(\mathbf{p}_p)$,

$$n(\mathbf{p}) \; = \; \int n(\mathbf{p}, \mathbf{q}) \, d\mathbf{q} \tag{3.5}$$

$$n(\mathbf{p}_p) \; = \; \int n(\mathbf{p}_p, \mathbf{q}_p) \, d\mathbf{q}_p \tag{3.6}$$

the loss term cam be written as

$$\left(\frac{dn}{dt}\right)_{\text{loss}} (\mathbf{p}) \; = \; n(\mathbf{p}) \int n(\mathbf{p}_p) \dots \Delta(\mathbf{p}, \mathbf{p}_p) \, d\mathbf{p}_p \;. \tag{3.7}$$

Crucial for any further calculation is the evaluation of the integration kernel $\Delta(\mathbf{p}, \mathbf{p}_p)$, from here on called Δ-integral. But the Δ-integral is not an instrument to solve (3.4) solely, it also gives direct access to some properties of the ensemble, most notably those we are seeking: the collisional velocity and rate of the resonant ensemble.

3.2   Assumptions and Preconditions

This work will exclusively deal with debris discs, meaning they will be at least some tens of millions of years old. Consequently they will be fully developed, all accretion and planet formation processes have long been concluded. The primary will be a single, main-sequence star, radiating steadily and with a luminosity L_* scaling with its mass,

$$L_* \; \sim \; M_*^{3.8} \;.$$

Orbiting around it will be one, and only one planet on a stable orbit. We are well aware that many stars are in multiple systems and that in at least some dozen systems more than one planet is present around the primary. We neglect those cases here, because in the case of a close binary with a circumbinary disc both stars will act as one primary and not alter the dynamics in the disc. In the case of wide binaries or even a disc around only one of them the interaction of both stars will perturb the disc more strongly than any planet could, meaning there will be no resonant structures there. The case of multi-planet systems is similar. If two or more of them perturb the disc in equal measure they will prevent any pronounced resonant structure from developing. If, on the other hand, there is a multi-planet system in a situation is similar to the Solar System, only one planet will disturb the circumstellar disc, the others will not influence it. For example Neptune influences the Kuiper Belt creating populations like Plutinos and Twotinos, the other seven planets, even the much larger Jupiter, are irrelevant here.

Further, this single planet will have a *circular* orbit, i.e. $e_p \equiv 0$. Again, for the Solar System, this assumption is natural. For many other systems where planetesimals are expected to be trapped in resonances as a result of planetary migration, it is reasonable, too, since dissipative forces that cause migration tend to circularize the planetary orbit (Wyatt, 2003). If, instead, capture of dust particles is considered, and therefore the mechanism of resonant capture is dust transport by dissipative forces rather than planet migration, resonance capture is known to be most efficient for less eccentric planets. Quillen (2006), among others, numerically investigated the dependence of the dust capture probability on e_p. She found that resonant capture is only possible if $(M_p/M_*)^{-1/3}e_p \sim 1$, where M_p and M_* are the masses of the planet and the star, respectively. Furthermore, even if capture occurs, already a low planetary eccentricity of ~ 0.05 smears a clumpy resonant structure to a rotationally symmetric ring (Reche et al., 2008).

Gas will be present in the disc in traces only, if at all, it will have no dynamical influence. The orbital motion of the small bodies in the disc will be purely Keplerian. The material in the disc has been thoroughly processed by accretion, disruption and possibly re-accretion before, it is therefore described as second generation or in other words: debris.

All bodies in the disc are assumed to be solid, justified by the collisional processing, and spherical, which actually *is* a simplification. But since we consider whole ensembles and not individual bodies, this can be viewed as the average over the shapes of all members of the ensemble in question.

All particles in an examined ensemble will be in a mutual resonance. Each will be an external, mean-motion resonance, thus

$$a_{\mathrm{res}} \gtrsim a_p \ .$$

Upon collision both colliders will leave the ensemble. Either because they have been disrupted into smaller fragments and do not exist anymore or because their orbits are changed so that they no longer reside in that resonance.
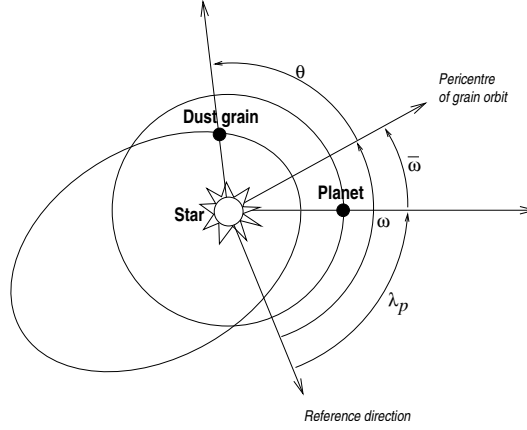
Figure 3.1: Angular variables in 2D.

Further, we confine our analysis to *small inclinations*, $i \lesssim 10°$. One reason for that is that orbital inclinations of small bodies in the Solar System and other planetary systems have this order of magnitude. Another reason is that higher inclinations drastically reduce the probability of resonance capture or make the resonant orbits unstable (e.g., Wisdom, 1983; Jancart et al., 2003; Gallardo, 2006). Already Wisdom (1983), who explored the phase space in the vicinity of mean motion resonances, found chaotic behaviour in slightly inclined orbits ($i = 10°$), where the same orbits were stable at zero inclination. More recent analysis of the three-dimensional dynamics back up Wisdom's conclusion. While Gallardo (2006) describes a drop in the strength and changes in stability of the resonance for highly inclined ($i = 40°$) orbits, Jancart et al. (2003) investigated the resonance capture probability in dependence on the particles' inclination. In a series of simulations with the same initial semimajor axis and eccentricity where capture was always possible for inclinations below 10°, they found it to be only sometimes possible between 10° and 40°, totally impossible for inclinations above 40°. We will compute collisional velocities by simply assuming $i = i_p = 0$, and take into account corrections due to small non-zero inclinations only in the calculations of collisional rates. Thus we can assume a 2-dimensional geometry as shown in Fig. 3.1. The current position of the planet will not be of interest for our calculation. Therefore we introduce overlined variables, measured with respect to the planet:

$$\begin{aligned} \overline{\omega} &\equiv \omega - \lambda_p, \\ \overline{\lambda} &\equiv \lambda - \lambda_p. \end{aligned}$$

The resonant argument for a particle in mean motion resonance with the planet in this reference frame reads

$$\Phi = (p+q)\overline{\lambda} - q\overline{\omega}.$$

Thus the planet appears implicitly only and we can fully concentrate on the resonant belt.

3.3 Resonant Belt

3.3.1 System

We will consider the following system. There is a massive body, which we will call planet, orbiting the primary, referred to as a star, and a disc of objects (small bodies or dust), orbiting the same primary. The motion of each of the objects in 3D is described by six Keplerian orbital elements

$$a \, , \, e \, , \, i \, , \, \omega \, , \, \Omega \, , \, \lambda, \tag{3.8}$$

which stand for the semimajor axis, eccentricity, inclination, argument of pericentre, longitude of ascending node, and mean longitude, respectively. Instead of λ, either the mean anomaly M or the true anomaly θ can be used. The elements of the planet will be marked with a subscript p.

3.3.2 Simplifications

In addition to the general assumptions explained in Sec. 3.2, we need to make some technical simplifications for this calculation. First we assume all particles to have the same "typical" radius. This is justified by the fact that we want to focus on geometrical effects caused by resonance locking, rather than on the size or shape distribution effects.

As long as we consider macroscopic objects, whose dynamics is purely gravitational and therefore independent of their size, this assumption does not imply any loss of generality. It *would* be a simplifying assumption for dust, the motion of which is affected by radiation pressure and is therefore size-dependent.

Both the libration amplitude A and the maximum eccentricity $e_{\max}$ depend, in a complex way, on the mechanism of resonant trapping (Poynting-Robertson effect, planet migration, etc.). Furthermore, even for a given trapping mechanism, both quantities depend on a multitude of physical parameters: planet mass, strength of stellar wind, order of the resonance, etc., see e.g. Fig.4.4 later in this work. Throughout our investigation, we assume that both A and $e_{\max}$ can be "pre-determined" by a dedicated dynamical study of a system of interest, and therefore treat them as *free parameters*.

Additional, less important simplifications, are introduced as appropriate.

3.3.3 Distributions

In 2D, four instead of orbital elements fully describe the particle's motion:

$$a \, , \, e \, , \, \theta \, , \, \overline{\omega}.$$

As for the whole resonant ensemble $a \equiv a_{\mathrm{res}}$ it is a parameter here and only three remaining elements represent the phase space variables.

We now introduce the distributions of this variables. The mean longitude $\overline{\lambda}$ is distributed uniformly, and the distribution of the true anomaly θ follows from the Kepler equation:

$$\phi(\overline{\omega}, \theta) = \phi(\overline{\omega}, \overline{\lambda}) \left| \frac{\partial \overline{\lambda}}{\partial \theta} \right|_{\overline{\omega}} = \phi(\overline{\omega}, \overline{\lambda}) \frac{r^2}{a^2 \sqrt{1 - e^2}} ,$$

where $\overline{\lambda}$ on the right-hand side should be calculated from θ by means of standard formulas of Keplerian motion

$$\overline{\lambda} = \overline{\omega} + M, \tag{3.9}$$

$$M = E - e \sin E, \tag{3.10}$$

$$\tan \frac{E}{2} = \sqrt{\frac{1 - e}{1 + e}} \tan \frac{\theta}{2}. \tag{3.11}$$

Within the resonance, where $\Phi_0 - A < \Phi < \Phi_0 + A$, the distributions of $\overline{\omega}$ and λ (or θ) are not independent. Assuming the distribution of the resonant argument Φ to be uniform within the libration width, we obtain

$$\phi_\omega(\overline{\omega}, \overline{\lambda}) = \frac{1}{2\pi} \frac{1}{2A} H \left[\Phi_0 - A < \Phi < \Phi_0 + A \right], \tag{3.12}$$

where $H[cond]$ is a Heaviside function, which equals one if the evaluation of *cond* returns *true* and zero if *cond* returns *false*. If needed, e.g. to examine a certain observed population, $H[.]$ can be replaced by a more realistic distribution, e.g. sinusoidal.

Particles caught in a resonance may have eccentricities between zero and a maximum value e_{max}. To keep the analysis simple, we assume a uniform distribution between these two borders,

$$\phi_e(e; e_{max}) = \frac{1}{e_{max}} H[e < e_{max}]. \tag{3.13}$$

This simplification, just like the one for the resonant argument made above, can always be lifted by replacing the Heaviside function with a more realistic distribution. Because of $e^2 \sim exp(-t)$, see Eq. (2.7), the eccentricities grow quickly for small e and slowly for larger ones, thus building a maximum of the distribution near $e = e_{max}$. That is confirmed by observations: The Plutinos, which are in 3:2 resonance with Neptune, are piled from $e \approx 0.1 \ldots 0.3$ (Morbidelli et al., 2003).

Figure 3.2 gives a visual impression of how the distribution (3.12) describes a resonant population. Plotted is the distribution of Cartesian coordinates $\phi_{xy}(x, y)$ calculated from $\phi_\omega(\overline{\omega}, \overline{\lambda})$ by the virtue of

$$\phi_{xy}(x, y)|dxdy| = \phi_\omega(\overline{\omega}, \overline{\lambda})|d\overline{\omega} \, d\overline{\lambda}|. \tag{3.14}$$

The upper plots, drawn for a small libration width A, show "loopy", pretzel-like structures, well-known to be typical of the synodic motion of resonant particles (cf. Murray
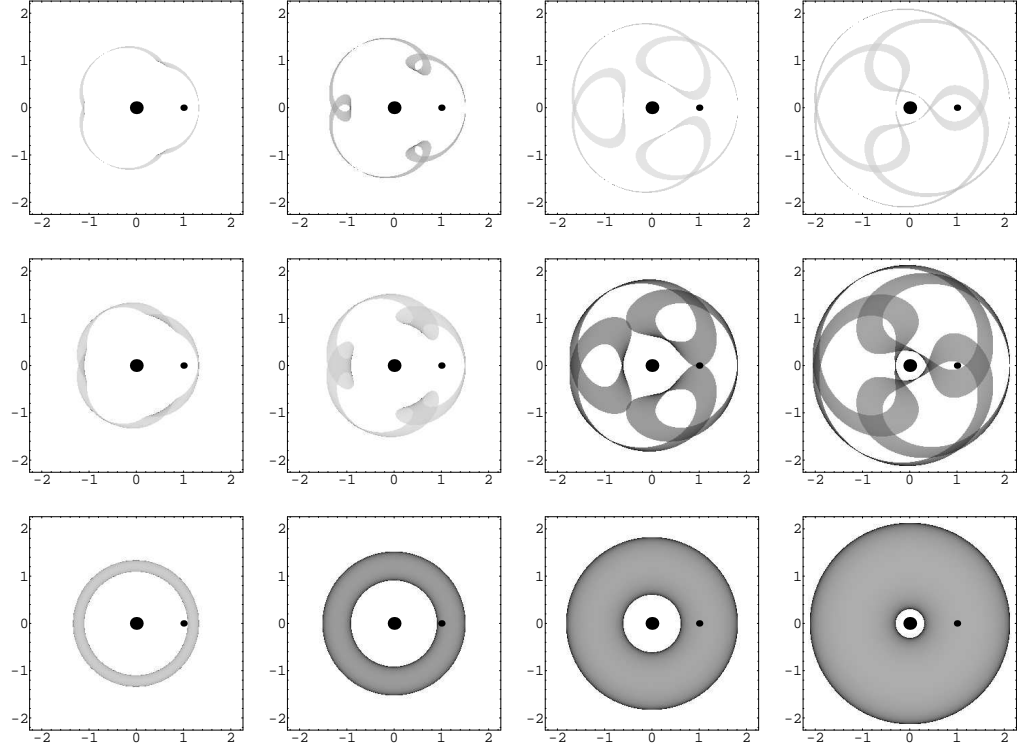
Figure 3.2: Density distribution (3.12) of objects for single eccentricity values, locked in a 4:3 resonance. The grey scale is arbitrary; the darker the grey, the higher the "density" of objects. The star at (0,0) and the planet at (1,0) are shown with large and small circles. From left to right: dependence on eccentricity, $e = 0.1$, 0.25, 0.5, and 0.75. From top to bottom: dependence on the libration amplitude, $A = 0.1\pi$ (18°), 0.3π (54°), and π (180°).

& Dermott, 1999; Kuchner & Holman, 2003). The middle panels show how a larger libration amplitude dithers the distribution. Finally, the lowest panels with $A = 180°$ that correspond to a nonresonant case become rotationally-symmetric. Note that the distributions are not radially uniform even in this case: the particle density is higher at the inner and outer edges of each ring. Mathematically, the density there becomes infinitely large, because the radial velocity of particles vanishes in pericentres and apocentres.

Fig. 3.3 shows the complete spatial density distribution, including (3.13) for different resonances, libration widths and maximum eccentricities. Instead of loopy structures there are clumps now, which are sometimes more pronounced, e.g. top left, sometimes smeared an fuzzy, e.g. top right. The larger e_{max} and the larger the libration width A, the more fuzzy the structures become.
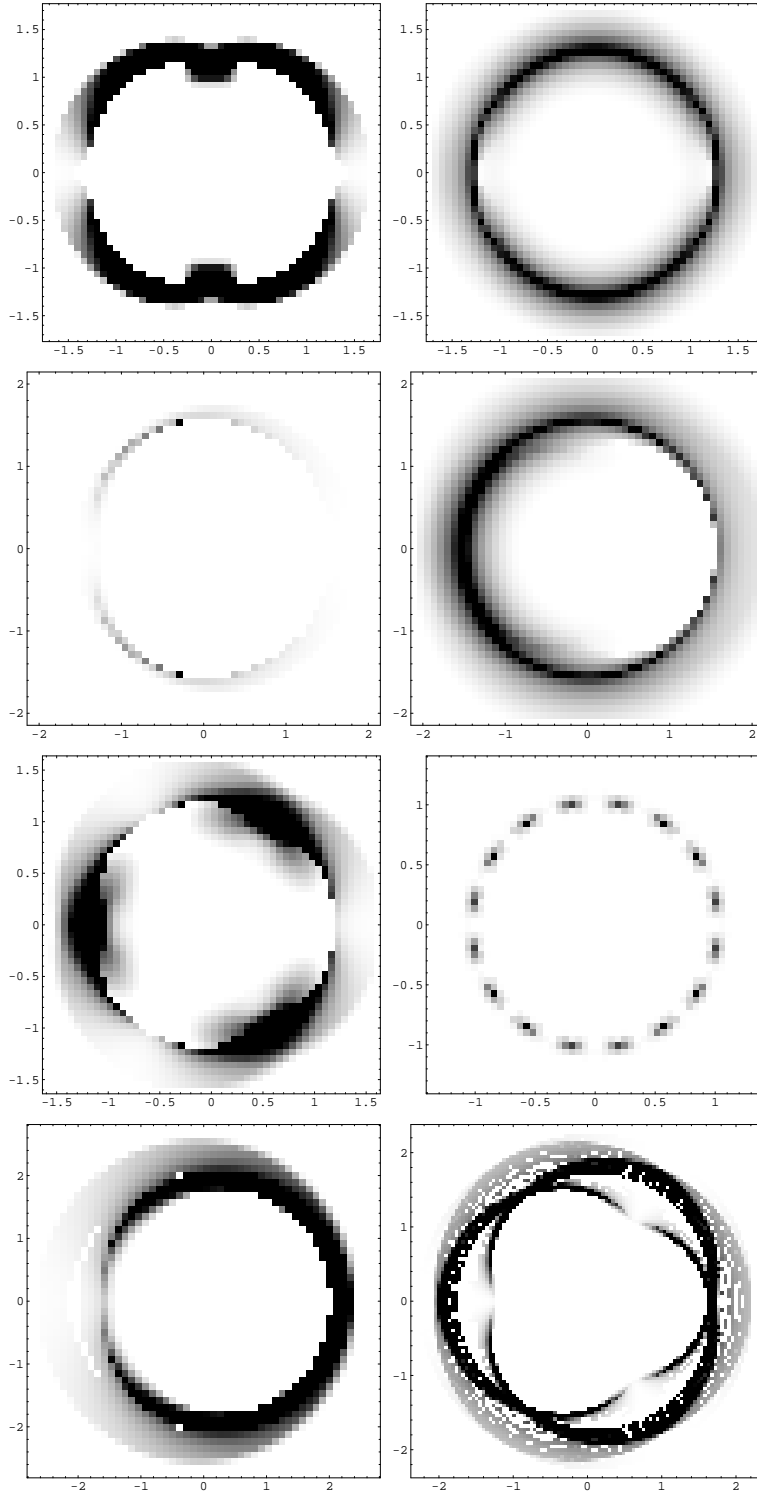
Figure 3.3: Complete density distributions (3.12) combined with (3.13) of resonant ensembles, the very same ones as Fig. 2.6 and 2.7. For each one the star is at (0,0), the planet at (1,0). Top panel: 3:2 resonance with maximum eccentricity 0.2 (left) and 0.5 (right), libration width in both cases is $A = 0.1\pi$. Second panel: 2:1 resonance with maximum eccentricity 0.2, but $A = 0.1\pi$ (left) and 0.4π (right). Third panel: 4:3 ($e_{\max} = 0.3$, $A = 0.1\pi$) and 16:15 resonance ($e_{\max} = 0.1$, $A = 0.01\pi$). Bottom panel: Higher order resonances ($q > 1$), 3:1 on the left and 7:2 on the right ($e_{\max} = 0.3$, $A = 0.1\pi$ both cases).

3.4 Collisions

3.4.1 Collision Condition

In the frame of our model, the disc particles collide, when their positions coincide. Physically speaking these are face-on collisions. Grazing collisions, where the radius of target and projectile must be kept in mind will not be considered explicitely here. As they tend to propel both colliders from the ensemble in question they will be destructive in our sence, too (see sec. 3.2). Thus, in terms of radius vectors, the collision condition is trivial: $\mathbf{r}_1 = \mathbf{r}_2$, meaning that distances and true longitudes $\overline{\omega} + \theta$ of both particles coincide:

$$r_1 = r_2 \tag{3.15}$$

$$\overline{\omega}_1 + \theta_1 = \overline{\omega}_2 + \theta_2. \tag{3.16}$$

By applying the equation of conic section and solving for $\overline{\omega}_2$ and θ_2, we get

$$\overline{\omega}_2^c = \theta_1 - \theta_2^c + \overline{\omega}_1 \tag{3.17}$$

$$\cos \theta_2^c = \frac{1}{e_2} \left[\frac{a_2}{a_1} \frac{1 - e_2^2}{1 - e_1^2} (1 + e_1 \cos \theta_1) - 1 \right], \tag{3.18}$$

which splits up into two solutions ("+" and "−") since the arc cosine is not unique. They are

$$\overline{\omega}_2^+ = \theta_1 - \theta_2^+ + \overline{\omega}_1, \qquad \theta_2^+ = \arccos\left[\cos \theta_2^c\right] \tag{3.19}$$

and

$$\overline{\omega}_2^- = \theta_1 - \theta_2^- + \overline{\omega}_1, \qquad \theta_2^- = 2\pi - \arccos\left[\cos \theta_2^c\right]. \tag{3.20}$$

Here we mark particle #1 as projectile an #2 as target. At this point we break the symmetry between the two colliders, although they are perfectly equal from the physical point of view. From the mathematical one they are not. So may the projectile have a circular orbit, the target may not. In the case of $e_2 = 0$, r_2 will equal a_2 for all θ_2 and Eq. (3.15) must be solved for θ_1, a θ_2^c does not exist.

Further mathmatical problems arise if $e_1 > e_2$. Then the part of orbit 1 which is near apocentre is outside of orbit 2 and collision is impossible for any θ_2 if $\theta_1 \approx \pi$. The solution of (3.15) and (3.16) is the empty set.

We will have to keep this in mind when evaluating the Δ-integrals.

3.4.2 Relative Velocity at Collision

To compute the relative velocity $V_{\mathrm{imp}}^k(e_1, \overline{\omega}_1, \theta_1 \ , \ e_2, \overline{\omega}_2, \theta_2)$ of two colliding particles, we start with calculating the velocity vector of either particle. Consider a Cartesian coordinate system centred on the star and with the x-axis pointing towards the particle's

present position, but *not* rotating with the radius vector. The particle's position and velocity in this system are

$$\mathbf{r} = \begin{pmatrix} r \\ 0 \end{pmatrix}, \tag{3.21}$$

$$\mathbf{v} = \begin{pmatrix} v_r \\ v_\phi \end{pmatrix} = \sqrt{\frac{GM}{a(1-e^2)}} \begin{pmatrix} e\sin\theta \\ 1 + e\cos\theta \end{pmatrix}. \tag{3.22}$$

Denoting the velocity vectors of two colliders by $\mathbf{v}_1$ and $\mathbf{v}_2$, the k-th power of the relative velocity is

$$V_{\mathrm{imp}}^k = |\mathbf{v}_1 - \mathbf{v}_2|^k. \tag{3.23}$$

Therefore, the relative velocity can be calculated by simply applying Eq. (3.22) to both colliders, which makes it obvious that $V_{\mathrm{imp}} = V_{\mathrm{imp}}(e_1, \theta_1, e_2, \theta_2)$. Furthermore, at collision, θ_2 is determined by e_1, θ_1, and e_2, see Eq. (3.18). Therefore, the impact velocity depends on three arguments only:

$$V_{\mathrm{imp}} = V_{\mathrm{imp}}(e_1, \theta_1, e_2). \tag{3.24}$$

We refrain from giving an explicit form of V_{imp}^k here, because it is rather lengthy and obtained by a straightforward calculation. It can be found in Appendix B

3.5 General Formalism

3.5.1 Splitting of Variables

The formalism of the Δ-integrals originates from Krivov et al. (2005), it was further developed in Krivov et al. (2006). Following these papers, we now arrange all phase space variables into "useful" ones $\mathbf{p}$ that we keep and "dummy" ones $\mathbf{q}$ that we will average over to reduce the mathematical complexity of our problem. For our calculations, we choose

$$\mathbf{p} = (e), \qquad \mathbf{q} = (\overline{\omega}, \theta). \tag{3.25}$$

Keep in mind that a is a parameter, not a phase space variable. We average over the angles, because we do not want to consider 'snapshots' of the disc and analyse the geometry but rather investigate how the resonant ensemble as a whole behaves. At this point we keep e, the individual eccentricity of the single particles, because the value of that essentially influences the ensemble. As Figs 3.2 and 3.3 show, higher eccentricity will lead to more pronounced clumps on the one hand and on the other hand it allows higher momentary velocities and thus possibly higher collisional velocities.

Later we will also average over e and thus make statements about the whole resonant ensemble, including all eccentricities in $[0, e_{\mathrm{max}}]$.

3.5.2 Δ-integrals

The collision condition (3.15), (3.16) is given in $\mathbf{p}$ and $\mathbf{q}$, but we need $\mathbf{p}$ only. Therefore we average over the unneeded ones and turn Dirac's δ into Δ,

$$\Delta(\mathbf{p}_1, \mathbf{p}_2) \equiv \int_{\mathbf{q}_1} \int_{\mathbf{q}_2} \delta(\mathbf{r}_1 - \mathbf{r}_2)\, \phi_q(\mathbf{q}_1)\phi_q(\mathbf{q}_2) d\mathbf{q}_1 d\mathbf{q}_2. \tag{3.26}$$

Higher momenta of such functions defined at the collisional point can be obtained by adding the relative velocity $V_{\mathrm{imp}}(\mathbf{p}_1, \mathbf{q}_1, \mathbf{p}_2, \mathbf{q}_2)$,

$$\begin{aligned} \Delta^{(k)}(\mathbf{p}_1, \mathbf{p}_2) \equiv \\ \int_{\mathbf{q}_1} \int_{\mathbf{q}_2} V_{\mathrm{imp}}^k(\mathbf{p}_1, \mathbf{q}_1, \mathbf{p}_2, \mathbf{q}_2)\, \delta(\mathbf{r}_1 - \mathbf{r}_2)\, \phi_q(\mathbf{q}_1)\phi_q(\mathbf{q}_2) d\mathbf{q}_1 d\mathbf{q}_2. \end{aligned} \tag{3.27}$$

Each of them already includes the collisional condition through the factor $\delta(\mathbf{r}_1 - \mathbf{r}_2)$.

Krivov et al. (2005, 2006) have shown that using the Δ-integrals the mean value of $V_{\mathrm{imp}}^k(\mathbf{p}_1, \mathbf{q}_1, \mathbf{p}_2, \mathbf{q}_2)$, averaged over all $\mathbf{q}$-variables, can be expressed as

$$V_{\mathrm{imp}}^k(\mathbf{p}_1, \mathbf{p}_2) = \frac{\Delta^{(k)}(\mathbf{p}_1, \mathbf{p}_2)}{\Delta^{(0)}(\mathbf{p}_1, \mathbf{p}_2)}. \tag{3.28}$$

With our choice of variables and setting $k = 1$, Eq. (3.28) takes the form

$$V_{\mathrm{imp}}(e_1, e_2) \equiv \frac{\Delta^{(1)}(e_1, e_2)}{\Delta^{(0)}(e_1, e_2)}, \tag{3.29}$$

which gives the average collisional velocity between two overlapping rings of particles: one with eccentricity e_1 and another one with eccentricity e_2. In which the angular elements of particles distributed in accordance with the resonance condition. An analysis of the dimensions shows that with this denominator $V_{\mathrm{imp}}(e_1, e_2)$ is indeed given in m/s and (3.28) gives the proper, physical collisional velocity.

3.5.3 Meaning of Δ-integrals

According to Krivov et al. (2005), $\Delta^{(0)}$ can be interpreted as the reciprocal of an "effective interaction volume". Consider again two rings formed by two subsets of particles with given eccentricities e_1 and e_2. If S_1 and S_2 are the surface areas of the rings e_1 and e_2, and S_{12} the area of their intersection, then the zeroth integral $\Delta^{(0)}(e_1, e_2)$ is approximately

$$\Delta^{(0)}(e_1, e_2) \approx \frac{S_{12}}{S_1 S_2}.$$

Fig. 3.4 shows a comparison of the actual interaction volume

$$S_{12} = \pi a^2 \left(\min\left((1 + e_1)^2, (1 + e_2)^2\right) - \max\left((1 - e_1)^2, (1 - e_2)^2\right) \right)$$

and the $\Delta^{(0)}$ integral for a 2:1 resonance, once for a weak ($A = 0.5\pi$) and then a strong one ($A = 0.1\pi$), $a = 1$ in all calculations.
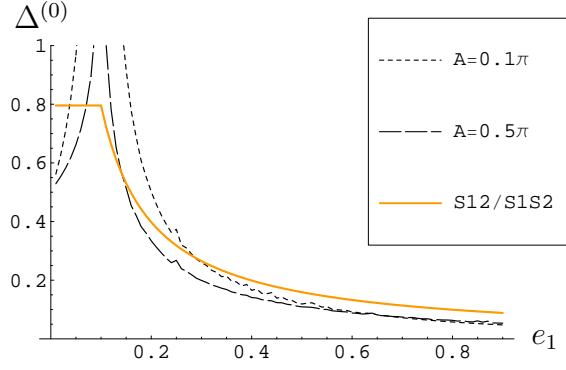
Figure 3.4: Comparison of exact interaction volume (grey) and $\Delta^{(0)}$ (black, for two different libration widths) for a 2:1 resonance, e_2 is set to 0.1.

In the previous section we explained the interpretation of the ratio $\Delta^{(1)}/\Delta^{(0)}$ as the collisional velocity. The integral $\Delta^{(1)}$ can be interpreted directly, too. Since $\Delta^{(1)} = V_{\text{imp}} \times \Delta^{(0)} \sim$ velocity/volume, $\Delta^{(1)}$ gives, after multiplication by the number of particles and their collisional cross section, the collisional rate,

$$
\begin{aligned}
R(e_1, e_2) &= N\sigma V_{\text{imp}}(e_1, e_2)\Delta^{(0)}(e_1, e_2) && (3.30)\\
&= N\sigma\Delta^{(1)}(e_1, e_2). && (3.31)
\end{aligned}
$$

More precisely, this will be the rate of collisions between those particles of the disc with eccentricity e_1 and those with eccentricity e_2.

Later on in this work there will be further comparisons of results obtained with our formalism and those from other methods.

3.5.4   Evaluation of Δ-integrals

For the actual calculation of any Δ-integral we insert (3.24) and (3.25) into (3.27):

$$
\begin{aligned}
\Delta^{(k)}(e_1, e_2) &= \int_{\overline{\omega}_1} \int_{\overline{\omega}_2} \int_{\theta_1} \int_{\theta_2} V_{\text{imp}}^k(e_1, \theta_1, e_2)\\
&\times \quad \delta\left(\mathbf{r}_1 - \mathbf{r}_2\right) && (3.32)\\
&\times \quad \phi_{\overline{\omega}}(\overline{\omega}_1, \theta_1)\,\phi_{\overline{\omega}}(\overline{\omega}_2, \theta_2)\,d\overline{\omega}_1 d\overline{\omega}_2\,d\theta_1 d\theta_2.
\end{aligned}
$$

The δ-function should now be expressed through orbital elements:

$$
\delta\left(\mathbf{r}_1 - \mathbf{r}_2\right) = J^{-1}\delta\left(\overline{\omega}_1 - \overline{\omega}_2\right)\delta\left(\theta_1 - \theta_2\right)\ , \tag{3.33}
$$

where the Jacobian

$$
J = \left|\frac{\partial \mathbf{r}_2}{\partial(\overline{\omega}_2, \theta_2)}\right|
$$

explicitly reads

$$
J = \frac{r^3}{a}\frac{e_2}{1 - e_2^2}|\sin\theta_2| = a^2\,\frac{e_2(1 - e_2^2)^2|\sin\theta_2|}{(1 + e_2\cos\theta_2)^3}\ . \tag{3.34}
$$

Incorporating this into (3.32) and paying respect to the collision condition, we get

$$
\begin{aligned}
\Delta^{(k)}(e_1, e_2) &= \int_{\overline{\omega}_1} \int_{\overline{\omega}_2} \int_{\theta_1} \int_{\theta_2} V_{\mathrm{imp}}^k(e_1, \theta_1, e_2) \\
&\times \frac{1}{a^2} \frac{(1 + e_2 \cos \theta_2)^3}{e_2(1 - e_2^2)^2 |\sin \theta_2|} \delta\left(\overline{\omega}_2 - \overline{\omega}_2^c\right) \delta(\theta_2 - \theta_2^c) \\
&\times \phi_{\overline{\omega}}(\overline{\omega}_1, \theta_1)\, \phi_{\overline{\omega}}(\overline{\omega}_2, \theta_2)\, d\overline{\omega}_1 d\overline{\omega}_2\, d\theta_1 d\theta_2.
\end{aligned}
\tag{3.35}
$$

This is the general, explicit version of Eq. (3.27), the numerical solution of which would be possible, the 4-time integration making in cumbersome, however.

3.5.5 Transformation of Δ-integrals

Here, we will transform Eq. (3.35) to a form more suitable for efficient numerical calculations.

Two out of four integrations in Eq. (3.35), those over $\overline{\omega}_2$ and θ_2, can be done immediately with the help of the two-branch collision condition. Since $\cos \theta_2^+ = \cos \theta_2^- = \cos \theta_2^c$ and $|\sin \theta_2^+| = |\sin \theta_2^-| = |\sin \theta_2^c|$ we obtain:

$$
\begin{aligned}
\Delta^{(k)}(e_1, e_2) &= \frac{1}{a^2 e_2 (1 - e_2^2)^2} \int_0^{2\pi} d\theta_1 \frac{(1 + e_2 \cos \theta_2^c)^3}{|\sin \theta_2^c|} \\
&\times \sum_{\pm} V_{\mathrm{imp}}^{\pm\ k}(e_1, \theta_1, e_2) \int_0^{2\pi} d\overline{\omega}_1 \phi_{\overline{\omega}}(\overline{\omega}_1, \theta_1) \phi_{\overline{\omega}}(\overline{\omega}_2^c, \theta_2^c).
\end{aligned}
\tag{3.36}
$$

The superscript "c" of $\overline{\omega}_2^c$ and θ_2^c will be omitted from now on. We stress, however, that both are functions of $e_1, \overline{\omega}_1, \theta_1$, and e_2, as calculated from Eqs (3.17) and (3.18). We insert the distribution function $\phi_{\overline{\omega}}$, (3.12), and the solution of the collision condition (3.18) – (3.20). The Δ-integral now takes the form

$$
\begin{aligned}
\Delta^{(k)}(e_1, e_2) &= \frac{(1 - e_1^2)^{1/2}(1 - e_2^2)^{1/2}}{16\pi^2 A^2 a^2} \int_0^{2\pi} d\theta_1 \frac{1}{|e_2 \sin \theta_2|(1 + e_1 \cos \theta_1)} \\
&\times \sum_{\pm} V_{\mathrm{imp}}^{\pm\ k}(e_1, \theta_1, e_2) \int_0^{2\pi} d\overline{\omega}_1\ H_1\ H_2
\end{aligned}
\tag{3.37}
$$

where the Heaviside functions

$$
H_j = H\left[\Phi_0 - A < \Phi_j < \Phi_0 + A\right], \qquad j = (1, 2)
\tag{3.38}
$$

describe libration of resonant arguments Φ_1 and Φ_2 around Φ_0 (e.g. π or 0).

The integral $\int d\overline{\omega}_1 H_1 H_2$ is analytically solvable. In principle we only need to find an analytic expression of the overlap of the two intervals where H_1 and H_2 both render one. In Appendix B of Queck et al. (2007) this is done with the help of the shift function $\Delta\chi$. It is measured modulo 2π and explicitly reads

$$
\Delta\chi = \left\{(p + q)\left[M(e_2, \theta_2) - M(e_1, \theta_1)\right] - p(\theta_2 - \theta_1)\right\}_{2\pi}.
\tag{3.39}
$$

$M = M(e, \theta)$ is the mean anomaly given by Eqs. (3.10)–(3.11). $\Delta\chi$ is the difference of deviations of the respective resonant arguments Φ of the two colliders from the centre of libration Φ_0 . As you can see, the centre of libration itself is ruled out here, thus its actual value is of no consequence.

The result obtained for $\int d\overline{\omega}_1 H_1 H_2$ in Queck et al. (2007) consists of two branches. The first one is

$$
\int_0^{2\pi} d\overline{\omega}_1 H_1 H_2 \;=\; 2\,A\,\left(1 \;-\; \frac{|\Delta\chi|}{2A}\right)\,H\left[1 \;-\; \frac{|\Delta\chi|}{2A}\right]
$$
$$
1 + \frac{|\Delta\chi|}{2A} \leq \frac{\pi}{A}. \tag{3.40}
$$

It is always taken for $A \leq \pi/2$.

The other branch of the integral is

$$
\int_0^{2\pi} d\overline{\omega}_1 H_1 H_2 = 2\,A\,\left(2 \;-\; \frac{\pi}{A}\right), \qquad 1 + \frac{|\Delta\chi|}{2A} \geq \frac{\pi}{A}. \tag{3.41}
$$

Note that $|\Delta\chi| \leq \pi$ and $A \leq \pi$. In the nonresonant limiting case $A = \pi$ we obtain $\int d\overline{\omega}_1 H_1 H_2 = 2A$.

The final result for the first branch is:

$$
\begin{aligned}
\Delta^{(k)}(e_1, e_2) \;=\;& \frac{(1 - e_1^2)^{1/2}(1 - e_2^2)^{1/2}}{8\pi^2 A a^2} \\
&\times\; \int_0^{2\pi} d\theta_1 \frac{1}{|e_2 \sin\theta_2|(1 + e_1 \cos\theta_1)} \\
&\times\; \sum_{\pm} V_{\mathrm{imp}}^{\pm\;k}(e_1, \theta_1, e_2)\left(1 \;-\; \frac{|\Delta\chi^{\pm}|}{2A}\right) \\
&\times\; H\left[1 \;-\; \frac{|\Delta\chi^{\pm}|}{2A}\right],
\end{aligned} \tag{3.42}
$$

and similar to that for the second branch. The only remaining integral is evaluated numerically using a Monte-Carlo method.

The above calculation assumes that the distribution of the resonant argument within the libration band is uniform, Eq. (3.12). If necessary, it can be repeated with a more realistic distribution. It is sufficient to replace the Heaviside function in Eq. (3.12) by another function $f(\{\Phi - \Phi_0\}_{2\pi})$, for instance a trigonometric one or a Gaussian, and re-do the calculation (3.36) – (3.42).

3.5.6   Limiting Cases of Δ-integrals

We consider two limiting cases of special interest of the Δ-integral: the perfect resonant lock $A = 0$ and the equality of the eccentricities of the colliders $e_1 = e_2$. The first part is a rather academic problem, in real astrophysical ensembles there will always be certain deviations. It will be, however, a good check for our numerically solved integrals with small, nonzero A. In the second case, $e_1 = e_2$, we need to be sure there exists a finite

limit so that $\Delta_{(k)}(e_1, e_2)$ can be smoothly continued for *all* e_1, e_2 as the physics demand. Eq. (3.42) and its counterpart for $A > \pi/2$ in that form are not valid for $e_1 \equiv e_2$.

We follow the analysis given in Appendix B of Queck et al. (2007) and begin with the limit $A \to 0$ and start at Eq. (3.40):

$$\lim_{A \to 0} \int_0^{2\pi} \mathrm{d}\overline{\omega}_1 H_1 H_2 = 4 \, A^2 \, \delta(\Delta\chi), \tag{3.43}$$

which completely eliminates the A dependence, since the prefactors of the integral (3.37) and (3.42) contain A^{-2}. Thus the $A \to 0$ limit of the Δ-integral is finite,

$$\lim_{A \to 0} \Delta^{(k)} < \infty \, .$$

Furthermore, the δ-function immediately resolves the remaining integral over θ_1 to an explicit expression. Since

$$\delta(\Delta\chi(\theta_1)) = \sum_i \left| \frac{\partial \Delta\chi(\theta_1)}{\partial \theta_1} \right|^{-1} \delta(\theta_1 - \theta_1^{(i)}), \tag{3.44}$$

the only task left is the calculation of the $\theta_1^{(i)}$ which are given as the roots of the equation $\Delta\chi(\theta_1^{(i)}) = 0$. In practice, the calculation of Eq. (3.44) is cumbersome, as it requires the inversion of the Kepler equation (3.10).

We now turn to the second part, the $e_2 \to e_1$ limit, confining our analysis to the case $\Delta^{(1)}$. Considering the collision condition (3.18) for the case $e_1 = e_2$ – and remembering $a_1 = a_2 = a_{\mathrm{res}}$ – we find that

$$\cos \theta_2^c \;\; = \;\; \cos \theta_1,$$

meaning collision is only possible if

$$\theta_2^c \;\; = \;\; \pm\theta_1.$$

With this result and the other half of the collision condition (3.17) there are two branches of the limit $e_2 \to e_1$ of (3.35). They render

$$\lim_{e_2 \to e_1} \frac{V_{\mathrm{imp}}{}^+}{|e_2 \sin \theta_2{}^+|} \;\; = \;\; 0, \tag{3.45}$$

$$\lim_{e_2 \to e_1} \frac{V_{\mathrm{imp}}{}^-}{|e_2 \sin \theta_2{}^-|} \;\; = \;\; \frac{2}{\sqrt{1 - e_1^2}} \, V_{\mathrm{kepler}}. \tag{3.46}$$

Here, the "$\pm$" branches of the collision condition have slightly different meaning than in (3.19)–(3.20). With the superscript "$+$" we denote the case $\theta_2^c \to \theta_1$, and with "$-$" we denote $\theta_2^c \to -\theta_1$. For the remaining nonzero "$-$" branch, equation (3.43) has to be evaluated. The condition $\Delta\chi(\theta_1^{(i)}) = 0$ is satisfied at $\theta_1^{(1)} = 0$ and $\theta_1^{(2)} = \pi$.

The integral $\Delta^{(1)}$ is again finite, except when

$$\left. \frac{\partial \Delta\chi(\theta_1)}{\partial \theta_1} \right|_{\theta_1 = \theta_1^{(i)}} = 0, \tag{3.47}$$

because

$$\delta\left(\Delta\chi(\theta_1)\right) = 0 \tag{3.48}$$

for *all* θ_1 then.

Setting $e_1 = e_2 =: e_\star$ and inserting $\sin\theta_1^{(i)} = 0$ it reduces to

$$(p+q)\frac{\partial M(e_\star,\theta_1)}{\partial\theta_1}\bigg|_{\theta_1=\theta_1^{(i)}} = p. \tag{3.49}$$

The case with $\theta_1^{(2)} = \pi$ does not have a solution, while for $\theta_1^{(1)} = 0$ the equation takes the form

$$\frac{\sqrt{1+e_\star}}{(1-e_\star)^{3/2}} = \frac{p+q}{p}. \tag{3.50}$$

Evaluating that for some examples of (p,q) we get

$$(p,q) = (1,1) \quad \text{gives} \quad e_\star = 0.31$$
$$(p,q) = (2,1) \quad \text{gives} \quad e_\star = 0.19$$
$$(p,q) = (3,1) \quad \text{gives} \quad e_\star = 0.14$$
$$(p,q) = (3,2) \quad \text{gives} \quad e_\star = 0.24.$$

Eq. (3.44) implies that $\Delta^{(1)}$ is infinite at those points $e_1 = e_2 = e_\star$ – since now $\delta(\Delta\chi(\theta_1))$ is 0 and according to (3.42) $\Delta^{(1)} \sim A^{-2}$. This singularity is an integrable one, though. After averaging over both arguments the Δ-integral will be finite again.

It does, however, have a maximum there. They will be illustrated later in this work (cf. Figs 3.9 or 3.10). As a result, the maxima seen later in this work for small, non-zero A (Fig. 3.10) will *not* grow infinitely large when $A \to 0$.

There is an explicit analytic representation of this limit for some special cases. E.g. if $q \geq 1$ the limit of the perfect resonance and minuscule eccentricities is

$$\lim_{A\to 0, e_1\to 0, e_2\to 0} \Delta^{(1)} = \frac{V_{\text{kepler}}}{2\pi^2 a^2}. \tag{3.51}$$

We note that all of the equations in this section hold for the case $q = 0$ (1:1 resonance, Trojans) as well, except when an explicit $1/q$ appears. In particular, $q = 0$ in Eq. (3.50) leads to $e_\star = 0$, which agrees with Fig. 3.12.

So far, we considered the limiting cases of the integral $\Delta^{(1)}$. Of course, $\Delta^{(0)}$ is not less important, because it is needed to calculate the collisional velocity, see Eq. (3.29). For $k = 0$ the "+" branch (Eq. (3.45)) diverges when $e_1 \to e_2$. Therefore, $\Delta^{(0)}$ also diverges, and the collisional velocity (3.29) goes to zero (see Fig. 3.5). As it should as $\theta_1 = \theta_2$ also, and thus both orbits coincide and make collisions impossible.

3.5.7   Properties of Δ-integrals

The analysis of the equations of the above sections allows us to establish several useful properties of the Δ-integrals, and therefore the collisional velocities and rates.

1. The Δ-integral is symmetric with respect to its arguments. Although it is not quite evident from (3.35), one can use Eq. (3.18) to change the integration variable from θ_1 to θ_2. The result will be identical to $\Delta(e_2, e_1)$, and therefore $\Delta(e_2, e_1) = \Delta(e_1, e_2)$. Of course, we have also tested the symmetry numerically.

2. As Eq. (3.42) readily shows, the transformed Δ integral depends on the libration width A, but does not depend on the libration centre Φ_0.

3. It is possible to calculate limiting cases of Eq. (3.42) and to get an idea of how large the effect of resonance on collisional velocities and rates could be (Sec. 3.5.6). The limit of the Δ-integral at $A \to 0$ is finite, and close to the values obtained in the following sections with small, but non-zero A.

4. The same holds for the limit of the Δ-integral at $e_1 \to e_2$: it is finite and is not far from the values calculated for close, but not equal e_1 and e_2.

3.6   Collisional Velocities

3.6.1   Collisional Velocity for the Subsets of Particles with $e = e_1$ and $e = e_2$

In this section, we show numerical results for the collisional velocity $V_{\text{imp}}(e_1, e_2)$, calculated with the aid of (3.29) and (3.42). Recall that this velocity is the average collisional velocity between two subsets of particles in the resonant family: one with eccentricity e_1 and another one with eccentricity e_2.

In the left and right columns of figure 3.5 shows this velocity as a function of one of its two arguments, with the second argument fixed to $e_2 = 0.1$ and $e_2 = 0.2$, respectively. The velocity is measured in units of the circular Keplerian velocity, $V_{\text{kepler}} \equiv \sqrt{GM/a}$. The major effect seen in these plots is that $V_{\text{imp}}(e_1, e_2)$ decreases from e_2 at $e_1 = 0$ to zero at $e_1 = e_2$ and then increases again.

The panels show three 1st order resonances of different strength, weak ones at the top and strong ones at the bottom. Different curves correspond to different resonance numbers p and q. Although the resonant lock does affect the velocities, is it somewhat surprising that the effect is rather subtle and makes comparably small quantitative difference to the nonresonant case.

Fig. 3.6 depicts the velocity in the e_1-e_2-plane. The upper panel for a strong resonance shows, as expected, a sharp minimum along the line of equal eccentricities and an extended area of low collisional velocity where both eccentricities are low, $e_1, e_2 \sim 0 \dots 0.2$. As far as other regions of the plane are concerned, the effects are highly non-linear. Particularly
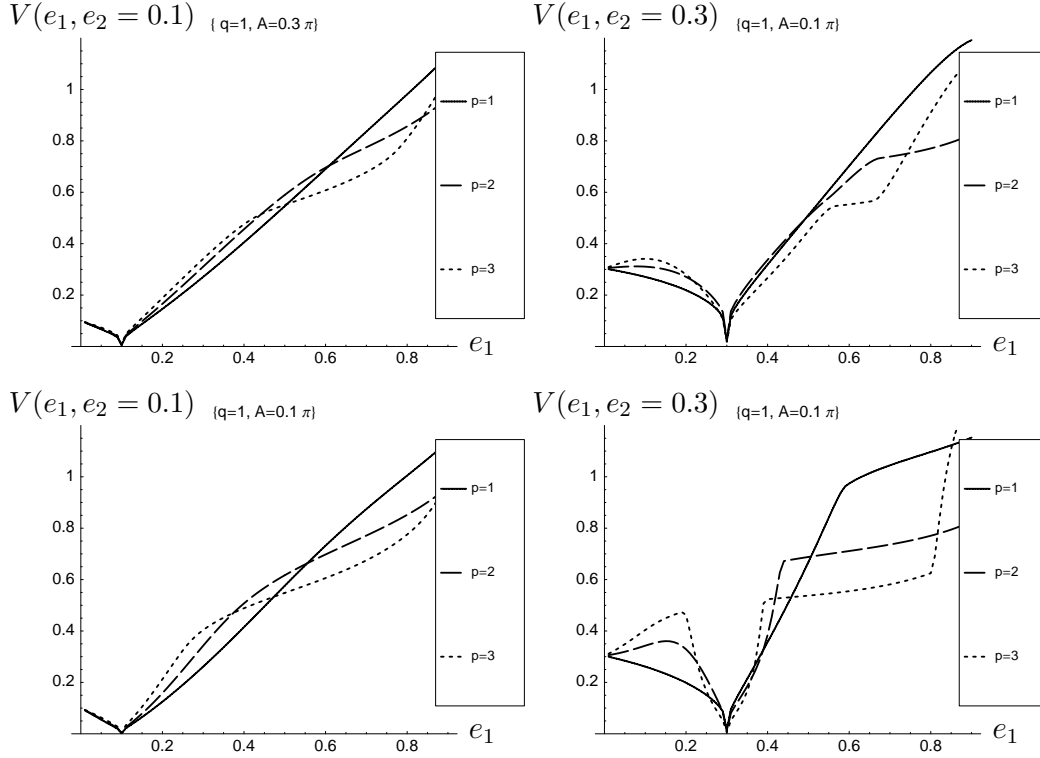
Figure 3.5: Cuts through the contour plots of collisional velocity $V_{\mathrm{imp}}(e_1, e_2)$ (in units of V_{kepler}) for fixed e_2. Left panels: a lower value of $e_2 = 0.1$, right panels: a higher one of $e_2 = 0.3$. Plotted are the 2:1 resonance (solid), 3:2 (dashed), 4:3 (dotted) in every panel. Top: a weaker resonance with $A = 0.3\pi$, bottom: a strong one with $A = 0.1\pi$.

interesting is a sharp increase of the collisional velocity from moderate to large eccentricities that occurs for 3:2 and 4:3 resonances. It is due to the fact that, starting from a certain e, the resonant "clumps" start to overlap, see two right-most panels in the middle row of Fig. 3.2. The larger p is the smaller the eccentricity at which the effect shows up, because a $(p + q) : p$ resonance produces p clumps. The larger the number of clumps, the easier it is for them to overlap. The same effects, in a weaker form, are seen in the middle panels that are drawn for a shallower resonance. The velocity is highest in collisions between particles in highly eccentric orbits with those in moderately eccentric ones. In the nonresonant case depicted in the lowest panels, the highest velocity is attained in collisions between particles in highly eccentric orbits with those in nearly circular ones. The maximum possible value of $V_{\mathrm{imp}}(e_1, e_2)$ is $\sqrt{2}$. It is achieved asymptotically when $e_1 = 0$ and $e_2 \to 1$.

3.6.2   Average Collisional Velocity in the Disc

After investigating the interaction of subsets, we now calculate the average collisional velocity in the *whole* disc of particles. This is accomplished by integrating $V_{\mathrm{imp}}(e_1, e_2)$ over both e_1 and e_2 from 0 to e_{max}, distributed according to Eq. (3.13). In this a way,
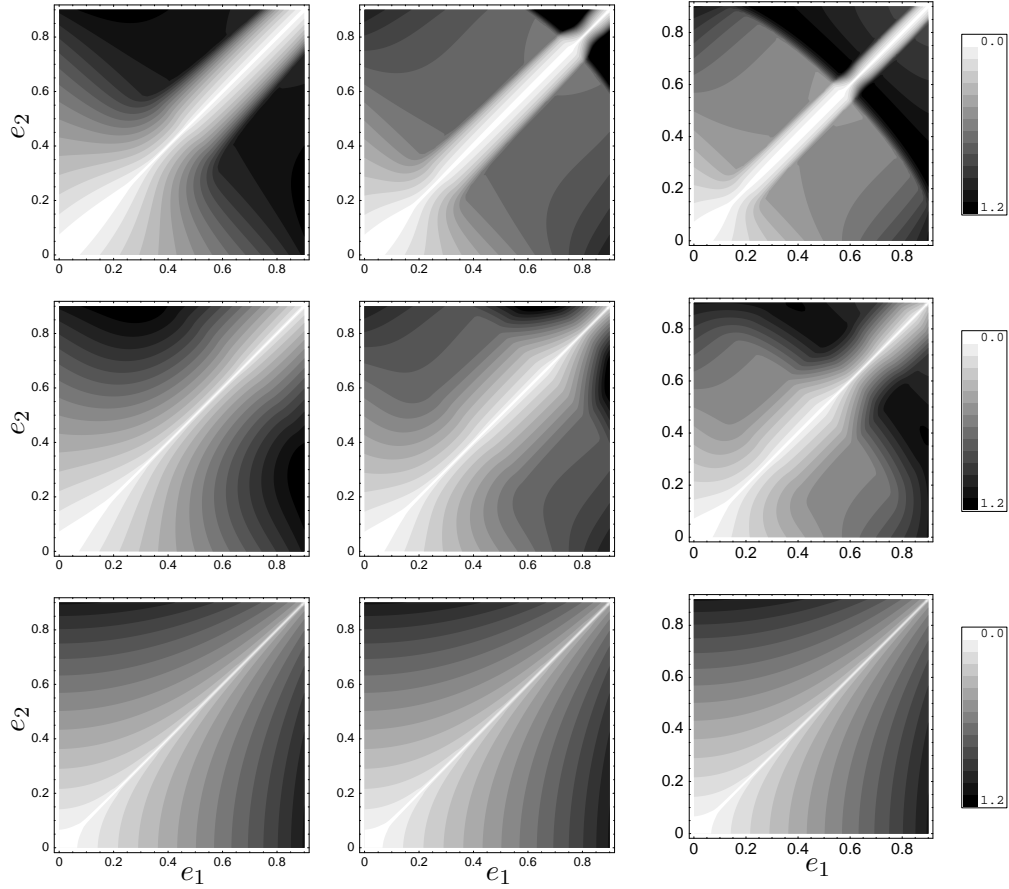
Figure 3.6: Contour plots of collisional velocity $V_{\mathrm{imp}}(e_1, e_2)$, in units of V_{kepler}, for the 2:1 resonance (left), 3:2 (middle), 4:3 (right) with libration width $A = 0.1\pi$ (top), $A = 0.3\pi$ (middle), and $A = \pi$ (bottom, non-resonance case). Darker regions correspond to higher velocities.

we get the average collisional velocity in the disc as a function of the maximum possible eccentricity,

$$V_{\mathrm{imp}}(e_{\max}) =$$
$$\int_{e_1} \int_{e_2} \frac{\Delta^{(1)}(e_1, e_2)}{\Delta^{(0)}(e_1, e_2)} \phi_e(e_1; e_{\max}) \phi_e(e_2; e_{\max}) de_1 de_2 . \tag{3.52}$$

The additional double integration is performed numerically with a Monte-Carlo method.

Fig. 3.7 (top) shows the dependence on the libration width of the resonant argument. The smaller A is the stronger the resonance – and its influence – becomes. $A = \pi$ describes a nonresonant case, whereas $A = 0$ corresponds to a perfect resonant lock. Again, the collisional velocity is affected by the resonance only weakly, but the effect is present. It is interesting that for moderate eccentricities, the average collisional velocity in a resonant belt is lower than in a similar nonresonant one, while for large eccentricities, the opposite is true. Similarly, middle and bottom panels in Fig. 3.7 demonstrate the dependence of V_{imp} on p and q. They show that collisional velocity does vary with the resonant integers,
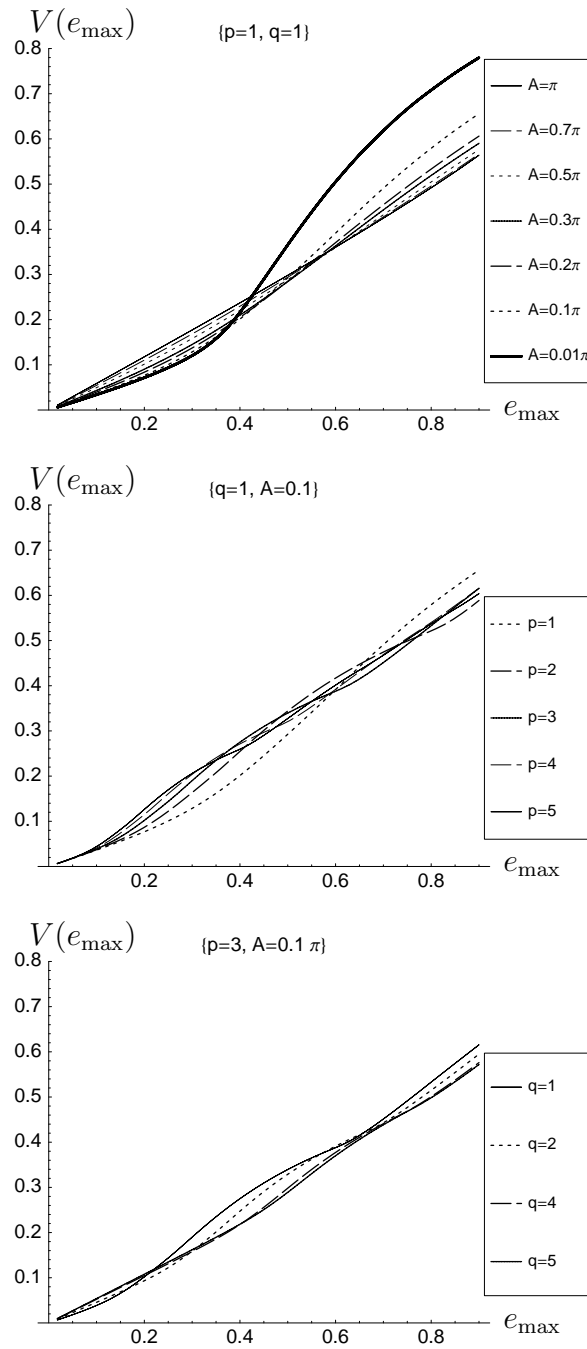
Figure 3.7: Collisional velocity $V_{\mathrm{imp}}(e_{\max})$ in units of V_{kepler}. Top: dependence on libration width A width for the 2:1 resonance. Middle: dependence on resonance parameter p for first-order resonances $q = 1$ with $A = 0.1\pi$. Bottom: dependence on the order of resonance q for $p = 3$ and $A = 0.1\pi$.

and may be both higher or lower that the nonresonant one, but the effect is usually of the order of several tens of percent.

3.7 Collisional Rates and Collisional Lifetimes

Using the same methods as in the previous section, we will now investigate the influence of a resonance on the frequency of collisions. Since the number density of the particles in the resonant "clumps" is higher than in a similar nonresonant belt one might expect the collisional rate to be higher, too. We check whether, and to what extent, this expectation is true.

3.7.1 Collisional Rate for the Subsets of Particles with $e = e_1$ and $e = e_2$

Like in the case of collisional velocity, we start by considering two subsets of particles in the resonant family: one with eccentricity e_1 (n_1 particles) and another one with eccentricity e_2 (n_2 particles) and "count" collisions between particles of population 1 with those of population 2. The rate of collisions is given by (see Krivov et al., 2005, 2006),

$$R(e_1, e_2) = N\sigma V_{\text{imp}}(e_1, e_2)\Delta^{(0)}(e_1, e_2),$$ (3.53)

which simplifies – with Eq. (3.28) – to

$$R(e_1, e_2) = N\sigma\Delta^{(1)}(e_1, e_2).$$ (3.54)

Here, σ is the collisional cross section for equal-sized particles, and the front factor N depends on what we mean by "collisional rate". If $R(e_1, e_2)$ is the number of collisions per unit time that a single particle of population 1 has with any particle of population 2, then $N = n_2$. Conversely, if we consider a particle of population 2 colliding with population 1 particles, then $N = n_1$. Finally, to get the total number of collisions between all particles of both families occurring per unit time, we should set $N = n_1 n_2$.

However, the above formulas are two-dimensional. For instance, σ should be understood as $2s$, where s is the radius of equal-sized particles. Any physically meaningful calculation of collisional frequencies requires a 3D treatment. We thus introduce an approximation for a 3D Δ-integral,

$$\Delta_{\text{3D}}^{(k)}(.) \equiv \frac{\Delta^{(k)}(.)}{h},$$ (3.55)

where $h = 2r\sin\epsilon \approx 2a_{\text{res}}\sin\epsilon$ is the disc thickness at the annulus location, ϵ being the half-opening angle of the disc. The 3D collision rate thus is

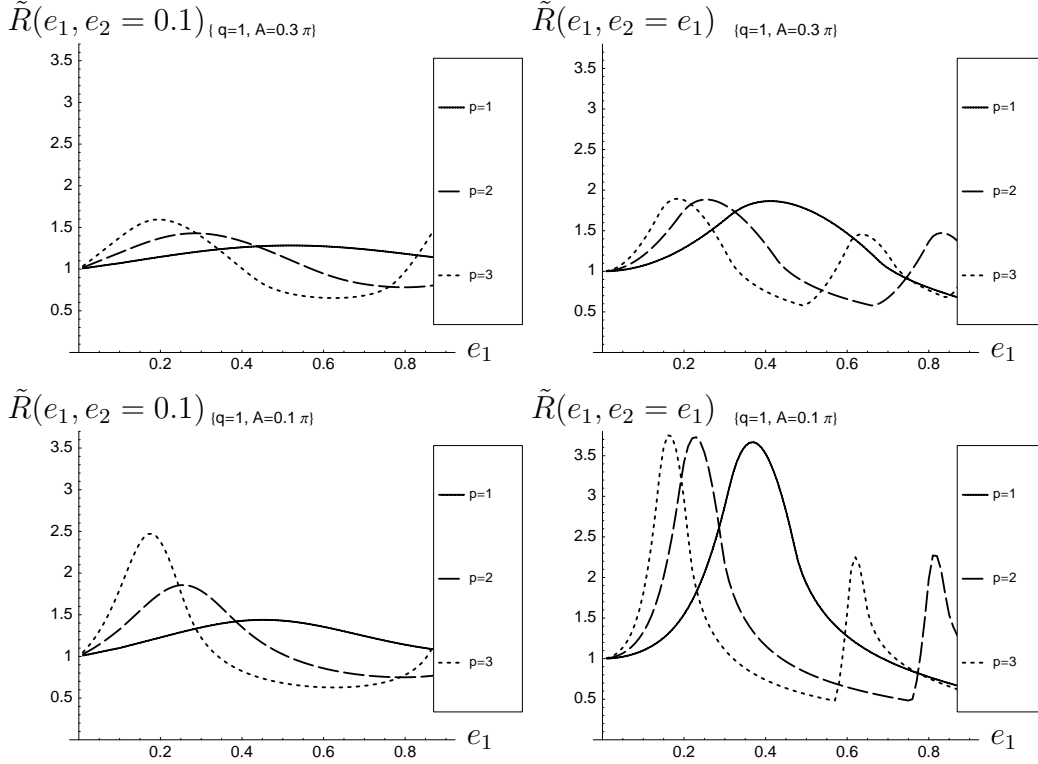$$R(e_1, e_2) = N\sigma\Delta_{\text{3D}}^{(1)}(e_1, e_2),$$ (3.56)

Figure 3.8: Cuts through the contour plots of collisional rate $\tilde{R}(e_1, e_2)$ for fixed $e_2 = 0.1$ on the left and along the line of equal eccentricities $e_1 = e_2$ on the right. Plotted are the 2:1 resonance (solid), 3:2 (dashed), 4:3 (dotted) in every panel. Top: a shallower resonance with $A = 0.3\pi$, bottom: a strong one with $A = 0.1\pi$. The shift of the maxima to lower e_1 for larger p is quite pronounced. Some further, local maxima appear in the case $p = 3$.

now with the "usual" collisional cross section $\sigma = 2\pi s^2$. We note that $\Delta_{3D}^{(1)}$, i.e. R without the factor $N\sigma$, is exactly what is usually called "intrinsic collisional probability" (e.g. Greenberg, 1982; Davis & Farinella, 1997).

Instead of dealing with the full collisional rate (3.56), it is convenient to introduce a dimensionless one $\tilde{R}(e_1, e_2)$,

$$\tilde{R}(e_1, e_2) \equiv R(e_1, e_2)/R_0, \tag{3.57}$$

where

$$R_0 \equiv \frac{1}{2\pi^2} \frac{N\sigma V_{\text{kepler}}}{h \, a_{\text{res}}^2} \tag{3.58}$$

is the approximate "particle-in-a-box" value of the collisional rate To first order, R_0 does not depend on eccentricities of the colliding particles and depends on their inclinations through the divisor h only. It describes the rate of collisions in a nonresonant, and therefore rotationally-symmetric, ring of objects. Again, $R_0/(N\sigma)$ is the intrinsic collisional probability in such a ring. Thus $\tilde{R}$ contains all the nonsymmetric effects, especially those of the mean motion resonance. Via its deviations from unity it enables us to study the
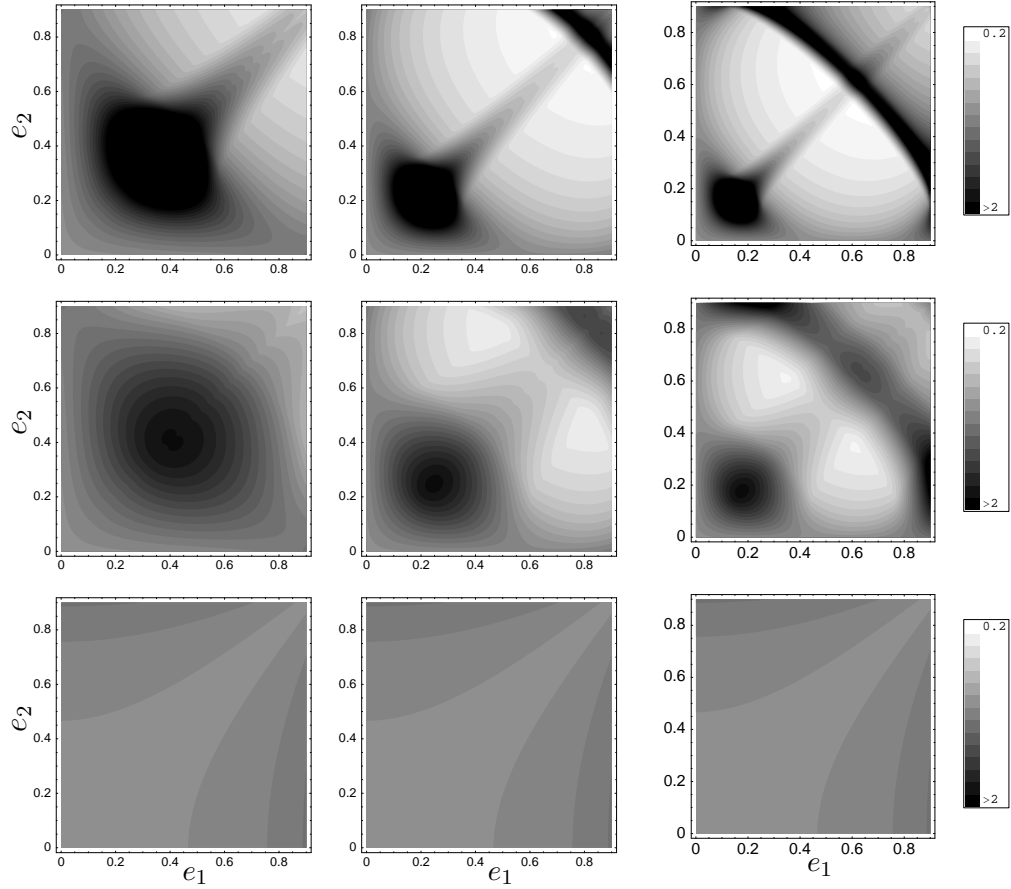
Figure 3.9: Contour plot of the dimensionless collisional rate $\tilde{R}(e_1, e_2)$, for the 2:1 resonance (left), 3:2 (middle), 4:3 (right) with libration $A = 0.1\pi$ (top), $A = 0.3\pi$ (middle), and $A = \pi$ (bottom, non-resonance case). The darker the contours, the higher the rate.

influence of a resonance without having to specify the disc. There are some corrections due to non-zero eccentricities, too. The value of which can be determined by studying the nonresonant $\tilde{R}|_{A=\pi}$.

The two columns of Figure 3.8 show the dimensionless collisional rate $\tilde{R}(e_1, e_2)$ as a function of one of its two arguments, left with the second argument fixed to $e_2 = 0.1$ and right with $e_2 \simeq e_1$, respectively. To avoid the singularity of (3.35) at $e_1 = e_2$ we calculated only up to $e_2 = 0.9999\,e_1$. For larger A, i.e. for a weaker resonance, shown in the top panels, the collisional rate is almost independent of e_1, being close to the "particle-in-a-box" value. For stronger resonances (bottom panels) $\tilde{R}(e_1, e_2)$ peaks at intermediate values of eccentricity e_1. The stronger the resonance, the more pronounced the maximum. For the 2:1 resonance at $e_2 = 0.3$ and $A = 0.1\pi$, the maximum collisional rate at $e_1 \sim 0.4$ is about 3.75 times larger than the nonresonant rate. Interestingly, the larger the resonant integer p, the smaller the value of eccentricity at which the collisional rate is the highest. Another finding is that, for sufficiently large eccentricities, resonances may decrease the frequency of collisions.

Fig. 3.9 depicts the collisional rate in the e_1-e_2-plane. Again, we excluded a region of width $2\ 10^{-4}$ around $e_1 = e_2$ and smoothed the graph over this small gap. The upper and middle panels show that within resonance collisions are most frequent between particles, whose orbital eccentricities are moderate and not very different from each other. Interestingly, these are exactly the eccentricities for which collisional rates in the nonresonant case are the lowest (bottom panels). For some resonances, another region of higher collisional rates is observed at very high eccentricities. This effect has the same origin as a similar effect in the collisional velocities, see Fig. 3.6.

3.7.2 Average Collisional Rate in the Disc

Like in the case of collisional velocity, we now average over both eccentricities in order to obtain the collisional rate in the whole disc containing N objects:

$$
\begin{aligned}
R(e_{\max}) = \\
N\sigma \int_{e_1} \int_{e_2} \Delta_{3D}^{(1)}(e_1, e_2)\phi_e(e_2; e_{\max})\phi_e(e_1; e_{\max})de_2 de_1.
\end{aligned}
\tag{3.59}
$$

Again, the front factor N depends on what we intend to describe. If $R(e_{\max})$ is the number of collisions per unit time that a certain particle may have with all other particles in the belt, then $N = n$. To get the total number of all collisions, meaning every particle with every other one, occurring in the ring per unit time, we should set $N = n^2/2$.

Figure 3.10 shows the numerical results. Again we split off R_0, so that

$$
\tilde{R}(e_{\max}) \equiv R(e_{\max})/R_0
\tag{3.60}
$$

The top panel focuses on the influence of the libration width A, whereas the middle and bottom ones illustrate the dependence on p and q. It is seen that $R(e_{\max})$, although all the curves are generally flatter than the non-averaged ones, has qualitatively the same properties as $R(e_1, e_2)$: independence of $e_{\max}$ out of resonance and a maximum at intermediate eccentricities for deeper resonances. The maxima shift to slightly lower eccentricities, when either the libration width decreases, p increases, or the order of resonance q decreases.

To understand those properties we go back to section 3.5.6. There, among other results, we obtained a formula in Eq. (3.50) for the position $e_\star$ of the maxima in the case $A \to 0$ and gave some examples for different p and q.

A comparison with the maxima in Fig. 3.10 shows that the plotted ones lie slightly to the right of the positions $e_\star$ calculated by (3.50). As is expected since we have plotted $\tilde{R}(e_{\max})$ for several small, but still non-zero A, while (3.50) is valid for $A \equiv 0$. We see, however, how $\tilde{R}(e_{\max})$ approaches this limit for decreasing A, as the the maximum shifts to smaller $e_{\max}$ as A decreases. We extracted the actual values fo the maxima $\tilde{R}(e_{\max})|_{\max}$ and their respective positions for different A of the 2:1 resonance shown in the uppermost panel of Fig. 3.10. They are plotted in Fig. 3.11 and show that the heights seem to grow
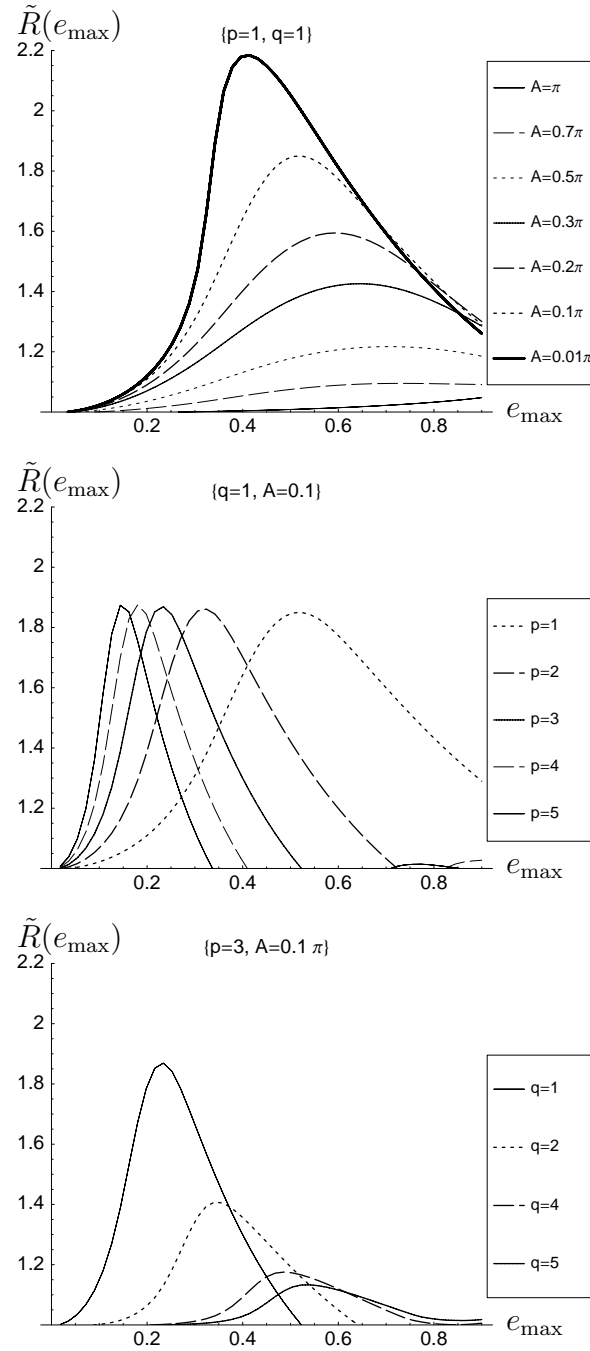
Figure 3.10: Dimensionless collisional rate $\tilde{R}(e_{\max})$ in the disc, Top: dependence on libration width A width for the 2:1 resonance. Middle: dependence on resonance parameter p for first-order resonances $q = 1$ with $A = 0.1\pi$. Bottom: dependence on the order of resonance q for $p = 3$ and $A = 0.1\pi$.
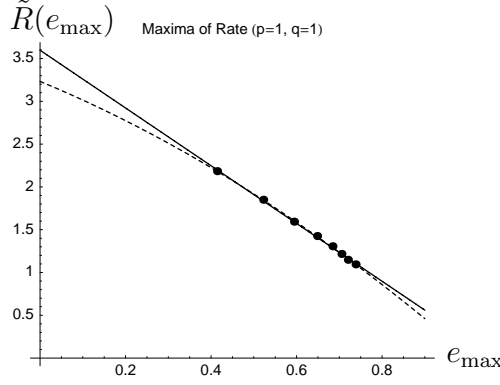
Figure 3.11: Plot of the heights of the maxima of $\tilde{R}(e_{max})|_{max}$ as a function of their positions for different A of the 2:1 resonance. Dots: data from calculations for different A, solid line: linear fit, dashed line: quadratic fit.

linearly with decreasing e_{max}. If we extrapolate this 'secondary data' to the maximum position $e_\star = 0.31$ for $A \to 0$, we get an estimate for the maximum collisional rate in the perfect resonance of

$$\lim_{A \to 0} \tilde{R}(e_{max})|_{max} \approx 2.5 R_0 \,,$$

for both linear and quadratic interpolation.

The collisional rates are intimately connected to collisional (life)times of the disc particles. The average collisional lifetime of an object in the disc defined as is

$$T_{coll}(e_{max}) = \left[\frac{\int_{e_1} \int_{e_2} R(e_1, e_2) \phi_e(e_2; e_{max}) \phi_e(e_1; e_{max}) de_2 de_1}{\int_{e_1} \int_{e_2} \phi_e(e_2; e_{max}) \phi_e(e_1; e_{max}) de_2 de_1} \right]^{-1} \tag{3.61}$$

or simply

$$T_{coll}(e_{max}) = \frac{1}{R(e_{max})}, \tag{3.62}$$

where $R(e_{max})$ is given by Eq. (3.59) with $N = n$.

Remember that we have calculated R in quasi-3D. More exactly: in the collisional rates, which are proportional to velocity / volume, we do take into account the inclinations when calculating the volume, but still ignore those in velocity.

3.8 Concerning High Eccentricities

In the previous sections we presented results for eccentricities e_1, e_2, e_{max} up to values of $e. = 0.9$. The total range of eccentricities for particles on elliptic orbits is $[0, 1]$ ($e > 1$ corresponds to hyperbolic, i.e. unbound, orbits). All our calculations performed in Sec. 3.5 are valid for the whole range of range minus its boundaries, i.e. for all eccentricities

$0 < e < 1$. We discussed the lower border in a separate section (3.5.6). We also aviod the upper limit in our calculations because there things diverge, too, this time for physical reasons. In the case $e = 1$ the orbit is a single, straight line of length $2a$ and both orbital velocity and acceleration diverge in the apo- and pericentre. It is not a physically stable orbit.

The deviations of the collisional rate $R(.)$ from R_0 in the nonresonant case are also due to effects of high eccentricity. The R_0 given in (3.58) *is* the nonresonant collisional rate – but only for small eccentricities. The deviations from $\tilde{R} = 1$ in Fig. 3.10 give an impression of the extent of the high-eccentricity corrections needed.

Taking a look at the dynamics of the resonance we find further constrains on e. The maximum possible eccentricity e_{res} which can be reached by resonant pumping (cf. Eq. (2.7)) is,

$$e_{\mathrm{res}} \equiv \lim_{t \to \infty} e(t) = \sqrt{\frac{q}{3p}} \, . \tag{3.63}$$

For the 2:1 resonance whose collisional velocities and rates are depicted in the upper panels of Figs. 3.7 and 3.10, this gives $e_{\mathrm{res}} = 0.58$. Even that maximum value is hardly reached. The particles start to become unstable already at the moment their orbits cross that of the planet, $a_{\mathrm{res}} (1 - e(t)) \leq a_p$ and will be ejected from the resonance soon after.

Since we are using the kinetic theory, setting the maximum eccentricity e_{max} 'by hand', instead of directly solving the equations of motion for the disc particles, we are not constrained by this dynamical limitations. We are able to check what would happen if a certain population acquires – by whatever means – a higher maximum eccentricity.

Because of this dynamical limitations we do not take great pains to make high-eccentricity corrections of our equations and simply avoid critically high eccentricities near $e = 1$.

3.9 The 1:1 Resonance: Trojans

The so called Trojan asteroids at the two trigonal Lagrangian points are a special case. First from the geometrical point of view and then from the observational one. Jupiter's Trojans are one of the very few cases in the Solar System where we can not only identify an asteroid to be resonant but also *see* the structures predicted by theory. Most other resonant groups are either too far away (Plutinos) or too scarcely populated (Earth belt) for the overall structure to be observable.

Trojans do reside in the 1:1 resonance, i.e. $p = 1$, $q = 0$. All the formulas derived and discussed above are valid in this case, but the results reveal important qualitative differences from the first- and higher-order resonances. Figure 3.12 presents the collisional velocity and the rates for Trojan clouds with different maximum eccentricities e_{max} and different libration amplitudes A.

Like in the case $q > 0$, V_{imp} vanishes when e_{max} goes to zero. However, unlike for other
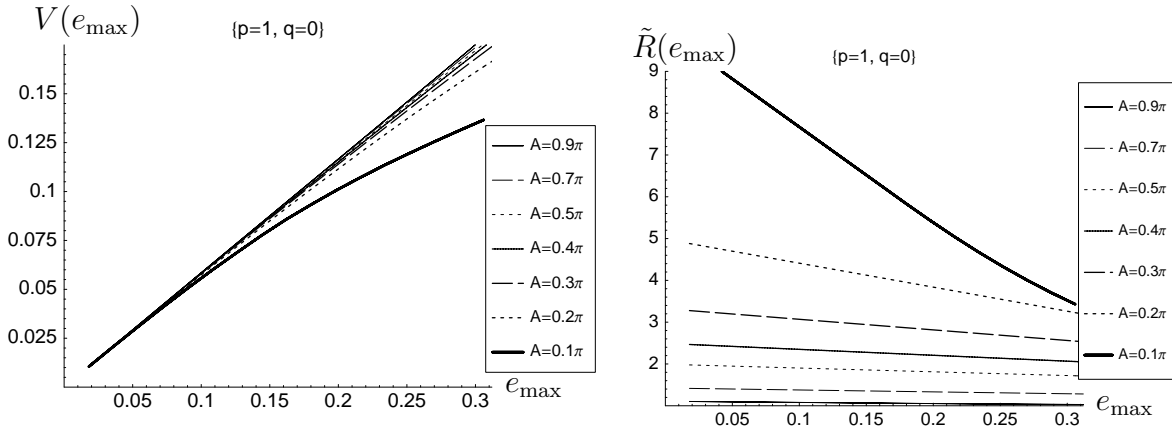
Figure 3.12: The case of Trojans. Left: collisional velocity $V_{\mathrm{imp}}(e_{\max})$ in units of V_{kepler}; cf. Fig. 3.7. Right: dimensionless collisional rate $\tilde{R}(e_{\max})$; cf. Fig. 3.10. Different curves correspond to different libration widths A.

resonances, $\tilde{R}(e_{\max})$ has a maximum at $e_{\max} = 0$. What is more, that maximum collisional rate goes to infinity when $A \to 0$. Mathematically, this is explained in Section 3.5.6; for instance, Eq. (3.51) is no longer valid – it was obtained under the condition $e_1, e_2 \neq e_\star$. Here $e_\star = 0$ is the only (non-complex) solution of (3.50). Geometrically, the explanation is obvious. For $q > 1$, even in the case where $e_{\max} = 0$ and $A = 0$ the objects form an (infinitesimally narrow) ring. For $q = 0$, the cloud simply shrinks to the Lagrangian point in that case – in other words, all the objects reside exactly at one and the same point and have zero relative velocities. Their volume density is infinitesimally high, and so is the collisional rate. For small non-zero $e_{\max}$ and A, frequent collisions are expected. In contrast to this, the velocity would be lower, but the effect here is almost negligible, because the velocities would be dominated by 3D-terms coming from inclinations, which we do not consider in our model.

3.10 Comparison to Other Work

3.10.1 Approach by Dell'Oro et al.

The formalism developed here is based on exactly the same ideas as those of the one developed by by Dell'Oro and collaborators (Dell'Oro & Paolicchi, 1998; Dell'Oro et al., 1998). For instance, our $\Delta^{(1)}$-integral (3.27) is essentially the same as Eq. (9) or (10) in Dell'Oro & Paolicchi (1998). A technical difference between the two approaches is that we incorporate the collisional condition directly into the integrand, through the function $\delta(\mathbf{r}_1 - \mathbf{r}_2)$, and assume a particular functional form of the distribution of orbital elements (Eqs. 3.12 and 3.13). We then perform analytically as many integrations in the multiple integral as possible. As a result, only one integration (see Eq. 3.42) needs to be performed
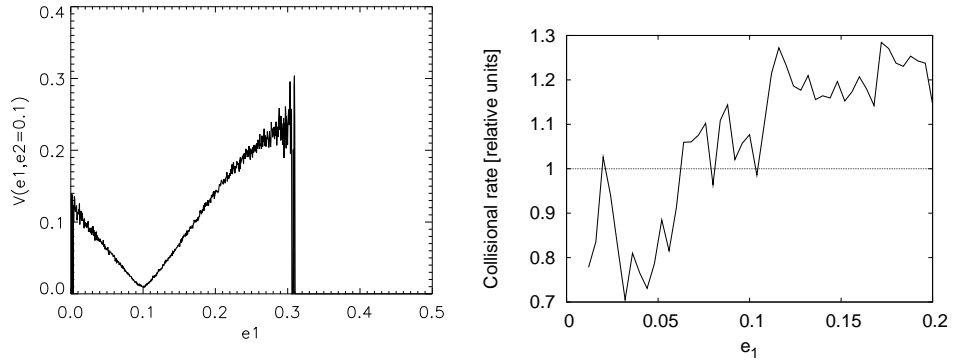
Figure 3.13: Typical numerical results for collisional velocity $V_{\mathrm{imp}}(e_1, e_2 = 0.1)$ (left) and collisional rate $R(e_1, e_2 = 0.1)$ (right) in a 2:1 resonance for comparison with left column of 3.5 3.8. See also right columns of Figs 4 and 7 of Queck et al. (2007).

numerically. The price to pay for "more analytics" in our approach is that it is much "heavier" mathematically, which makes a strict 3D-treatment impossible. Still, we deem this approach suitable for theoretical study of a statistical ensemble of pseudo-objects with continuous distributions of orbital elements. As we have seen, our approach is quite convenient for exploring the dependence of the collisional velocities and rates on various parameters ($e_{\max}$, A, p, and q). Moreover, our approach naturally circumvents numerical difficulties that otherwise would arise for extreme values of these parameters (e.g., for very low or very high eccentricities).

In contrast, Dell'Oro and his group evaluate the multiple numerically using a Monte-Carlo technique integrals, similar to our $\Delta^{(k)}$. This allows a study in three dimensions. In fact, in terms of our formalism they use

$$\mathbf{p} = (a, e, i) \qquad \mathbf{q} = (\Omega, \omega, \theta) \tag{3.64}$$

(cf. Eq. 3.25). This makes their approach ideal for the study of particular collisional complexes in the Solar System, consisting of individual objects with known orbital elements. Their method is particularly useful for exploring effects associated with inclinations and longitudes of nodes.

3.10.2 Numerical Formalism by Thébault and Collaborators

We also compare our results to those of some numerical calculations. The latter were obtained by Phillipe Thébault using his algorithm developed in Thébault & Brahic (1998) and Thébault & Doressoundiram (2003). This algorithm is a N-body code with "inflared particle radius", i.e. they consider a relatively small number of particles N_{num} with radius s_{num}, such that their product equals that of the real particles,

$$N_{\mathrm{num}} s_{\mathrm{num}} = N_{\mathrm{real}} s_{\mathrm{real}}.$$

They follow the motion and collisions of this enflared particles. Fig. 3.13 shows some test numerical integrations, in which planetesimals were trapped into a 2:1-resonance with a slowly migrating, Neptune-like planet.

With respect to the velocity we see exactly the same V-shape pattern in the left panel of Fig. 3.13 as was seen in Fig. 3.5: a drop to 0 at $e_1 = e_2$ and rise to $\sim 0.25 V_{\mathrm{kepler}}$ at $e_1 = 0.3$. At that point the calculation ceases because the particle is ejected from the resonance.

With respect to the rates there is a lot of numerical noise caused by a limited number of integrated particles. Those notwithstanding, the right panel of Fig. 3.13 shows the same tendency of a small, but definite, increase for larger e_1 as Fig. 3.8 showed.

3.10.3   "Intrinsic Collisional Probability"

The "intrinsic collisional probability" is a phrase coined by Marzari and collaborators. It describes the collisions within a certain population and gives the probability that a particle has a collision with any other per unit time, i.e. the intrinsic collisional probability is the frequency of collisions, or in other words the collisional rate.

Marzari et al. (1996) studied Jupiter's Trojans and found that their intrinsic collisional probability is about twice a high as that of the Main Asteroid Belt between Mars and Jupiter.

Our result, see Fig. 3.12, is that for the Trojans the resonant collision rate is up to 10 times that of the nonresonant one, depending on A and e_{max}. To compare this to Marzari's result we have to consider the inclination and semimajor axis dependence of R first. Eq. (3.58) gives $R \sim a^{-7/2}$ and $R \sim 1/h \sim \sin \epsilon^{-1}$, for flat discs, $i \ll \pi$, we can approximate the sine of the opening angle with the mean inclination $< i >$: $\sin \epsilon \approx < i >$. Thus we have $R \sim a^{-7/2} \langle i \rangle^{-1}$. The Trojans have Jupiter's semimajor axis, $a = 5.2 \, AU$, whereas the Main Belt is situated between $2.2 \, AU$ and $3.2 \, AU$, in the mean about half the Trojans' distance to the Sun. For the inclinations the situation is similar: Trojans have $< i > = 15°$, the Main Belt $< i > = 8°$. Thus asteroids in the Main Belt should have a collisional rate 20 times higher than the Trojans due to geometrical reasons. However, the Trojans are resonant, the Main Belt asteroids are not, so there is an additional factor of ten in favour of the Trojans, so that in the end both collisional rates are of comparable value. Considering all the simplifications we made, e.g. quasi-3D calculations, Heaviside distributions of orbital elements, fully circular planet, this is in reasonable agreement with the result by Marzari et al. (1996).

Unlike the collision rate, the effect of the resonance on the collisional velocity is minor. In fact, given rather large inclinations of Trojans, V_{imp} will be dominated by inclination terms of the order iV_{kepler} that are ignored in our treatment. As a result, we expect nearly the same impact velocities for Trojans as for the main-belt asteroids, and, as a consequence, the same collisional outcomes. This fully agrees with conclusions of Marzari et al. (1996) and Dell'Oro et al. (1998) as well.

3.11 Summary

In this chapter we have developed a statistical model of the celestial mechanics in a circumstellar debris disc. Therein we successfully combined collisions with resonant dynamics. Thus we were able to explore the collisional velocity and rate for subsets of disc particles on the one hand and for the whole disc on the other hand. Due to the kinetic approach we were able to choose freely the resonant parameters p and q, the libration width A and maximum eccentricity $e_{\max}$.

We averaged both velocity and rate over the whole particle orbit being well aware that in resonant ensembles the particle density is much higher in the resonant "clumps" so that most collisions take place there (see, e.g., Fig. 4 in Wyatt, 2006). The influence of the resonance on the particle ensemble is strongest in the "clumps". The individual particles, however, move in and out of them in their revolution around the star.

The collisional velocity for subsets of disc particles, $V_{\mathrm{imp}}(e_1, e_2)$, we found to be smallest for $e_1 = e_2$. It is almost linear for small eccentricities $e_1, e_2 \lesssim 0.3$ but becomes highly nonlinear for large ones $e_1, e_2 \gtrsim 0.7$. Averaged over both eccentricities and thus representing the collisional velocity of the whole ensemble $V_{\mathrm{imp}}(e_{\max})$ is almost linear over the whole range of eccentricities considered. The most remarkable feature is that for small eccentricities the resonance lowers the collisional velocity, in contradiction to heuristic arguments. This might be due to geometrical aligning in resonance. In all cases considered V_{imp} was of the order of magnitude $\sim e.v_{\mathrm{kepler}}$.

Concerning the collisional rate there is a definite change from nonresonant to strongly resonant ones. While the rate $R(e_1, e_2)$ of two subsets is almost constant in the nonresonant case, – some high eccentricity corrections not withstanding – it develops a pronounced maximum on the line of equal eccentricities for stronger resonances. The smaller the libration width A, the more pronounced the maximum becomes,

$$A = 0.3\pi \quad \Rightarrow \quad \text{maximum rate } 1.89R_0$$
$$A = 0.1\pi \quad \Rightarrow \quad \text{maximum rate } 3.75R_0$$
$$p = 3 \text{ in both cases.}$$

For the rate $R(e_1, e_2)$ a higher resonance parameter p not only moved the maximum towards lower eccentricities, but also results in slightly higher maximum values:

$$p = 1 \quad \Rightarrow \quad \text{maximum rate } 3.67R_0 \text{ at } e_1 = e_2 = 0.38$$
$$p = 3 \quad \Rightarrow \quad \text{maximum rate } 3.75R_0 \text{ at } e_1 = e_2 = 0.17$$
$$A = 0.1\pi \text{ in both cases.}$$

The collision rate of the whole disc $R(e_{\max})$, i.e. $R(e_1, e_2)$ averaged over both e_1 and e_2, still shows such a maximum, becoming steeper for smaller libration width. It is somewhat lower than in the unaveraged case: for $A = 0.1$ and $p = q = 1$ it is only $1.85R_0$ now. The parameter p still shifts the maximum inwards, but does not alter the height anymore. For

higher orders q of the resonance the maximum is shifted towards higher e_{max} and lowered considerably in height,

$$q = 1 \quad \Rightarrow \quad \text{maximum } 1.87R_0 \text{ at } e_{\text{max}} = 0.23$$
$$q = 5 \quad \Rightarrow \quad \text{maximum } 1.13R_0 \text{ at } e_{\text{max}} = 0.54$$
$$p = 3 \text{ in both cases}$$

The most drastic influence of resonance is seen in the case of Trojans ($p = 1, q = 0$). The collisional velocity is only subtly influenced again, but the rate actually goes to infinity for $e_{\text{max}} \to 0$.

Although we did need quite a few simplifying assumptions in order to be able to carry out analytic calculations our results are in good agreement with others' work. In contrast to those, our results show the influence of the different parameters in an easy and straightforward way.

Chapter 4

Origin of Resonant Structures

In the previous chapter we explored the collisional behaviour within resonant ensembles. But how does a resonance actually create structures in circumstellar discs? This is the question we will address in this part of our work, whereas before we just assumed the circumstellar particles to *be* in a resonant, structured ensemble.

The somewhat 'classical' mechanism of structure formation by resonances is based upon transport processes in the circumstellar disc. It assumes that there is a reservoir of dust grains far out, due to Poynting-Robertson and stellar wind drag – its significance will be tested also – the disc particles are moving inwards. When they near the location, $a \approx a_{\rm res}$ of an mean motion resonance, they get trapped and form the observed structures, see e.g. Figs. 2.2, 2.6 and 2.7. This scenario was first proposed by Gold (1975) and thoroughly discussed, especially since several discs have been spatially resolved (e.g. Weidenschilling & Jackson, 1993; Beaugé & Ferraz-Mello, 1994; Liou & Zook, 1997; Wyatt, 2005). We will refer to it as 'scenario I'.

But this mechanism has one major problem: the timescales. As Lecavelier des Etangs et al. (1996); Lagrange et al. (2000) and Wyatt (2005) have shown PR drag is a rather slow process. Collisions in such gas-less debris discs are very violent, mostly destructive – and may be faster than transport by PR-drag. They might smear out or totally destroy the resonant structures faster than PR drag replenishes them. Therefore another, not time dependent formation scenario was suggested (Wyatt, 2003, 2006), hereinafter 'scenario II'. Now the dust's parent bodies, the planetesimals, are caught in resonance, because they grew there or were caught during earlier planet migration phases. The capture mechanism for the planetesimals will not be a subject of our investigation. Their existence is proved by two examples from the Solar System, Jupiter's Greeks and Trojans (L_4 and L_5 branch of 1:1 resonance) on the one hand and Neptune's Plutinos (3:2 resonance) on the other one. Those resonant planetesimals collide amongst each other and create a cloud of fragments, including the observable dust.

We will make a comparative analysis of both scenarios with analytic models as simply as possible. We want to avoid extensive numerical solutions of any equation and instead obtain results which show the influence of certain parameters in an obvious and

straightforward way.

Scenarios I and II are considered in Secs 1 and 2, respectively.

4.1   Scenario I

4.1.1   Effects

We start with an analysis of scenario I, in which dust particles are brought from afar to resonant locations and are captured in resonances. We have to consider three types of effects here: first the drag forces, second the resonance and third the collisions. The transport is driven by the outflow of the star, photons as well as massive particles like electrons, protons, α particles and so on. The photons move radially outward, but with a finite velocity c, the wind particles move with the much smaller velocity v_{wind} and in spiral formation due to the rotation of the star. Thus a dust particle moving tangentially around the star is hit aslant by photons and wind and *dec*elerated by the acquired momentum. In case of photons the effect is called *Poynting-Robertson effect*, in case of massive particles *stellar wind*. For our models only the velocity dependent, indirect parts of them will be of interest.

The decelerating force grows with the intensity I irradiated upon the particle as well as with the latter's orbital velocity $\mathbf{v}$ and cross-sectional area $\mathfrak{A}$ (Burns et al., 1979),

$$\mathbf{F}_{\text{rad}} = -\frac{I_{\text{rad}}\mathfrak{A}}{c}\frac{\mathbf{v}}{c} . \tag{4.1}$$

c being the speed of light. We make a Taylor expansion of $I_{\text{rad}} = I_0^{\text{rad}}\sqrt{1 - v^2/c^2}$ and neglect all terms v^2/c^2 since $v \ll c$. We consider the radial vector component of that, called Poynting-Robertson effect, and obtain

$$F_{\text{PR}} = -\frac{I_0^{\text{rad}}\mathfrak{A}}{c} . \tag{4.2}$$

Inserting $I_0^{\text{rad}} = L_*/(\pi r^2)$ and $\mathfrak{A} = \pi/4\,s^2$ this can be rewritten as

$$F_{\text{PR}} \quad = \quad -\frac{1}{4}\frac{L_*}{c}\frac{s^2}{r^2}. \tag{4.3}$$

Making use of the $1/r^2$ dependence we are able to bring this into the same formal structure as the gravitational force,

$$F_{\text{PR}} \quad \equiv \quad -\beta_{\text{rad}}\frac{GM_*m}{r^2} \tag{4.4}$$

$$\text{with } \beta_{\text{rad}} \quad := \quad \frac{3}{16\pi}\frac{L_*}{GM_*c\rho s} , \tag{4.5}$$

where s is the dust grain's radius, ρ its density, m its mass. M_* is the stellar mass and L_* the luminosity.

In case of the massive particles the work-flow is similar, but now the intensity I_{wind} has to be scaled by the wind velocity v_{wind} instead of the speed of light. (To be exact, the wind velocity is vectorial, too, $\mathbf{v}_{\mathrm{wind}}$, but we are interested in the radial component only.) The wind's force is

$$\mathbf{F}_{\mathrm{wind}} \quad = \quad -\frac{I_{\mathrm{wind}}\mathfrak{A}}{v_{\mathrm{wind}}}\frac{\mathbf{v}}{v_{\mathrm{wind}}} \tag{4.6}$$

$$F_{\mathrm{wind}} \quad = \quad -\frac{I_0^{\mathrm{wind}}\mathfrak{A}}{v_{\mathrm{wind}}} \tag{4.7}$$

$$F_{\mathrm{wind}} \quad = \quad -\frac{3}{16\pi}\frac{\dot{M}_* \, v_{\mathrm{wind}} \, s^2}{r^2} \tag{4.8}$$

$$\equiv \quad -\beta_{\mathrm{wind}}\frac{GM_*m}{r^2} \tag{4.9}$$

$$\text{with} \quad \beta_{\mathrm{wind}} \quad := \quad \frac{3}{16\pi}\frac{v_{\mathrm{wind}}^2}{GM_*\rho}\frac{1}{s}\dot{M}_* \,. \tag{4.10}$$

Here $\dot{M}_*$ is the mass-loss rate of the star, the massive particles' equivalent to the photons' luminosity.

As can be seen, the Poynting-Robertson and stellar wind forces have the same radial dependence. Therefore we combine them into one drag force, F_{drag}. Therein we have to remember the different angles due to different velocities under which both are acting upon the orbiting dust particle. This angle is given by the ratio of the velocities, thus

$$\beta \quad = \quad \beta_{\mathrm{rad}} + \beta_{\mathrm{wind}}\frac{c}{v_{\mathrm{wind}}} \tag{4.11}$$

$$\beta \quad = \quad \frac{3}{16\pi}\frac{L_*}{GM_*c\rho s}\left(1 + \frac{\dot{M}_*c^2}{L_*}\right). \tag{4.12}$$

With this formalism, it is evident that the drag force reduces the gravity to an 'effective gravity',

$$F_G^{\mathrm{eff}} = (1 - \beta)F_G \,, \tag{4.13}$$

and that the drag is the more efficient the smaller the dust particles. This seems to contradict the fact that both Poynting-Robertson and stellar wind forces are $\sim \mathfrak{A} \sim s^2$. But in the circumstellar environment, gravity is always at work, too, and $F_G \sim m \sim s^3$. Thus the larger the grains are, the more dominating gravity will be.

For later use we rewrite (4.12) in a more convenient form:

$$\begin{aligned}\beta \quad = \quad & 0.57\left(\frac{L_*}{L_\odot}\right)\left(\frac{M_\odot}{M_*}\right)\left(\frac{1\,\mathrm{g\,cm}^{-3}}{\rho}\right)\left(\frac{1\,\mu\mathrm{m}}{s}\right) \\ & \times\left(1 + 0.29\left(\frac{\dot{M}_*}{\dot{M}_\odot}\right)\left(\frac{L_\odot}{L_*}\right)\right).\end{aligned} \tag{4.14}$$

In what follows, we treat M_* as a parameter and calculate luminosity by using the standard $L_* \propto M_*^{3.8}$ relation for main-sequence stars.

The typical resonant dynamics have been summarized in the introduction: once captured, the particle's semimajor axis stays constant, its inclination is reduced and the eccentricity pumped up. At a certain e_{max} the particle becomes unstable and is ejected from the resonance. Most likely it will leave the planetary system. But some of them may continue migrating toward the star. Such cases were considered by Marzari & Vanzani (1994). Then the dynamics are even more complicated due to chaotic regions in the vicinity of the resonances. And the resonance inducing planet needs to be a very low mass one ($M \sim M_\oplus$), which is still below the observational limits today. It might become observable with the DARWIN or TPF mission, but even for them it is not very likely. We confine our analysis to larger, at least Neptune/Uranus-mass planets.

Since we are now dealing with the small dust grains for which the PR and wind drag needs to be considered we have to correct (2.6) accordingly,

$$a_{res} \quad = \quad (1 - \beta)^{1/3} \left(\frac{p + q}{p} \right)^{2/3} a_p \, , \qquad (4.15)$$

where β is the combined one of (4.12). The same goes for $e(t)$, Eq. (2.7).

The third and last effect is that of the collisions. They were thoroughly investigated in the previous chapter. We will use the most simple collisional model. We consider ensembles of single sized particles and collisions among them are totally destructive. However, we are aware that in collisional equilibrium there is a certain distribution of particle sizes (Dohnanyi, 1969) and that grains are mostly destroyed by those just smaller than themselves (Krivov et al., 2006). The collisions are destructive in the sense that afterward they no longer reside in the resonant ensemble, either because they are really broken up or because they have been scattered out of the resonance to join the background. We will not consider the collisional outcome here. After a collision the particle simply is not a member of the considered ensembles anymore.

4.1.2   The Set-up

The set-up within which we will construct our model is depicted in Fig. 4.1. It consists of one planet on a circular orbit with semimajor axis a_p and an annulus around a given external, mean motion resonance, $a_{res}(1 - e_{max}) < a < a_{res}(1 + e_{max})$. Two populations of dust grains reside in that annulus. The first is the non-resonant one of the background grains. Their distribution is rotationally symmetric, without internal structure and on mostly circular orbits due to PR drag (Wyatt & Whipple, 1950; Deller & Maddison, 2005).

Second are the resonant grains. Their distribution is asymmetric, they form 'clumpy' structures. We will mark all quantities of the background with subscript "0", the resonant population will have none. We will also omit unnecessary subscripts for quantities which are by model construction equal for both, such as size s and β ratio.

The half width e_{max} of the annulus is the maximum eccentricity that the resonant grains can aquire. At the most this is the eccentricity at which they are ejected from the
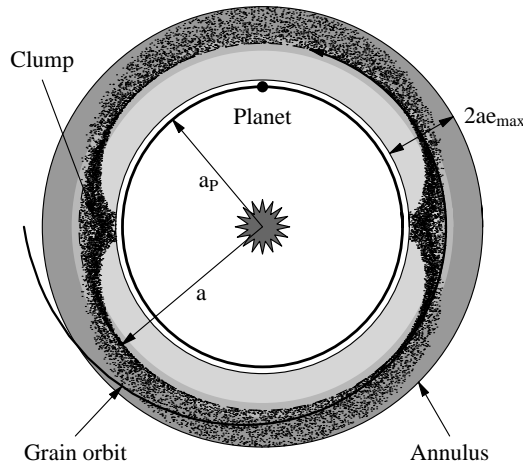
Figure 4.1: Schematic of the resonant and non-resonant components of the dust disc in the vicinity of a given resonance. The particular resonant population with two clumps shown here corresponds to the 3:2-MMR with $e_{\max} = 0.2$ and $A = 20°$.

resonance, e_{res}. But collisions might destroy them before reaching that value, therefore $e_{\max} \leq e_{\mathrm{res}}$. Under the influence of PR and wind drag Eq. (2.7) is valid as an approximation for small eccentricities only, a more general but also more complicated $e(t)$ can be found in Liou & Zook (1997). Eq. (3.63) gives a simple estimate of e_{res}, numerical integrations of which yield values between 0.1 and 0.4 (e.g. Weidenschilling & Jackson, 1993; Beaugé & Ferraz-Mello, 1994; Liou & Zook, 1997). We will adopt as a standard value $e_{\mathrm{res}} = 0.2$ throughout our calculations.

Each ensemble will consist of one typical grain size s corresponding to a certain β. The β ratio will be a free parameter in our model. It has to be chosen carefully to be large enough for efficient PR drag and small enough to get caught in resonance for a long time, compare e.g. Krivov et al. (2000); Thébault et al. (2003); Krivov et al. (2006) and Diploma thesis of M. Reidemeister. We will adopt $\beta = 0.1$ as a default.

The density ρ of the grains depends on the chemical composition, porosity and other parametres. We adopt an intermediate value of $2\,\mathrm{g\,cm}^{-3}$ throughout our work.

Farther out beyond the annulus there is the reservoir of dust grains, such that they are constantly replenished. That reservoir will not be the subject of our modelling. Once produced the dust grains drift inwards to the star by PR and wind drag at such a rate that $\dot{n}^+$ cross $a = a_{\mathrm{res}}$ per unit time.

When the grains arrive in the vicinity of a_{res} they are captured into resonance with a certain probability p_{res}. That capture probability depends on a wide range of parameters, e.g. the planetary mass and semimajor axis, the grains' size, inclination and eccentricity or the resonance parameters p, q themselves. E.g. Deller & Maddison (2005) found that

parameter	β	ρ	p_{res}	e_{res}
value	0.1	$2.0\ g/cm^3$	0.5	0.2

Table 4.1: Collection of default values for Scenario I.

for a Jupiter sized planet, capture into 5:2 resonance is most efficient, whereas for $0.05 M_J$ a wide range of them is more or less equally populated. A large β ratio, however, results in the capture preferentially into resonances close to the planet, $(p+q)/p \approx 1$, for smaller β capture is already very efficient at the outer ones 2:1, 3:2 or 4:3 (Liou et al., 1999; Reidemeister, 2007). A thorough investigation of the parameter space of resonant capture was recently performed in the Diploma thesis of Martin Reidemeister (Reidemeister, 2007). There and in the papers cited above p_{res} shows a large variation from 10% to almost 100%. We choose an intermediate value of $p_{\mathrm{res}} = 0.5$ in our calculations.

4.1.3   Kinetic Model and Timescales

We now construct a model, which shall contain all the effects discussed above on the one hand, but on the other hand it shall be as simple as possible, so that the influence of different parameters can be shown easily. We need the correct temporal scaling, meaning all the timescales have to be combined consistently to see where PR drag is fast enough to allow the development of structures and where it is not. A kinetic model fulfils all our requirements. This first needs the balance equation, now a much simpler form of (3.4). We combine the gains by drag forces, $\dot{n}^+$, and resonant capture, p_{res}, with the losses by collision, $T_{\mathrm{coll}}, T_{\mathrm{coll}}^0$, or ejection, T_{res}, to

$$\frac{dn}{dt} = \dot{n}^+ p_{\mathrm{res}} - \frac{n}{T_{\mathrm{res}}} - \frac{n}{T_{\mathrm{coll}}^0} - \frac{n}{T_{\mathrm{coll}}}. \tag{4.16}$$

T_{coll} and T_{coll}^0 are the collisional lifetimes for collisions *among* the resonant particles and for collisions of resonant particles with those from the *background*, respectively.

This means there are 4 typical timescales in our system, the two collisional ones T_{coll}, T_{coll}^0, the time of residence in the resonance T_{res} and the time to drift through the annulus T_{drag} by PR and wind drag. According to Burns et al. (1979) the drag timescale is

$$T_{\mathrm{drag}} = \frac{4 e_{\mathrm{max}}}{B}, \tag{4.17}$$

where B is $\sim \beta$ (cf. Eq. (2.8)), the sum of PR and wind drag.

This timescale can be linked to the number density of particles in the respective area. Multiplying the drift rate with the drift time gives the number of background particles in the annulus at a certain moment,

$$n_0 = \dot{n}^+ T_{\mathrm{drag}} .$$

During the drift the background ensemble is reduced in number due to resonant capture. To avoid unnecessary complications, it is assumed here, that the resonant capture occurs precisely at $a \equiv a_{\mathrm{res}}$. Therefore we split it in (I) drift from the outer rim of the annulus $a = a_{\mathrm{res}}(1+e_{\max})$ to the centre $a = a_{\mathrm{res}}$, where resonant capture actually happens, and (II) drift from the centre to the inner rim $a = a_{\mathrm{res}}(1 - e_{\max})$. So we get

$$n_0^I = \dot{n}^+ \hat{T}_{\mathrm{drag}} \tag{4.18}$$

$$n_0^{II} = (1 - p_{\mathrm{res}})\dot{n}^+ \hat{T}_{\mathrm{drag}} \tag{4.19}$$

$$n_0 = n_0^I + n_0^{II} \tag{4.20}$$

$$= (1 - \frac{p_{\mathrm{res}}}{2})\dot{n}^+ T_{\mathrm{drag}} \tag{4.21}$$

$$\mathrm{with}\ T_{\mathrm{drag}} = 2\,\hat{T}_{\mathrm{drag}}\ . \tag{4.22}$$

The number density in return is linked to the geometrical optical depth τ_0,

$$\tau_0 = \frac{n_0\,\sigma}{S_0}\ , \tag{4.23}$$

where σ is the collisional cross section of a single particle, $\sigma = \pi s^2$ and S_0 the size of the annulus, $S_0 = 4\pi a^2 e_{\max}$. Combining (4.23), (4.21) and (4.17) we are now able to express the drift rate by an observable quantity. The explicit expression is

$$\dot{n}^+ = \frac{a^2 B}{s^2 \left(1 - \frac{p_{\mathrm{res}}}{2}\right)}\,\tau_0\ . \tag{4.24}$$

So we will be able to compare our model with real, observed systems.

Considering the collisional timescales we confer to the previous chapter, where collisions within resonances were investigated thoroughly. There we found that in a certain, resonant ensemble the collisional rate, being the inverse of the collisional timescale, is about twice as high within resonance as out of it, see Fig. 3.10. Thus, if R and T_{coll} are the collisional rate and time scale within the resonant ensemble and R_0 and T_{coll}^0 those with the nonresonant background particles, we have

$$R \equiv \frac{1}{T_{\mathrm{coll}}} = 2R_0$$

$$\Rightarrow T_{\mathrm{coll}} = \frac{1}{2}T_{\mathrm{coll}}^0\ . \tag{4.25}$$

If the number density n is known, the collisional rate can be calculated by

$$R = \frac{n\sigma v}{V}\ , \tag{4.26}$$

where σ is again the collisional cross section, v the collisional velocity and V the interaction volume. With the respective variables, the same is true for the background. In the case of a nonresonant ensemble the Appendix of Krivov et al. (2006) gives

$$V_0 = (2\pi a)^2\,h|\sin\Gamma| \tag{4.27}$$

$$v_0 = v_{\mathrm{kepler}}|\sin\Gamma|, \tag{4.28}$$

with $h = 2a\sin\epsilon$ being the height of the disc (ϵ the disc's semi-opening angle) and Γ the angle between the two colliders. Eq. (4.28) is true for very flat discs only, it ignores corrections due to nonzero inclinations as well as those due to eccentricities. It can be understood as a mean value, averaged over the orbit. The Keplerian velocity v_{kepler} needs to be PR drag corrected,

$$v_{\text{kepler}} = (GM_*(1 - \beta_{\text{PR}})/a)^{1/2} \,. \tag{4.29}$$

Note that here we have the Poynting Robertson drag only, the wind drag moves the particle to a different orbit a, but does not affect the orbital velocity. Collecting everything the collisional time for the background is

$$T_{\text{coll}}^0 = \frac{1}{n_0} \frac{(2\pi a)^2 h}{\sigma v_{\text{kepler}}} \tag{4.30}$$

The calculation of V and v in the resonant, non-rotationally symmetric case is not as easy, as was seen in the previous chapter. But making use of (4.25) we can evade the extensive analysis and have the respective resonant collisional time analogous to (4.30) as

$$T_{\text{coll}} = \frac{1}{2}\frac{1}{n}\frac{(2\pi a)^2 h}{\sigma v_{\text{kepler}}} \,. \tag{4.31}$$

For simplification of later calculations we define

$$\hat{T}_{\text{coll}} := \frac{(2\pi a)^2 h}{\sigma v_{\text{kepler}}} \tag{4.32}$$

and finally have

$$T_{\text{coll}} = \frac{1}{2}\frac{1}{n}\hat{T}_{\text{coll}} \tag{4.33}$$

$$T_{\text{coll}}^0 = \frac{1}{n_0}\hat{T}_{\text{coll}} \,. \tag{4.34}$$

Last, but not least, we need the resonant timescale T_{res}. This is that time which is needed to pump the eccentricity of a resonant particle from zero to e_{res}. At $e = e_{\text{res}}$ the particle is ejected from the resonance due to dynamic perturbation. We start by inverting (2.7), because now we no longer follow the time evolution of a particle but want to know the time it takes to achieve a certain eccentricity. Inversion plus Taylor series expansion in e gives

$$t = \frac{p+q}{3p}\frac{1}{B}\ln\left(\frac{3p}{q}e^2 + \frac{9p^2}{2q^2}e^4 + \mathcal{O}(e^6)\right) \,. \tag{4.35}$$

Table 4.2 shows some example values of the 2nd and 4th order terms for different resonances and different e_{res}. As can be expected from the p^2 dependence, the 4th order is negligible for small p, but must be considered for larger ones. For large q it can be neglected in

2:1 resonance:	e_{res}	0.1	0.3	0.5	0.7
	1st term	0.03	0.27	0.75	1.47
	2nd term	0.0004	0.0364	0.2812	1.080
9:8 resonance:	e_{res}	0.1	0.3	0.5	0.7
	1st term	0.24	2.16	6.00	11.76
	2nd term	0.029	2.33	18.0	69.15
9:1 resonance:	e_{res}	0.1	0.3	0.5	0.7
	1st term	0.0037	0.0337	0.0937	0.1837
	2nd term	0.0000	0.0006	0.0044	0.0169

Table 4.2: Comparison of the 2nd and 4th order term in the Taylor series of $t(e)$, see Eq. (4.35), for three resonances, $p = q = 1$ (top), $p = 8, q = 1$ (middle) and $p = 1, q = 8$ (bottom).

any case. We will restrict ourselves to low order resonances and small e_{res} and thus omit terms of the order of e^4. The resonant time then is

$$t(e_{\text{res}}) \equiv T_{\text{res}} \approx \frac{p + q}{q} \frac{e_{\text{res}}^2}{B}. \tag{4.36}$$

Thus we have now allocated all relevant timescales for the resonant particles. In Figs 4.2 and 4.3 we compare all four of them as functions of the optical depth of the background and various parametric dependencies. Generally we see that of course T_{res} is independent of τ_0, and T_{drag} almost is. Only for very large optical depth does it decrease slightly. Regardless of the circumstances (given by τ_0, s or $\dot{M}_*$), collisions with the background are always faster than those within the resonant ensemble. In dilute discs with very low optical depth, resonant and drag timescales are shorter than the collisional one T_{coll}^0. For very large τ_0 the opposite is true and, because we set p_{res} to 0.5, T_{coll} approaches T_{drag}. All timescales are shorter the smaller the grains are, although the collisional ones are almost independent of grain size.

Fig. 4.2 shows a solar mass star for two different mass-loss rates: the solar (top) and a 10 times larger one (middle). All timescales are affected, they all are shorter for larger $\dot{M}_*$, but T_{drag} and T_{res} more so than T_{coll} and T_{coll}^0. The background collisions for $s = 2.9\mu m$ have the shortest of all timescales up to $\tau_0 \approx 1 \cdot 10^{-5}$ in the case $\dot{M}_* = \dot{M}_\odot$. In the case $\dot{M}_* = 10\dot{M}_\odot$, however, that border is shifted to $\tau_0 \approx 5 \cdot 10^{-5}$. For small particles, $s = 0.7\mu m$, both borders lie at a about 1 order of magnitude larger τ_0. The lowest panel of Fig. 4.2 shows the timescales for one particle size, $s = 1.5\mu m$, but two capture probabilities: a very low one of 20% and a very high one of 80%. Now also the collisional times are quite thoroughly affected whereas in the two upper panels they showed only subtle dependence on any parameters. T_{coll} drops to 1/3 for $p_{\text{res}} = 0.8$ compared to $p_{\text{res}} = 0.2$, although now there are residing 4 times more particles in the resonance. T_{coll}^0
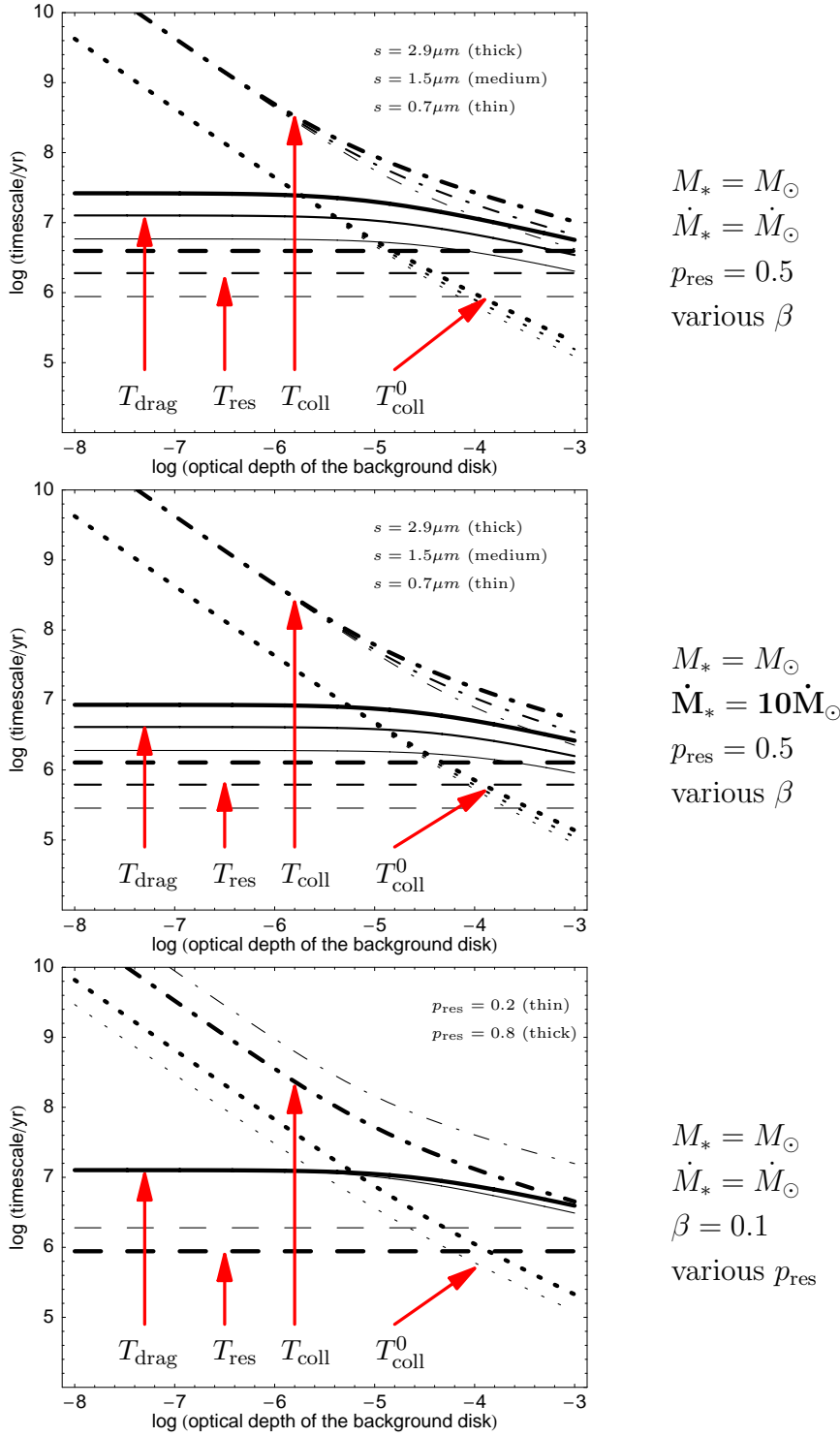
Figure 4.2: Typical timescales for a Sun-like star as functions of the normal optical depth τ_0 of the non-resonant disc. Thick, medium, and thin lines: $\beta = 0.05$, 0.10, and 0.20, respectively. These values correspond to $s = 2.9$, 1.5, and $0.7\,\mu$m. Top: The Sun, with its actual mass-loss rate $2 \cdot 10^{-14} M_\odot/year$. Middle: with a 10 times larger one. Bottom: dependence on capture probability for Sun ($M = M_\odot$, $\dot{M} = \dot{M}_\odot$) for a single size.
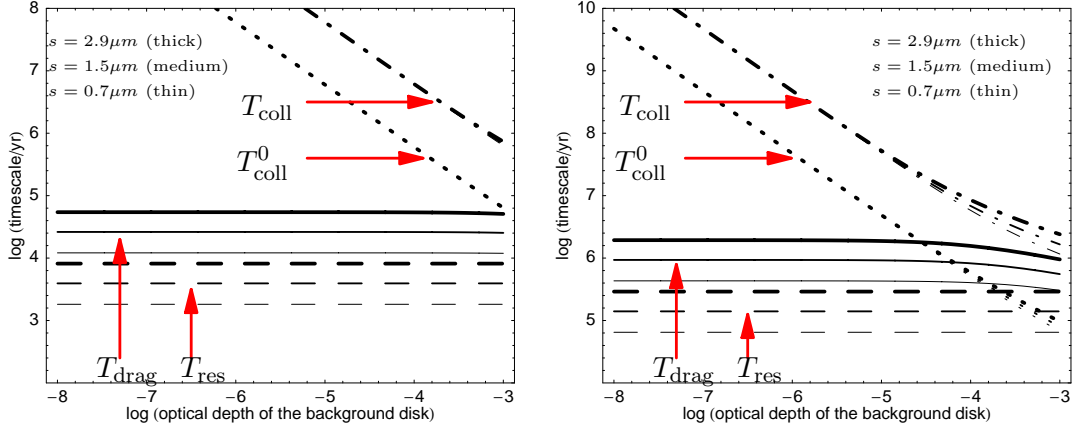
Figure 4.3: Typical timescales as functions of the normal optical depth τ_0 of the non-resonant disc. Same as Fig. 4.2, but for two example stars known to host a debris disc. Left: AU Mic with $M = 0.6 M_\odot$, $\dot{M} = 300 \dot{M}_\odot$ Right: ϵ Eri with $M = 0.8 M_\odot$, $\dot{M} = 30 \dot{M}_\odot$

only becomes twice as large, when p_{res} rises from 0.2 to 0.8. Considering the uncertainties in the determination of τ_0 for any observed disc we can neglect the p_{res} dependence in our analysis of the timescales.

The optical depth of the Kuiper Belt in the Solar System is estimated to be $\tau_0 \approx 10^{-6}$. For a medium sized particle, $s = 1.5 \mu m$, the drag time is about 3 times shorter than the one of collisions with the background. This means scenario I is able to produce resonant structures in the Kuiper Belt.

Fig. 4.3 depicts the timescales for two example stars (see Tab. 2.1). Both stars host a resolved debris disc (Kalas et al., 2004; Liu, 2004; Greaves et al., 1998). On the left-hand side is the M1 dwarf star AU Microscopii. Because of the large mass-loss rates obtained for this star it is not surprising that the drag forces, especially the wind drag $\beta_{\mathrm{wind}} \approx 10 \ldots 300 \beta_{\mathrm{PR}}$, are very efficient and work much faster than any collision. Thus for the whole range of optical depth for debris discs the particles in the resonance are replenished so fast, that sustaining a resonant structure should not be a problem. But problems do arise considering the β dependence of the capture probability. A high β reduces the overall capture probability drastically and causes a preference for higher order resonances.

On right-hand side of Fig. 4.3 is the K2V star ϵ Eridani. It is not at active as AU Mic, but still has a mass-loss rate of $30 \dot{M}_\odot$ (Wood et al., 2002), which means that the wind drag is about 20-25 times more efficient than PR drag. The transition from drag to collision determined ensemble takes place at $\tau_0 \approx 5 \, 10^{-4}$.

At the moment observational data give only weak constrains to the actual optical depths of the AU Mic or the ϵ Eri disc. It is expected to be around $\tau_0 \approx 10^{-5} \ldots 10^{-4}$. This would result in a balance between drag and collisions. So scenario I could be responsible for resonant structures there, if not very pronounced ones because collisions are relatively
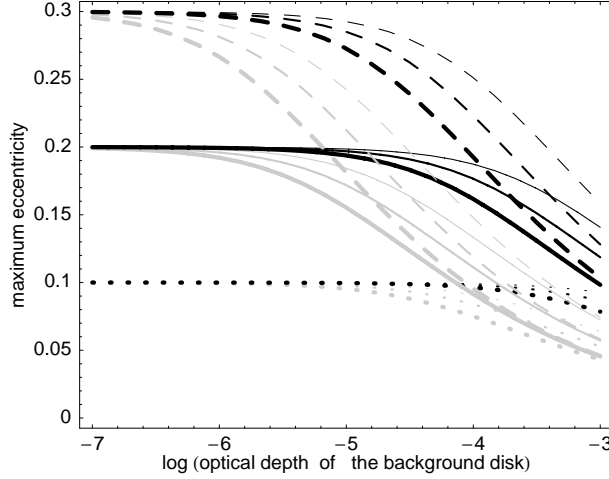
Figure 4.4: Maximum orbital eccentricity of the clump particles as a function of the optical depth of the "regular" disc τ_0. Dashed, solid, and dotted lines: $e_{\text{res}} = 0.3$, 0.2, and 0.1, respectively. Thick, medium, and thin lines correspond to $\beta = 0.05$, 0.10, and 0.20. Gray lines are for $\dot{M} = \dot{M}_\odot$, black lines for $\dot{M} = 30\dot{M}_\odot$.

fast.

The actual *lifetime* T of a resonant particle is determined by all sinks combined and given by

$$\frac{1}{T} \equiv \frac{1}{T_{\text{res}}} + \frac{1}{T_{\text{coll}}^0} + \frac{1}{T_{\text{coll}}}. \tag{4.37}$$

In graphic representation it is the lower envelope of all timescales depicted in Figs 4.2 and 4.3. The maximum eccentricity achieved by the particles in that time T is

$$e(T) \approx \sqrt{\frac{q}{p+q} BT} \equiv e_{\text{max}}. \tag{4.38}$$

This follows from Eq. (2.7) by inversion and a Taylor series expansion for small e_{max}. The calculation of T and e_{max} is an iterative problem, because T_{coll}^0 in Eq. (4.30) depends through n_0 on e_{max} (Eqs (4.21)–(4.17)) which, in turn, depends on T and thus back on T_{coll}^0 (Eqs (4.37)–(4.38)). In a first approximation one can use e_{res} for e_{max}, especially for dilute discs.

Fig. 4.4 depicts the maximum eccentricity as a function of the background optical depth. For illustrative purposes the data of ϵ Eridani have been chosen with $a_p = 40\,\text{AU}$. The semi-opening angle of the disc ϵ is proportional to the collisional lifetime T_{coll}^0, unfortunately it is unconstrained in the face-on view we have. In analogy with similar, but edge-on discs (β Pic, AU Mic) we set $\epsilon = 0.1 = 6°$. To show the effect of the high mass-loss rate, we added graphs for $1\,\dot{M}_\odot$ in grey lines.

For the high mass-loss rate measured, the maximum eccentricity is almost independent of the background optical depth up to $\tau_0 \sim 10^{-5}$, because drag and resonant pumping are very efficient in that case, see right panel of Fig. 4.3. For larger τ_0 the collisions start to

take over and $e_{\max}$ drops rapidly. In the case of a lower mass-loss rate the dependence on τ_0 is much stronger. In a dense debris disc, $\tau_0 \sim 10^{-3}$, $e_{\max}$ is smaller 0.1, independent of e_{res}, it only depends on the size.

This means the more dense or dusty a disc is, the lower the eccentricities in a resonant ensemble are. Instead of pronounced clumps, which need higher eccentricities, there will be narrow – if bright – rings only, compare e.g. Fig. 2.6 of this work.

Greaves et al. (2005) claim that three out of the six clumps seen in the ϵ Eri disc are real. Choosing a 4:3 MMR, which creates exactly 3 clumps this means the disc particles will have an eccentricity of $0.2 \ldots 0.25$. This is sufficient for non-axisymmetric structures. However, if the mass-loss rates are lower than claimed by Wood et al. (2002) the eccentricities would be too low to make clumps by resonant structuring according to this scenario.

4.1.4 Optical Depth

With all the timescales being specified, especially their dependence on n, the balance equation (4.16) can now be solved. It is a first order differential equation, but when inserting T_{coll} we see that it is not linear but quadratic in n. The general, time-dependent solution is

$$
\begin{aligned}
n = \frac{\hat{T}_{\mathrm{coll}}}{2} \Bigg[&\frac{-1}{T_{\mathrm{res}}} - \frac{1}{T_{\mathrm{coll}}^0} \\
&+ W \tanh\left(\frac{1}{2} W\, t + \operatorname{arctanh}\left(\frac{\frac{1}{T_{\mathrm{res}}} + \frac{1}{T_{\mathrm{coll}}^0}}{W} \right) \right) \Bigg]
\end{aligned}
\tag{4.39}
$$

$$
\text{with } W = \sqrt{ \frac{4\dot{n}^+ p_{\mathrm{res}}}{\hat{T}_{\mathrm{coll}}} + \left(\frac{1}{T_{\mathrm{res}}} + \frac{1}{T_{\mathrm{coll}}^0} \right)^2 }.
\tag{4.40}
$$

To determine the integration constant we assumed the initial condition

$$
n(t = 0) \equiv 0
$$

so that at the very beginning of our solution there will be no resonant particles, they will be caught step by step.

This nears its asymptotic limit very quickly, as seen in Fig. 4.5. So we will have an equilibrium-like status after a few orbits already. In equilibrium $dn/dt = 0$, which mathematically is equivalent to $t \to \infty$, the solution simplifies to

$$
n = \frac{\hat{T}_{\mathrm{coll}}}{2} \left[\sqrt{ \frac{4\dot{n}^+ p_{\mathrm{res}}}{\hat{T}_{\mathrm{coll}}} + \left(\frac{1}{T_{\mathrm{res}}} + \frac{1}{T_{\mathrm{coll}}^0} \right)^2 } - \left(\frac{1}{T_{\mathrm{res}}} + \frac{1}{T_{\mathrm{coll}}^0} \right) \right].
\tag{4.41}
$$

It has two limiting cases: very dense and very dilute resonant structures. In the first case we have perfect resonant capture, $p_{\mathrm{res}} = 1$ and slow collisions. Equation (4.21) shows that even then the background is anything but empty,

$$
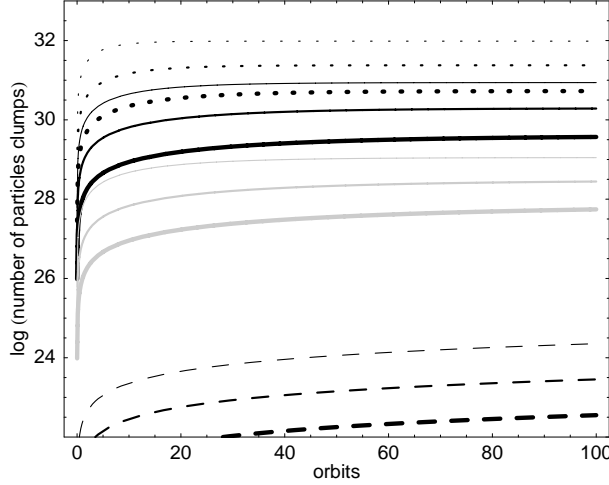n_0(p_{\mathrm{res}} = 1) = \frac{1}{2} \dot{n}^+ T_{\mathrm{drag}}.
$$

Figure 4.5: Number of resonant particles as a function of time for a Sun-like star ($M_* = M_\odot$) for a variety of parameters. Black lines: $\tau_0 = 10^{-5}$, grey lines $\tau_0 = 10^{-7}$. Solid: $a_p = 30AU$, $\dot{M}_* = \dot{M}_\odot$, dashed: $a_p = 0.1AU$, $\dot{M}_* = \dot{M}_\odot$, dotted: $a_p = 30AU$, $\dot{M}_* = 10\dot{M}_\odot$.

Both ensembles will be similarly populated. For real systems, however, this case is not very likely. More likely is the case of dilute clumps, $n \ll n_0$. Then we can neglect the n^2 term in the balance equation and thus make it linear. Its solution in this case is

$$n = \frac{\dot{n}^+ p_{\text{res}}}{T_{\text{res}}^{-1} + (T_{\text{coll}}^0)^{-1}} . \tag{4.42}$$

We will compare the linear and quadratic solution later.

To construct the normal, optical depth from the number density we also need the collisional cross section σ of a single particle and the total area of the resonant structures or clumps S,

$$\tau = n\frac{\sigma}{S} . \tag{4.43}$$

For a given particle size s the cross section is easily calculated to be $\sigma = \pi s^2$. The problem, however, is the determination of the clump size. The clumps are per definition not axisymmetric, their number depends on the resonant parameters p and q and their width and elongation depend on libration width and maximum eccentricity. There is no analytical representation or approximation with sufficient accuracy.

The most obvious possibility to make numerical approximations is integration of a derivative of the distribution function $\phi(.)$ over the annulus. E.g. define a 'clump' to be where the (normalized) number density of the particles exceeds a certain treshold ϕ_{min} and construct a spacial distribution $\Phi(x, y)$ which is 1 if $\phi(.) > \phi_{\text{min}} > 0$. But the distribution function of a resonant ensemble is highly nonlinear. Near the border of the resonance there are high, sharp peaks, in the middle very low minima. Even if an adequate ϕ_{min} is found, the resulting $\Phi(x, y)$ will not be a continuous function but one with lots of steps or jumps. Numerical integration of such a function is cumbersome.
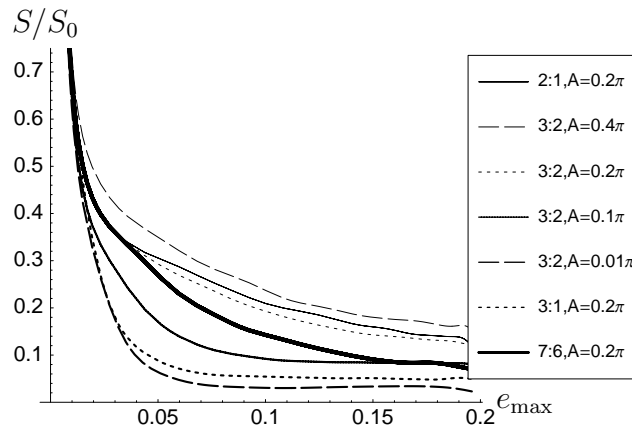
Figure 4.6: Size of the clumps of a resonant structure as a function of the maximum eccentricity, derived from scatterplots, for several 1st order resonances, one 2nd order one and several libration widths A. Curves smoothed to reduce numerical noise.

The alternative to estimate to the clump size can be found in scatterplots like Figs 2.6 and 2.7. To extract statements about the clump size from the data sets of positions of resonant particles we divide the annulus area into bins $(x_i + \delta x) \times (y_i + \delta y)$, count the particles per bin n_i and then define that the clump is where the number of particles exceeds a certain percentage k of the maximum number per bin n_{max}, $n_i \geq k n_{max}$. The ratio of the number resonant bins divided by the number of all bins gives the ratio of clump size S to annulus size S_0. The latter is determined by a_{res} and e_{max} according to

$$S_0 = 4\pi a_{res}^2 e_{max}.$$

Fig. 4.6 shows the results of such an "integration by counting". The curves were smoothed to reduce the numerical noise. In total there are 2 000 000 particles considered and the clump condition was set to $10\% \, n_{max}$. We considered several first order and a second order resonance, i.e. $q = 1$ and $q = 2$, respectively. For all of them the dependence in p is very subtle, stronger is the dependence on the libration width. For larger A, meaning weaker resonance, the clumps are more spread out, i.e. more dilute but also covering more space. For small A, meaning strong resonance, they are sharper and denser, but also concentrated in space and thus smaller. The fact that S/S_0 diverges for $e_{max} \to 0$ seems to contradict what we have seen in Fig. 2.6, the clump seems larger in the case of larger e_{max}. But in the small e_{max} case the arcs between the clumps become more pronounced. The smaller e_{max} the more "concentrated" the resonant ensemble is and the more of the arcs exceeds the clump condition $n_i \geq k n_{max}$. In the extreme $e_{max} \to 0$ the annulus becomes infinitely narrow and the resonant ensemble inhabits all of it. Numerically we divide by zero in the lower limit $e_{max} = 0$, but then we have neither an annulus nor clumps, but only a rotationally symmetric, bright ring. For an intermediate e_{max} of 0.2 and an intermediate A of 0.2π the relative clump size is $S/S_0 \approx 0.2$. We use this as a default value.
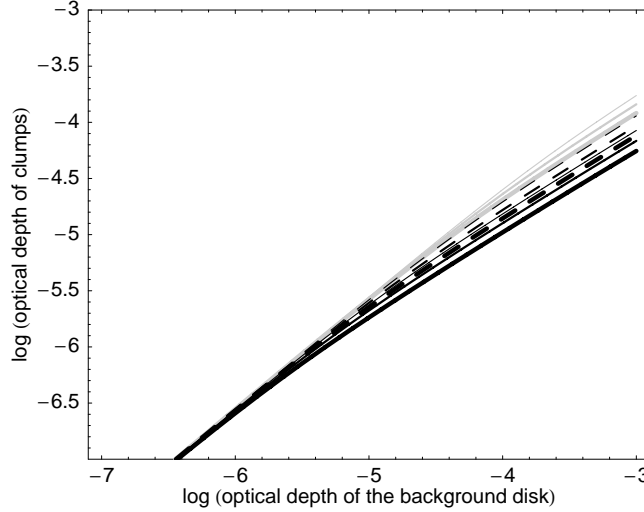
Figure 4.7: Normal optical depth of the resonant clumps τ as a function of the optical depth of the "regular" disc τ_0 for the Sun. Solid, black lines are for the actual mass-loss rate $1\dot{M}_\odot$ and the Kuiper Belt ($a_p = 30AU$). Dashed show a 10 times larger mass-loss rate, grey lines are for a resonant zodi, $a_p = 0.1AU$. Thick, medium, and thin lines correspond to $\beta = 0.05$, 0.10, and 0.20, respectively. The chosen resonance is 3:2, i.e. the Plutinos in the Kuiper Belt case.

Thus we are now able to estimate the optical depth of the resonant clumps. Figs. 4.7 to 4.9 show τ as a function of the background optical depth τ_0.

It is obvious from Fig. 4.7 that neither mass-loss rate nor position of the planet has a significant influence on the clumps' optical depth for a given central mass and resonance. Especially in the solar case, $\tau_0 \approx 10^{-6}$, there is no any difference for all parameters considered. In a very dense debris disc there are slight quantitative differences: a 10 times higher mass-loss rate gives about 10% denser clumps and those of a resonant zodiacal cloud ($a_p = 0.1AU$) are about twice as dense as a resonant Edgeworth-Kuiper Belt ($a_p = 30AU$).

The results of Fig. 4.8 are somewhat surprising. Although there is the very large difference between 1% and 100% capture probability the clump brightness is still only $\sim 10\%$ of the background with the perfect resonant capture. For $p_{\mathrm{res}} \equiv 0$ the clumps brightness will of course be identical zero. Heuristically one would expect an approximate equality of background and clumps in the case $p_{\mathrm{res}} = 1.0$. The lower panel with the p and q dependence seems to contradict what can bee seen in Fig. 3.10. There a larger q reduces the collisional rate considerably, which gives the clumps more time to develop and consequently a higher optical depth. But in the models considered here, we have fixed $\tilde{R}$ to 2, for all p, q and e_{max}. Inserting the results of Chapter 3 would probably lead to a compensation of the effects and result in a non-dependence on p and q.

Finally, Fig. 4.9 shows the clumps' optical depth for the debris disc host star ϵ Eridani. We use the proposed outer planet ($a_p = 40AU$) again and a 3:2 resonance. Plotted in solid lines is the solution of the full balance equation, in dashed lines that of the linearized
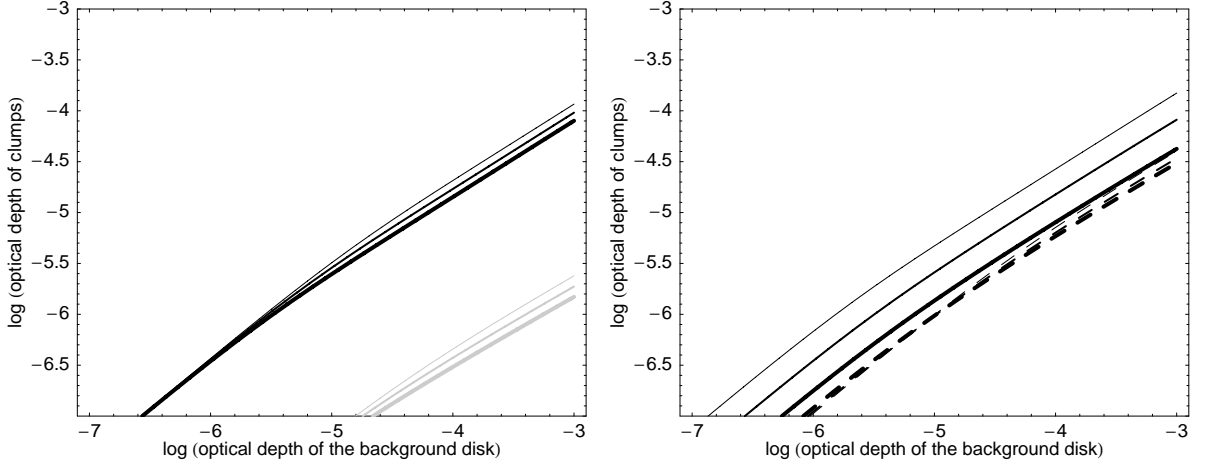
Figure 4.8: Normal optical depth of the resonant clumps τ as a function of the optical depth of the "regular" disc τ_0 for the Sun. Left panel: Dependence on the resonant capture probability. Black lines are for $p_{\text{res}} = 1.0$, grey ones for $p_{\text{res}} = 0.01$. Thick, medium, and thin lines correspond to $\beta = 0.05$, 0.10, and 0.20, respectively. Right panel: Dependence on resonance parameters p and q. Solid lines represent the first order resonances 2:1 (thick), 4:3 (medium) and 8:7 (thin). Dashed lines are for the higher order resonances 4:1 (thick), 6:1 (medium) and 8:1 (thick).
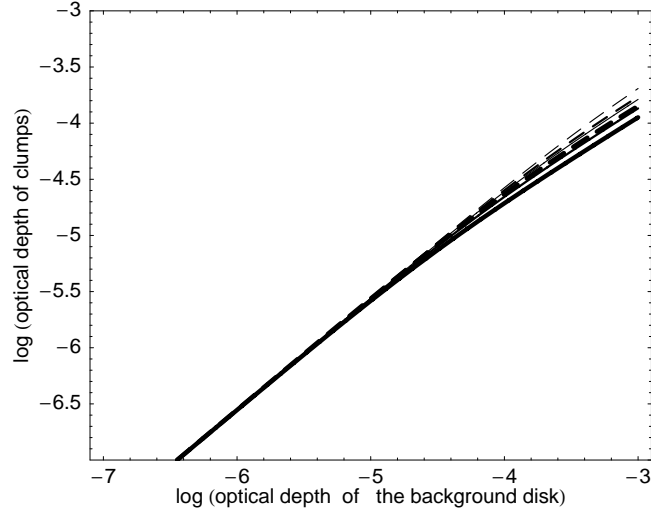

Figure 4.9: Normal optical depth of the resonant clumps τ as a function of the optical depth of the "regular" disc τ_0 for the debris disc host star ϵ Eri ($a_p = 40AU$, $\dot{M}_* = 30\dot{M}_\odot$). Solid lines show the full solution (4.41) of the balance equation and dashed ones the solution (4.42) of the linearized balance equation. Thick, medium, and thin lines correspond to $\beta = 0.05$, 0.10, and 0.20, respectively.

one. Since we have already seen in the upper panel of Fig. 4.8 even in the best case the clumps are much fainter than the background, the condition $n \ll n_0$ is always fulfilled and the approximated solution (4.42) is an excellent one for all τ_0. With ϵ Eridani's estimated optical depth of $\tau_0 \sim 10^{-5}$ the clumps' optical depth is about $\tau \sim 3\,10^{-6}$, one third of that of the background.

In Figs 4.10 and 4.11 there are contourplots showing the additional dependence on the planetary semimajor axis for several parameters. For the low mass star $M_* = 0.5 M_\odot$, that dependence is nonexistent, except for very large distances $a_p \sim 10^4 AU$. That is different for a higher mass star, $M_* = 5 M_\odot$. The further from the star the planet and thus the resonant structure is, the fainter it gets. The decrease in τ for increasing a_p is much more prominent for $1\dot{M}_\odot$ than $300\dot{M}_\odot$, because for high mass-loss rates drag and pumping effects are more efficient and lead to denser clumps in general. For low mass-loss rates the collisions are more dominating, thus the clumps are more dilute.

The dependencies on the resonances $(p + q) : p$ themselves are rather subtle, see the upper panels of Fig. 4.11. The influence of the β ratio is similar to that of the stellar mass-loss rate: high β means more efficient drag which means more dense clumps.

To allow quick numerical estimates for given sets of parameters we derive approximative formulas for the clumps' optical depth now. Therein we have to consider 4 cases: tenuous and dense discs as well as host stars with low and high mass-loss rate. We use the same ansatz as Krivov et al. (2007),

$$\frac{\tau}{\tau_0} = \frac{n}{n_0} \frac{1 - p_{\mathrm{res}}/2}{\hat{S}} = p_{\mathrm{res}} \frac{T}{T_{\mathrm{drag}}} \tag{4.44}$$

but include stellar wind next to PR effect in T_{drag}.

In the case of tenuous discs, the lifetime T is given mainly by the resonant timescale T_{res} and the maximum eccentricity e_{max} reaches e_{res}. Inserting both into (4.44) and simplifying we see that all β dependencies rule themselves out and get the very same result as Krivov et al. (2007),

$$\frac{\tau}{\tau_0} \approx 0.125 \left(\frac{p_{\mathrm{res}}}{0.5}\right) \left(\frac{\hat{S}}{0.2}\right)^{-1} \left(\frac{e_{\mathrm{res}}}{0.2}\right) \left(\frac{p + q}{q}\right). \tag{4.45}$$

In the case of dense discs we start with the distinction between high and low mass-loss rates. For high $\dot{M}_*$ the disc is transport dominated and T_{res} determines the lifetime, just as in the case of tenuous discs, and we again arrive at (4.45). For low $\dot{M}_*$ the situation is more complicated. Here the lifetime is determined by a combination of the timescales of collisions with the background and resonant timescale,

$$T = \left(\frac{1}{T_{\mathrm{res}}} + \frac{1}{T_{\mathrm{coll}}^0}\right)^{-1}. \tag{4.46}$$

This and the resulting complicated expression for the maximum eccentricity makes the derivation of a formula in the form of Eq. (4.45) impossible. Thus we restrict ourselves
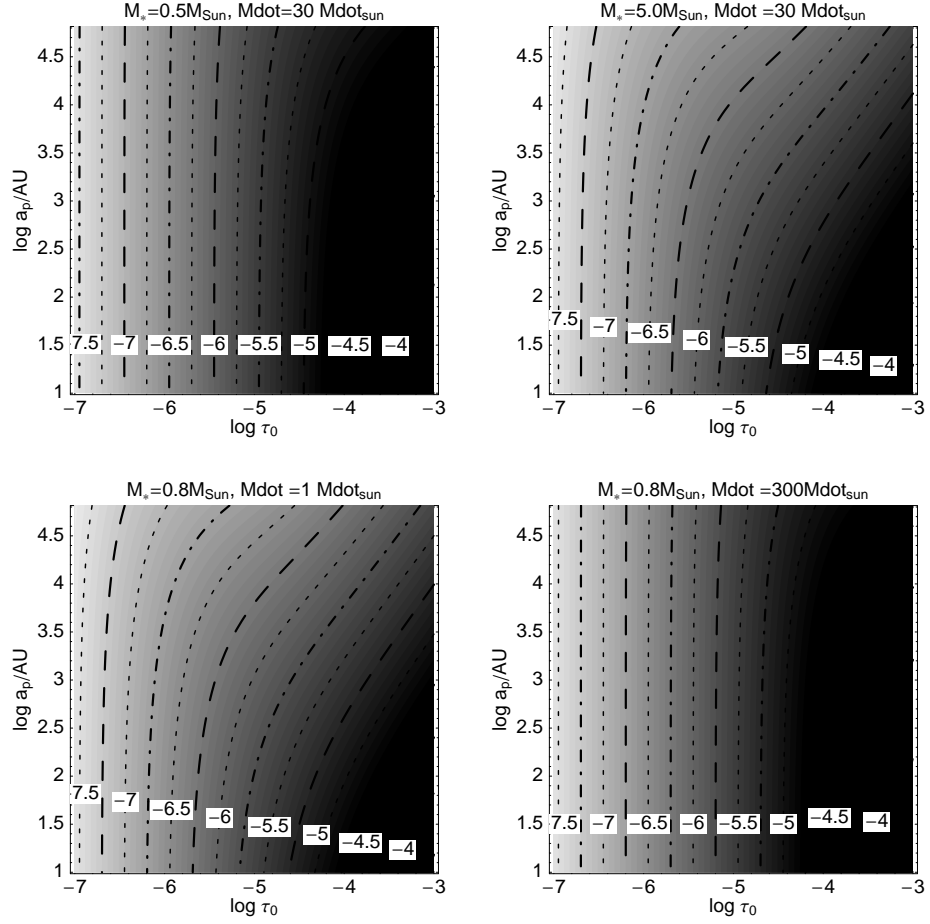
Figure 4.10: Contour plots of the normal optical depth of the resonant clumps τ, as a function of the optical depth of the "regular" disc τ_0 and the planet's distance from the star. Shown is a 3:2 resonance. The assumed is $\beta = 0.10$. Top left and right: stellar masses 0.5 and $5.0 M_\odot$. Bottom left and right: mass-loss rates of $1\dot{M}_\odot$ and $300\dot{M}_\odot$. Contours are labelled with the values of $\log \tau$.

to the case of a mass-loss rate so low that the lifetime is determined by T^0_{coll} alone. Then

$$e_{\max} \approx e(T^0_{\mathrm{coll}}) = \left(\frac{q}{p+q} \frac{\pi B a \sin \epsilon}{(1 - p_{res}/2) v_{\mathrm{kepler}} \tau_0} \right)^{1/3}, \tag{4.47}$$

and our approximated expression for dense discs and very low mass-loss rates is similar to the respective result of Krivov et al. (2007),

$$\tau \approx 9 \times 10^{-6} \left(\frac{M_*}{M_\odot} \right)^{1/6} \left(\frac{\beta_{\mathrm{PR}}}{0.1} \right) \left(1 + 0.29 \left(\frac{\dot{M}_*}{\dot{M}_\odot} \right) \left(\frac{L_\odot}{L_*} \right) \right)$$

$$\times \quad \left(\frac{\epsilon}{0.1\mathrm{rad}} \right) \left(\frac{\tau_0}{10^{-4}} \right)^{2/3}$$

$$\times \quad \left(\frac{p_{\mathrm{res}}}{0.5} \right) \left(\frac{\hat{S}}{0.2} \right)^{-1} \left(\frac{a_p}{100\,\mathrm{AU}} \right)^{-1/6} \left(\frac{p+q}{q} \right)^{2/3}. \tag{4.48}$$

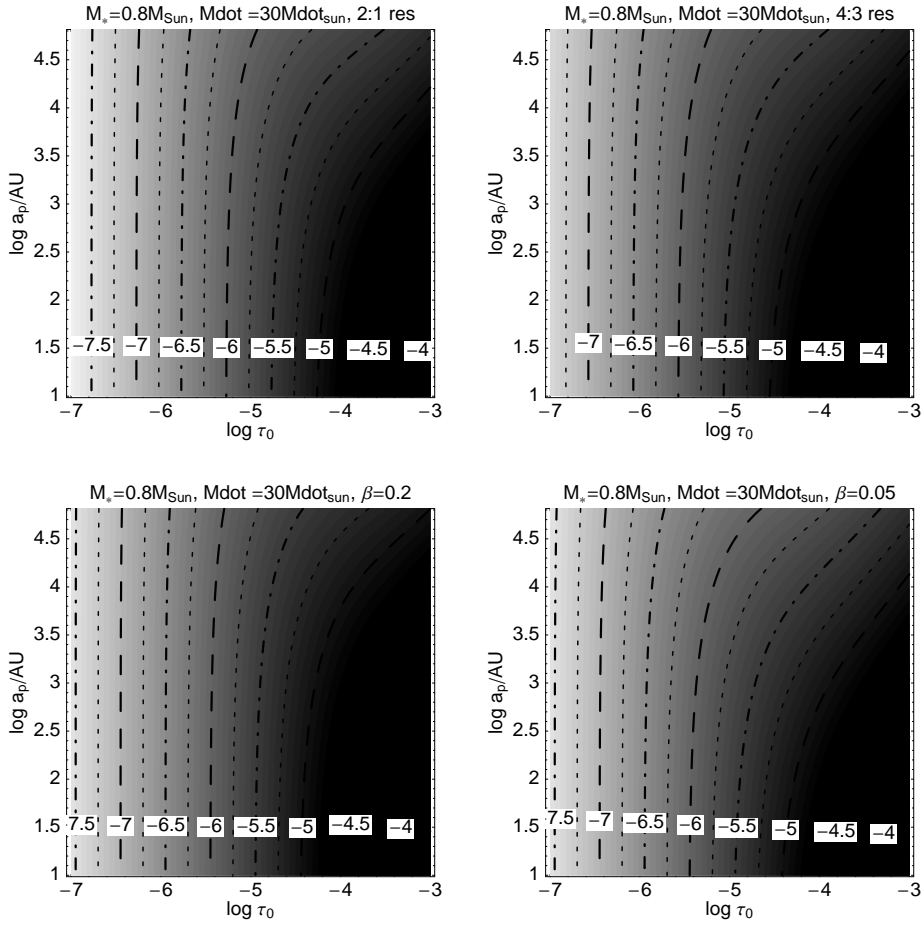Figure 4.11: Contour plots of the normal optical depth of the resonant clumps τ, as a function of the optical depth of the "regular" disc τ_0 and the planet's distance from the star. In each panel $M_* = 0.8 M_\odot$, $\dot{M}_* = 30 \dot{M}_\odot$. Top left and right: 2:1 and 4:3 resonance, respectively ($\beta = 0.1$ each). Bottom left and right: $\beta = 0.2$ and $\beta = 0.05$, respectively (3:2 resonance each). Contours are labelled with the values of $\log \tau$.

The difference is the mass-loss rate corrected β, see Eq. (4.12).

4.1.5   Contrast

Until now we have exclusively discussed the optical depth of the clumps, which is small compared to the background. But in any complete disc the background is *always* present, i.e. wherever there is a clump there is background "underneath". Thus, to get the *contrast* of a disc region with and without resonant clump we have to add τ to τ_0. The difference of optical depth in the presence of a clump is

$$\Delta\tau \;=\; \frac{\tau + \tau_0}{\tau_0}. \qquad (4.49)$$

Ergo, if $\tau \approx 0.1 \ldots 0.3\tau_0$ then the disc is about 10% to 30% denser in the region of resonant structures than around them.

To obtain the difference in brightness, i.e. the enhancement of observable flux, the physical properties, such as the temperature and efficiency of emisssion, have to be considered. What we can say, however, since both resonant and nonresonant ensembles consist of the same kind of dust grains, the brightness difference between background disc and resonant clump will be of the same order. Thus that the clumps developing as scenario I describes are just around the limit of observability when we compare it to the sensitivity of todays instruments. So does the SCUBA array – with which the images 2.2 were taken – have an accuracy of 5% - 15% depending on the wavelength (Greaves et al., 2005). Thus the resonant clumps in the ϵ Eridani disc would be just above the noise level and difficult to distinguish from the background.

4.1.6 Simplifications

In addition to the general assumptions – circular planetary orbit, 2D geometry, all collisions totally destructive and so on – we make further, model specific simplifications.

First we have fixed the resonant eccentricity e_{res}. Since it is given by p and q this means we restrict ourselves to one single resonance. But looking at the actual range of e_{res} for different important resonances we see that it ranges from 0.57 (2:1) to 0 (1:1). And according to Fig. 4.4 the actually achieved eccentricity e_{max} of a particle is more dependent on the background optical depth and mass-loss rate than e_{res}.

Second we have fixed the capture probability p_{res}. This is the place where the planetary mass M_p would enter into our models. Large planets tend to capture preferably into 2:1 resonance, where smaller ones prefers those closer to $(p + q)/p \approx 1$ (Reidemeister, 2007, and references therein). If M_p/M_* is too large, the particles' orbits tend to become chaotic instead of being caught into resonance, if on the other hand M_p/M_* is too low, the particles simply pass by the resonances without being caught (Kuchner & Holman, 2003). p_{res} also depends on distance to the star (given by a_p), the particles' size or the β ratio and very slightly on the inclination with respect to the planet. There have been attempts to find analytic or empirical formulas for p_{res} (Beaugé & Ferraz-Mello, 1994; Lazzaro et al., 1994), but only for some subspaces of the parameters. A numerical study of a wide range of parameters was recently performed by Reidemeister (2007). He found that the inclination dependence is minor, but the β dependence very strong: where there is perfect capture ($p_{\mathrm{res}} = 1$) at $\beta = 0.03$ it drops to zero at $\beta = 0.3$. We chose an intermediate value of $p_{\mathrm{res}} = 0.5$.

The third fixed parameter is the collisional rate within resonance. It does not appear explicitly in our modelling but in Eq. (4.25) we set $\tilde{R} = 2$ and implicitly used it later for all p, q and e_{max}, ignoring the results of Chap. 3.3. To include those correctly we would, e.g., have to apply another $\tilde{R}$ to every single e_{max} evaluated, meaning to every chosen τ_0. To keep our treatment simple we again set an intermediate value.

Apart from these numerical ones there is one major systematic assumption we make. We do our modelling for a single particle size only. While in the collision between a very small and a very big particle it will most probably not be destructive for the latter, Krivov et al. (2006) found that in collisions of like sized particles the bigger one will most probably be destroyed by the slightly smaller one. Thus when we ignore the other grain sizes we ignore those "destructors" and overestimate the collisional lifetimes T_{coll}^0 and T_{coll}.

4.1.7   Applications

This scenario is a somewhat classical one and was considered by several authors before. It was applied to the Solar System by Liou & Zook (1996) and Liou & Zook (1999)

By modelling perturbations induced by Jovian planets on the Edgeworth-Kuiper Belt dust disc, they found efficient resonant trapping of dust by Neptune, which produces arcs of dust co-orbital with the planet. According to their analysis, if the Solar System were observed from outside, the presence of at least Neptune and Jupiter would be obvious merely from analysing images of the dust disc. While the large-scale clumps on the outskirts of the Solar System still escape observational detection, there is one, so far the only, case where scenario I is observed at work: the asymmetric resonant ring of asteroidal dust around the Earth orbit. Predicted by Jackson & Zook (1989), it was identified in IRAS (Dermott et al., 1994) and COBE/DIRBE data (Reach et al., 1995).

In the case of ϵ Eri, Liou et al. (2000), Ozernoy et al. (2000), Quillen & Thorndike (2002), and Deller & Maddison (2005) have tried to find particular orbital parameters and masses of a planet, or planets, that may reproduce the observed substructure in the disc. To fit the observed structure they claim the planetary parameters to be $M_p = 0.1 M_J$, $a_p = 41.6 AU$ and $e_p = 0.3$. The latter, however, contradicts recent results by Reche et al. (2008). They found that, although eccentric planets still allow resonant capture, already a low eccentricity of $e_p = 0.05$ smears out the clumps and makes typical resonant structures invisible.

4.2   Scenario II

In the previous section we have seen that the timescales and optical depth of scenario I depend on a multitude of parameters. The efficiency and thus the success in explaining structures in observed discs depends in particular on the luminosity L_* and mass-loss rate $\dot{M}_*$ of the host star. E.g. scenario I might work in the case of ϵ Eridani if the published mass-loss rate of $\dot{M}_* = 30\dot{M}_\odot$ is true. If not and in the case of a less active star we need an alternative. That is offered by scenario II. Here the dust parent bodies *are* caught in a mean motion resonance. By mutual collisions among them smaller fragments and finally visible dust is produced right within the same resonance.

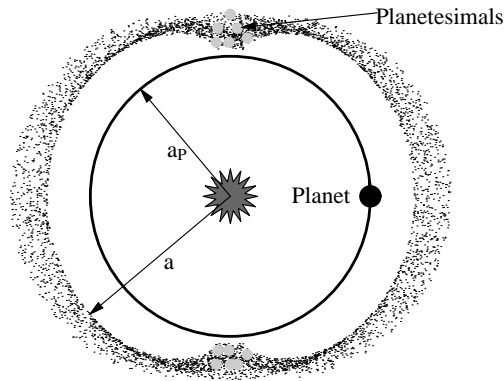Here we are confronted with other and in many cases larger difficulties than we had

Figure 4.12: Schematic representation of Scenario II. The particular resonant population with two clumps shown here again corresponds to the 3:2-MMR with $e_{\max} = 0.2$ and $A = 20°$.

with scenario I. There the dust production was not a matter of modelling, all the involved processes were merged in the dust injection rate $\dot{n}^+$. Which we were able to connect to the observable quantity "optical background depth", thus we gauged our model on the observations and there was no need to model the dust production itself.

In scenario II now the dust production is in the form of the collisional cascade the essential part of the model. It starts at planetesimal populations, which are totally unobservable for exoplanet systems. Along the way down to dust grains – across no less than about 30 orders of magnitude in mass – there exist a few benchmarks and constrains only. Therefore, we construct here the simplest possible model to explore the efficiency of scenario II, while being aware of its roughness.

4.2.1 The Set-up

To built our model we again assume a planet on a circular orbit and a group of planetesimals in a certain resonance. How they came into the resonance will not be considered here. Each of the planetesimals is small enough so that $m_{\mathrm{planetesimal}} \ll M_p$, but large enough so that they are not subject to the drag forces, i.e. $\beta = 0$. Consequently, there is no pumping of any eccentricity, compare Eq. (2.7), i.e. $e \neq e(t)$. They will not be ejected from the resonance, their configuration is stable. Because we want to let them collide and break up there must be a suitable number of them to replenish and sustain the dust on a long-term timescale. Their total mass M will be a free parameter of the model. All collisions will be catastrophic ones, see sec. 2.3. In contrast to the previous analysis we do keep the fragments of the collisions this time. They stay in the resonance and collide amongst each other again and again until they are ground down to a minimum size, to be specified later. Thus there is a collisional cascade grinding the material from the massive, but invisible planetesimals down to the smallest dust. We have a cloud or

swarm of resonant bodies in the clumps. Those small dust grains have a large surface and are thus observable. They form the visible structures.

Fig. 4.12 depicts the set-up of scenario II for a 3:2 resonance. This scenario is much simpler in concept than scenario I, but more difficult in analysis since now we have to consider the details of the collisions and model the cascade.

4.2.2   Locking Conditions

Although our model assumes that all fragments stay locked in the resonance, we have to consider under which conditions and to what extent that assumption is realistic. On the one hand material loss does occur because of the size of the fragments. For the large bodies we can ignore the drag forces, but for the smaller ones the β ratio grows larger and PR and wind drag have to be considered. If they get too dominant they may remove the grains from the resonant swarm. The size and the responding β will be called $s_{\min}$ and β_{crit}, respectively. Wyatt (2006) investigated locking conditions of resonant particles under the influence of radiation pressure and found a critical β ratio of

$$\beta_{\mathrm{crit}} = 0.034 \left(\frac{M_p/M_J}{M_*/M_\odot} \right)^{1/2}. \tag{4.50}$$

This is easily generalized to Poynting-Robertson plus stellar wind drag by simply interpreting the β as the combined one, including both forces. The minimum size not blown from the resonant swarm is

$$s_{\min} = s \left(\beta_{\mathrm{crit}} \right). \tag{4.51}$$

This blow-out is the result of the *direct* PR and wind effect. In contrast to the indirect one of sec. 4.1.1 this is velocity independend and does not drive inward transport processes, but makes a radial outward pressure. The combined β now is

$$\beta_{\mathrm{direct}} \;=\; \beta_{\mathrm{PR}} + \beta_{\mathrm{wind}} \tag{4.52}$$

$$\;=\; \frac{3}{16\pi} \frac{L_*}{GM_* c\rho s} \left(1 + \frac{\dot{M}_* c v_{\mathrm{wind}}}{L_*} \right), \tag{4.53}$$

and the wind's velocity v_{wind} appears explicitly. For the solar system velocity between $300 km/s$ and $800 km/s$ have been measured, depending on the activity. We adopt an intermediate value of $400 km/s$, as did Wood et al. (2002).

For a Sun-like star ($M_* = M_\odot$) and Jupiter-like planet ($M_p = M_J$) we have

$$\beta_{\mathrm{crit}} = 0.034 \quad \Leftrightarrow \quad s_{\min} = 10.8 \mu m.$$

For ϵ Eridani with $M_* = 0.8 M_\odot$ and an outer planet with an assumed mass of $M_p = 0.1 \ldots 1 M_J$ the critical β ratio (using $L_* = 0.34 L_\odot$ and $\dot{M}_* = 30 \dot{M}_\odot$) is

$$\beta_{\mathrm{crit}} = 0.012 \ldots 0.038 \quad \Leftrightarrow \quad s_{\min} = 9.2 \ldots 2.9 \mu m.$$
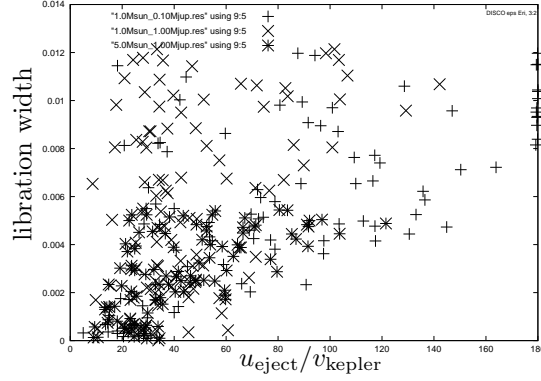
Figure 4.13: Velocity of ejection from the resonance, in units of Keplerian velocity V_{kepler}, as a function of the allowed libration width A. The planet was placed at $a_p = 40\,\text{AU}$. Differed plotsymbols represent data sets of different M_p/M_* relation, $+$: $M_p = 0.1 M_J, M_* = 1 M_\odot$, $\times$: $M_p = 1 M_J, M_* = 1 M_\odot$, $*$: $M_p = 1 M_J, M_* = 5 M_\odot$.

In a recently published paper considering our models (Krivov et al., 2007) a minimum size of $12\mu m$ was obtained for ϵ Eridani, but they used $L_* \propto M^4$.

On the other hand material may be lost due to too high velocity. The relative or collisional velocities of the colliders are much smaller than the orbital velocity v_{kepler} (compare e.g. Figs 3.5 and 3.7 of the previous chapter) and part of the kinetic energy will be used to break apart the colliders, but the fragments will still have a certain nonzero relative velocity with respect to their centre of mass. We will call this velocity "ejection velocity" u_{eject} – the fragments are ejected from the colliders during collision. The question is, what is the *critical* ejection velocity u_{crit} where the fragments leave the resonant swarm? To answer this question we performed some numerical experiments. A planet was placed at $40AU$, the parent bodies' eccentricity and inclination were set to zero. Following the analysis of Wyatt (2006) we chose different stellar and planetary masses: $M_* = 0.1, 0.2, 0.5, 1.0, 2.0, 5.0 M_\odot$ and $M_p = 0.03, 0.1, 0.3, 1.0, 3.0 M_J$, resulting in 30 different data sets. We simulated the orbital motion of 100 particles per (M_*, M_p) pair by direct integration of their equations of motion. The fragments were released within a resonance $(p + q) : p$ with a certain initial velocity u_{eject}. A β dependence was not investigated since that only gives a larger initial semimajor axis and eccentricity. We followed their motion and determined the resonant libration width A.

Results for 3 different sets of parameters are shown in Fig. 4.13. It shows a concentration in the region of both small velocity and small libration width and a tendency for larger libration for larger ejection velocities. Thus the resulting libration width is a function of the ejection velocity of the particles, or – inverting that function – the ejection velocity can be written as a function of the libration width, with a parametric dependence on stellar and planetary mass

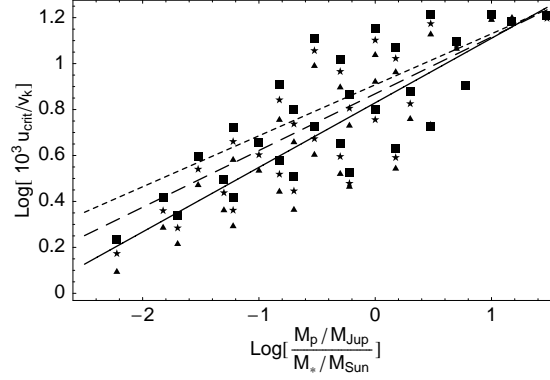$$\frac{u_{\text{eject}}}{v_{\text{kepler}}} = f(A; M_*, M_p). \tag{4.54}$$

Figure 4.14: Critical relative velocity of fragments $u_{\rm crit}/v_{\rm kepler}$ to stay in the resonance, as a function of the planet-to-star mass ratio. Symbols: results of individual runs (secondary data sets); lines: power law fits (4.56). Different maximum A of particles were adopted as a criterion of staying in the resonance: $A = 30°$ (triangles and solid line), $A = 40°$ (squares and dashed line), $A = 50°$ (stars and dotted line).

M_*	$1 M_\odot$	$1 M_\odot$	$0.8 M_\odot$	$0.8 M_\odot$
M_p	$1 M_\oplus$	$1 M_J$	$0.1 M_J$	$1 M_J$
$u_{\rm crit}/v_{\rm kepler}$	$1.36\ 10^{-3}$	$3.01\ 10^{-3}$	$3.73\ 10^{-3}$	$7.13\ 10^{-3}$

Table 4.3: Some examples of critical ejection velocities for collisions within a resonant swarm. The allowed libration width is set to $30°$.

We fitted our data sets to a power law aA^b. To determine a critical velocity we have to set limits on A to distinguish still caught from ejected particles. Thus we create 'secondary data sets' with certain $u_{\rm crit}$ for each triple of chosen A, M_* and M_p,

$$\frac{u_{\rm crit}}{v_{\rm kepler}} \;=\; f\left(M_*, M_p;\, A\right). \tag{4.55}$$

Knowing that resonant dynamics depend on the ratio M_p/M_* rather than the individual values, we fitted the secondary data to

$$\frac{u_{\rm crit}}{v_{\rm kepler}} \;=\; \mathcal{A}\left(M_p/M_*\right)^{\mathcal{B}}, \tag{4.56}$$

for libration widths between $A = 30°$ and $A = 50°$ excluding the shallow resonances easily destroyed by any perturbation.

Fig. 4.14 shows both the data sets and the fitted lines of $u_{\rm crit}$ as a function of M_p/M_* for three choices of libration width. The results of the fits by linear regression were $\mathcal{A} = 6.7\,10^{-3}$ and $\mathcal{B} = 0.28$ for $A = 30°$ and $\mathcal{A} = 8.1\,10^{-3}$ and $\mathcal{B} = 0.22$ for $A = 50°$ with errors of $\approx 10\%\ldots40\%$ for $\mathcal{A}$ and $\approx 10\%$. Table 4.3 shows some example values.

We will continue with the analysis of a stronger resonance ($A = 30°$) and choose

$$u_{\rm crit} \;=\; 6.7 \cdot 10^{-3} \left(M_p/M_*\right)^{0.28} v_{\rm kepler}. \tag{4.57}$$

Both Figures 4.13 and 4.14 show rather wide spread data, which implies that there is a further or more complicated functional dependence of the velocities than we considered here. But they also show that in 0th order approximation the numerical data fit our assumption well enough. For the sake of the simplicity of our models we will not go into further detail to obtain the critical velocity for particle loss from the resonance.

4.2.3 Collisional Cascade

As sketched in Sec. 4.2.1 the particles in the resonant clumps go through a collisional cascade, which grind the largest ones ($s = s_{\max}$) step by step down to the smallest ones ($s = s_{\min}$). The choice of $s_{\max}$ is an arbitrary one, typical values are $s_{\max} \sim 10km$. $s_{\min}$, however, is fixed by β_{crit}, as discussed above.

To model the collisional cascade we first need the distribution of fragments of a single collision, in size as well as in velocity. That outcome is not easy to determine. It depends e.g. on the collisional velocity and angle, target and projectile size, composition, morphology or porosity. Experiments are only possible for the lower end of the size distribution, for sizes of centimetres, sometimes up to metres. For the extrapolation to all sizes scaling laws are needed. They are the result of theoretical work and often, due to the lack of data, no more than educated guesses.

The mass-loss due to $\beta > \beta_{\mathrm{crit}}$ is minor, due to the little mass these very small particles carry. Most important is the loss due to high ejection velocity, $u > u_{\mathrm{crit}}$. Labelling the ratio of fragments kept by Ψ we schematically need the following:

$$\Psi = \frac{\text{all fragments} - \text{ those with } u > u_{\mathrm{crit}}}{\text{all fragments}}. \tag{4.58}$$

To estimate the amount of *those with $u > u_{\mathrm{crit}}$* we follow the analysis of Nakamura & Fujiwara (1991). They experimentally investigated destructive collisions of different materials and performed a thorough analysis of the obtained data. They give the cumulative mass of the fragments with $u > u_i$ to be

$$M(u > u_i) = \frac{\mathcal{N}}{2 - \tilde{\gamma}} M_t \left(\frac{u_i}{u_0}\right)^{-\gamma}, \tag{4.59}$$

where M_t is the target mass and u_0 the fragments mean velocity. $\tilde{\gamma}$ and γ are material parameters, which depend on the size and velocity distribution of a single collision and were experimentally determined. $\mathcal{N}$ is the prefactor of the Dohnanyi (2.9) distribution and a fit paramter.

Inserting (4.59) into (4.58) we have

$$\Psi(< u_{\mathrm{crit}}) = 1 - \left(\frac{u_0}{u_{\mathrm{crit}}}\right)^{\gamma} \qquad (u_{\mathrm{crit}} \geq u_0). \tag{4.60}$$

This is the loss after *one* collision. It remains to estimate the loss during the cascade. To do this we will extrapolate Eq. (4.60) for a series of collisions,

$$\Psi_{\mathrm{cascade}} = \Psi_1 \times \Psi_2 \times \Psi_3 \times \cdots \times \Psi_k, \tag{4.61}$$

where the indices denote the number of the collision, k is the total number of collisions it takes to grind down s_{max} to s_{min}. Krivov et al. (2007) found that in the case $s_{\mathrm{max}} = 10km$ and $s_{\mathrm{min}} = 30\mu m$ the mean number of collisions is

$$k \approx 8.$$

Each iterative Ψ_i can be written in the form of (4.60). But the mean velocity of the fragments grows with each collision, whenever hit by a projectile the particle gets propelled away from the centre of mass,

$$u_{0,i+1} \quad = \quad u_{0,i}\delta u. \qquad (4.62)$$

In which the velocity gain depends on the ratio of minimum and maximum mass of the fragments produced (see Krivov et al. (2007) for more details),

$$\log(\delta u) \quad \sim \quad \log\left(\frac{m_{\mathrm{max}}}{m_{\mathrm{min}}}\right) \gg 1. \qquad (4.63)$$

Thus means that the mean velocity grows rapidly and most of the mass is lost in the last collision,

$$\Psi_{\mathrm{cascade}} \quad \approx \quad 1 - \left(\frac{u_{0,\mathrm{final}}}{u_{\mathrm{crit}}}\right)^{\gamma}. \qquad (4.64)$$

For simplicity we drop the extra index, thus:

$$\Psi_{\mathrm{cascade}} \quad \approx \quad 1 - \left(\frac{u_0}{u_{\mathrm{crit}}}\right)^{\gamma}. \qquad (4.65)$$

With the last one being the one at the lower end of the size distribution $u_{0,\mathrm{final}}$ is the mean velocity of fragments measured in the experiments u_0. For non-monolithic solids Nakamura & Fujiwara (1991) obtained $\gamma = 2.3\ldots1.9$ and $u_0 = 4.4\ldots6.4m/s$, depending on the material. Consistent results of $u_0 = 5\ldots20\,m/s$ were found by Arakawa et al. (1995); Giblin et al. (1998). We will use the intermediate values $\gamma \approx 2$, $u_0 \approx 5m/s$. Comparing this to the Keplerian velocities for e.g. the Kuiper Belt and the ϵ Eri ring we find

$$u_0 \sim 10^{-4} v_{\mathrm{kepler}},$$

which in turn means (compare Fig. 3.5 and 3.7)

$$u_0 \sim 10^{-3} v_{\mathrm{imp}}.$$

Table 4.4 gives some examples of the *lost* fraction of particles $1 - \Psi$. For the resonance of an Earth mass planet 45% of the material is lost when undergoing a collisional cascade. But remember that the critical velocity u_{crit} was calculated for an 3:2 resonance. This and other resonances further from the planet are known to be rather weak for low mass planets like the earth (Kuchner & Holman, 2003). For Jupiter the further out ones are

stellar mass	$M_\odot$	$M_\odot$	$0.8 M_\odot$	$0.8 M_\odot$
planet's mass	$M_\oplus$	M_J	$0.1 M_J$	M_J
$1 - \Psi$	0.45	$1.1\ 10^{-3}$	0.10	$2.77\ 10^{-2}$

Table 4.4: Some examples for the lost fraction after a collisional cascade within a resonant swarm. The allowed libration width is set to 30°.

the strongest, and here less than 1% of the material is lost. The situation is similar for the proposed outer planet of ϵ Eridani. In the expected mass range of $0.1 \ldots 1 M_J$ between 10% and 3% are lost. That means most of the material is kept in the resonant swarm when undergoing a collisional cascade and that swarm can be described as a closed system. Thus we can apply the Dohnanyi theory,

$$n(m) \quad \propto \quad m^{-1-\alpha}. \tag{4.66}$$

Dohnanyi himself obtained a slope α of 5/6 (Dohnanyi, 1969). In the region of our minimum size $s_{\min}$ of several μm the work of Durda & Dermott (1997) implies a power law index of $k = -2.75$ in Eq. (2.12) and thus

$$\alpha = 0.87 \,. \tag{4.67}$$

Ergo the size distribution within the swarm of colliding and fragmenting resonant particles is fully determined as

$$n(m) \propto n^{-1-0.87}. \tag{4.68}$$

4.2.4   Swarm Cross Section

To make estimates about observables quantities such as the optical depth we first have to calculate the collisional cross section of our resonant ensemble. For scenario I we solved the balance equation, obtained the number of resonant particles n and simply multiplied that with the collisional cross section of a single one $\sigma(s^2)$ to get the one for the whole ensemble. For scenario II the ensemble does not consist of equally sized bodies anymore, we have to consider their size distribution $n(s)$.

The total cross section of the swarm of colliding, resonant particles is

$$\Sigma = \Psi_{\text{cascade}} \int_{s_{\min}}^{s_{\max}} \sigma(s) n(s) ds \,, \tag{4.69}$$

where $\sigma(s) = \pi s^2$ as above and $n(s)$ is obtained from $n(m)$ by

$$n(s) \quad = \quad n\left(m(s)\right) \frac{dm}{ds} \tag{4.70}$$

$$\text{with}\ \ m(s) \quad = \quad \frac{4}{3} \pi \rho s^3, \tag{4.71}$$

ρ being the uniform density of the particles. Inserting (2.9), (4.70) and (4.71) the swarm collisional cross section is

$$\Sigma \;\; = \;\; \Psi_{\text{cascade}} \, \mathcal{N} \frac{3\pi}{2-3\alpha} \left(\frac{4}{3}\pi\rho \right)^{-1-\alpha} \left(s_{\text{max}}^{2-3\alpha} - s_{\text{min}}^{2-3\alpha} \right) \tag{4.72}$$

$$= \;\; \Psi_{\text{cascade}} \, \mathcal{N} \frac{3\pi}{2-3\alpha} \left(\frac{4}{3}\pi\rho \right)^{-2/3} \left(m_{\text{max}}^{2/3-\alpha} - m_{\text{min}}^{2/3-\alpha} \right) . \tag{4.73}$$

To ascertain $\mathcal{N}$ we calculate the total mass in the swarm in a similar way,

$$\mathfrak{M} \;\; = \;\; \int_{m_{\text{min}}}^{m_{\text{max}}} m \, n(m) dm \tag{4.74}$$

$$= \;\; \mathcal{N} \frac{1}{1-\alpha} \left(m_{\text{max}}^{1-\alpha} - m_{\text{min}}^{1-\alpha} \right) . \tag{4.75}$$

Inserting this into (4.73) we have

$$\Sigma \;\; = \;\; \Psi_{\text{cascade}} \, 3\pi \frac{1-\alpha}{2-3\alpha} \left(\frac{4}{3}\pi\rho \right)^{-2/3} \mathfrak{M} \frac{\left(m_{\text{max}}^{2/3-\alpha} - m_{\text{min}}^{2/3-\alpha} \right)}{\left(m_{\text{max}}^{1-\alpha} - m_{\text{min}}^{1-\alpha} \right)} . \tag{4.76}$$

To bring this into a more convenient form we make use of $m_{\text{min}} \ll m_{\text{max}}$, thus we can approximate

$$\frac{1}{\left(m_{\text{max}}^{1-\alpha} - m_{\text{min}}^{1-\alpha} \right)} \;\; \approx \;\; \frac{1}{m_{\text{max}}^{1-\alpha}} \tag{4.77}$$

and, since $2/3 - \alpha < 0$ for all small particle regimes (see Fig. 12 of Durda & Dermott (1997)),

$$m_{\text{max}}^{2/3-\alpha} \;\; \ll \;\; m_{\text{min}}^{2/3-\alpha} \tag{4.78}$$

$$\Rightarrow \left(m_{\text{max}}^{2/3-\alpha} - m_{\text{min}}^{2/3-\alpha} \right) \;\; \approx \;\; m_{\text{min}}^{2/3-\alpha} . \tag{4.79}$$

Finally we obtain for the swarm's cross section

$$\Sigma \;\; = \;\; \Psi_{\text{cascade}} \, 3\pi \frac{1-\alpha}{2-3\alpha} \left(\frac{4}{3}\pi\rho \right)^{-2/3} \frac{\mathfrak{M}}{m_{\text{max}}^{1-\alpha} \, m_{\text{min}}^{-2/3+\alpha}} . \tag{4.80}$$

For Dohnanyi's $\alpha = 5/6$ this becomes symmetric

$$\Sigma = \Psi_{\text{cascade}} \, \pi^{1/3} \left(\frac{3}{4\rho} \right)^{2/3} \frac{\mathfrak{M}}{m_{\text{min}}^{1/6} \, m_{\text{max}}^{1/6}} . \tag{4.81}$$

4.2.5   Optical Depth

The optical depth of the resonant clump created by the colliding swarm of particles is now

$$\tau \;\; = \;\; \frac{\Sigma}{S} , \tag{4.82}$$

where S is the size of the clump. We will again use

$$S = 4\pi e_{\max} a^2 \hat{S}$$

and $\hat{S} \approx 0.2$, see Fig. 4.6 and surrounding text. With this the 'annulus' from scenario I reenters through a 'back door'. But here – in contrast to scenario I – it only sets the maximum eccentricity allowed and not a background to be overcome in brightness by the clumps.

In this scenario the optical depth and thus the brightness of the resonant structure does *not* depend on that of the background, but on the planetesimal mass and thus on the amount of material provided in the resonance. The full functional dependence of τ in this model is

$$\tau = f\left(\mathfrak{M}, a_p, \ \alpha, u_0, \gamma, \ m_{\min}, m_{\max}\right).$$

The dependence on the parameters of the collision α, u_0, γ is shown in Fig. 4.15. Here the host star is the Sun, $M_* = M_\odot, \dot{M}_* = \dot{M}_\odot$ and the planet is placed at Neptune's orbit, $a_p = 30AU$. The resonance was chosen to be 3:2, i.e. it represents the Plutinos in the Kuiper Belt. It shows that most important for the determination of τ is the choice of the correct slope α of the size distribution (thick dotted and solid line). The choice of a typical or mean velocity u_0 of the fragments or the fracturing exponent γ have a minor influence, only. The hardly visible difference between $u_0 = 5m/s$ and $u_0 = 1m/s$ hints at the maximum possible τ for a given planetesimal mass $\mathfrak{M}$. If the mean velocity were zero, there would be no loss during the collisional cascade, leading to a maximum optical depth in the vicinity of $\tau = \tau(u_0 = 1m/s)$. As long as the lost fraction is of the order of 10^{-3} the choice of u_0 makes hardly any difference. However, when it becomes large enough so that several percent are lost, the difference becomes more pronounced, as seen for $u_0 = 10m/s$.

Fig. 4.16 shows on the one hand the clumps' optical depth for the two debris disc host stars ϵ Eridani (solid lines) and AU Microscopii (dashed lines) and on the other hand illustrates the dependence on $\dot{M}_*$ and a_p. Via the mass $m_{\min}$ of the smallest, still bound particles the optical depth indirectly depends on the host star's luminosity and mass-loss rate. This dependence as well as that on $m_{\max}$ is weak, as can be seen in Eq. (4.80) and in Fig. 4.16. A thirty times larger mass-loss rate, and thus about thirty times larger $s_{\min}$ reduces the clump optical depth by far less than 2 times. For lack of better estimations the planet was placed in the region of the brightness depletion at $29AU$.

For ϵ Eridani we compared two very different planet positions. First the inner one found by radial velocity measurements. It would shape a hypothetical zodiacal cloud of this system, so far there is no observational evidence for its existence. It would, however, have much denser resonant clumps than the actually observed outer disc, structured by the planet proposed to be at $40AU$. That figure also tells us that we only need a planetesimal swarm of less than 10% Earth mass around ϵ Eri to create clumps of the optical depth
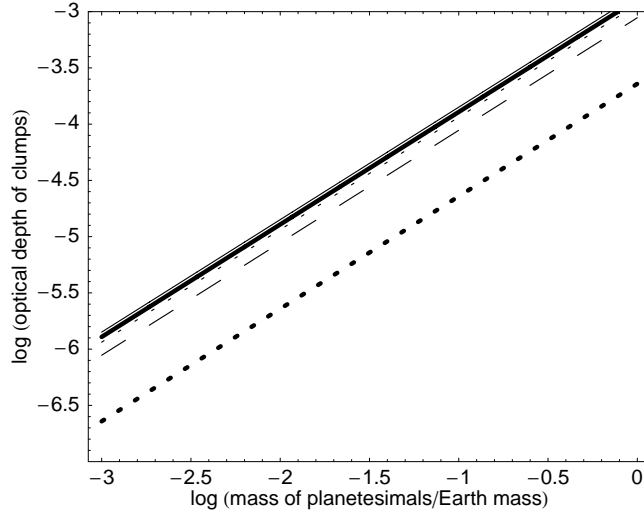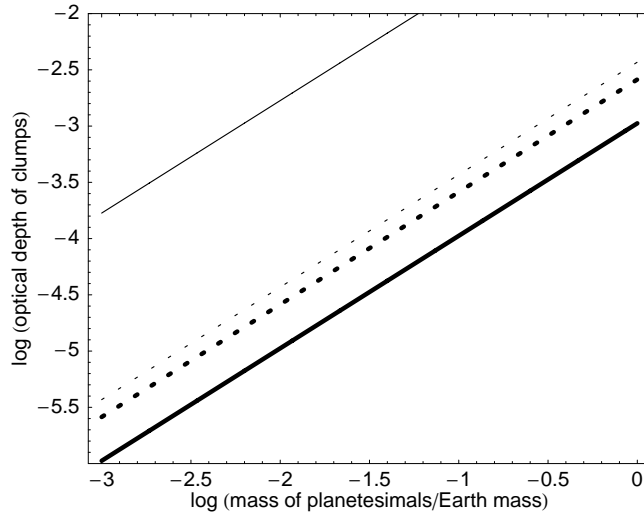
Figure 4.15: Normal optical depth of the resonant clumps τ in scenario II, as a function of the planetesimal population mass $\mathfrak{M}$, exemplified for the Kuiper Belt of our Solar System: $M_* = M_\odot$, $\dot{M}_* = \dot{M}_\odot$ and $a_p = 30AU$. Thick lines are for $u_0 = 5\,\mathrm{m\,s}^{-1}$ and $\gamma = 2$ and two different α: Dohnanyi's $\alpha = 0.833$ (dashed) and a more realistic $\alpha = 0.87$ (solid). Thin lines are for $\alpha = 0.87$ and different u_0 and γ: $u_0 = 1\,\mathrm{m\,s}^{-1}$ and $\gamma = 2$ (solid), $u_0 = 10\,\mathrm{m\,s}^{-1}$ and $\gamma = 2$ (dashed), $u_0 = 5\,\mathrm{m\,s}^{-1}$ and $\gamma = 1.5$ (dotted).

Figure 4.16: Normal optical depth of the resonant clumps τ in scenario II, as a function of the planetesimal population mass $\mathfrak{M}$, exemplified for ϵ Eri and AU Mic, $u_0 = 5\,\mathrm{m\,s}^{-1}$ and $\gamma = 2$ in all cases. Solid: ϵ Eri with the planet proposed to explain the clumps at $a_p = 40AU$ (thick) and the radial velocity one at $a_p = 3.4AU$ (thin). Dashed: AU Mic, with the two mass-loss rates $\dot{M}_* = 10\dot{M}_\odot$ (thin) and $\dot{M}_* = 300\dot{M}_\odot$ (thick). The planet was placed at $a_p = 29AU$

$\tau \approx 10^{-4}$, as observed. For AU Mic there one needs 5% to 10% Earth mass, depending on the actual mass-loss rate, to create equally bright clumps.

The contour plots Fig. 4.17 and 4.18 show, in addition to the dependence on the planetesimals' mass, that on the planet's semimajor axis, i.e. the distance of the clumps to the star. As the 'standard case' we chose an ϵ Eridani like system with $M_* = 0.8 M_\odot$, $\dot{M}_* = 30 \dot{M}_\odot$, $M_p = 0.1 M_J$, a 3:2 resonance and a size distribution with the slope $\alpha = 0.87$.

The most prominent contrast to similar plots of scenario I (cf. Fig. 4.10) is the existence of a critical distance a_{crit} of the resonant particles where the clumps' optical depth drops to zero,

$$\tau = 0 \quad \Leftrightarrow \quad a_{\mathrm{res}} \geq a_{\mathrm{crit}}. \tag{4.83}$$

That is the distance where the critical ejection velocity u_{crit} equals the fragments' mean velocity u_0, which means that Ψ is zero and no material remains within the resonance after the collisional cascade. The crucial term for that a_{crit} is the fraction of fragments kept,

$$\tau(a_p) \sim \Psi = 1 - \left(\frac{u_0}{u_{\mathrm{crit}}}\right)^\gamma. \tag{4.84}$$

We determined u_{crit} as a function $f(M_*, M_p) v_{\mathrm{kepler}}$ and thus also a function of the distance to the star a_{res}. Inserting Eq. (4.56) as well as $u_0 = 5 m/s$ and $\gamma = 2$ we get

$$\tau \sim 1 - 6.6 \, 10^{-4} \left(\frac{M_*}{M_\odot}\right)^{-0.44} \left(\frac{M_p}{M_J}\right)^{-0.56} \left(\frac{a_p}{AU}\right) \left(\frac{p+q}{p}\right)^{2/3}. \tag{4.85}$$

In the case of ϵ Eridani with $M_* = 0.8 M_\odot$, $M_p = 0.1 M_J$ and a 3:2 resonance the optical depth will be zero at $a_p \approx 307 AU$, which is just out of the upper edge of the plots' panels. The critical semimajor axis is reached earlier for smaller stellar or smaller planetary masses, shown clearly in Eq. (4.85), the upper panels of Fig. 4.17 and middle panel of Fig. 4.18. Concerning the resonance $(p+q) : p$ itself the resonant semimajor axis a_{res} is $\sim ((p+q) : p)^{2/3}$, the resonant locations are closer to the planet (for constant q) and thus a_{crit} increases with increasing p.

Of the other parameters tested the choice of a more realistic $\alpha = 0.87$ enlarges the optical depth of about one half of an order of magnitude. A more massive and thus more luminous star as well as a larger mass-loss rate both result in less dense clumps. The actual *brightness* observed around a given star, however, will depend on the amount of light irradiated upon the dust particles. Thus the lower optical depth and the larger amount of provided light might rule each other out.

For quantitative analysis we rewrite Eq. (4.82) in a more convenient form. For simplicity we assume that $\Psi \approx 1$, if that approximation is not possible the following has to be corrected as given by Eq. 4.85. We insert (4.80) into (4.82) and express m_{max} and m_{min} by s_{max} and s_{min}, respectively. The latter is defined as $s(\beta_{\mathrm{crit}})$ and thus

$$s_{\mathrm{min}} \quad \sim \quad \frac{1}{\beta_{\mathrm{PR}}} \left(1 + \frac{\dot{M}_* c v_{\mathrm{wind}}}{L_*}\right)^{-1}. \tag{4.86}$$
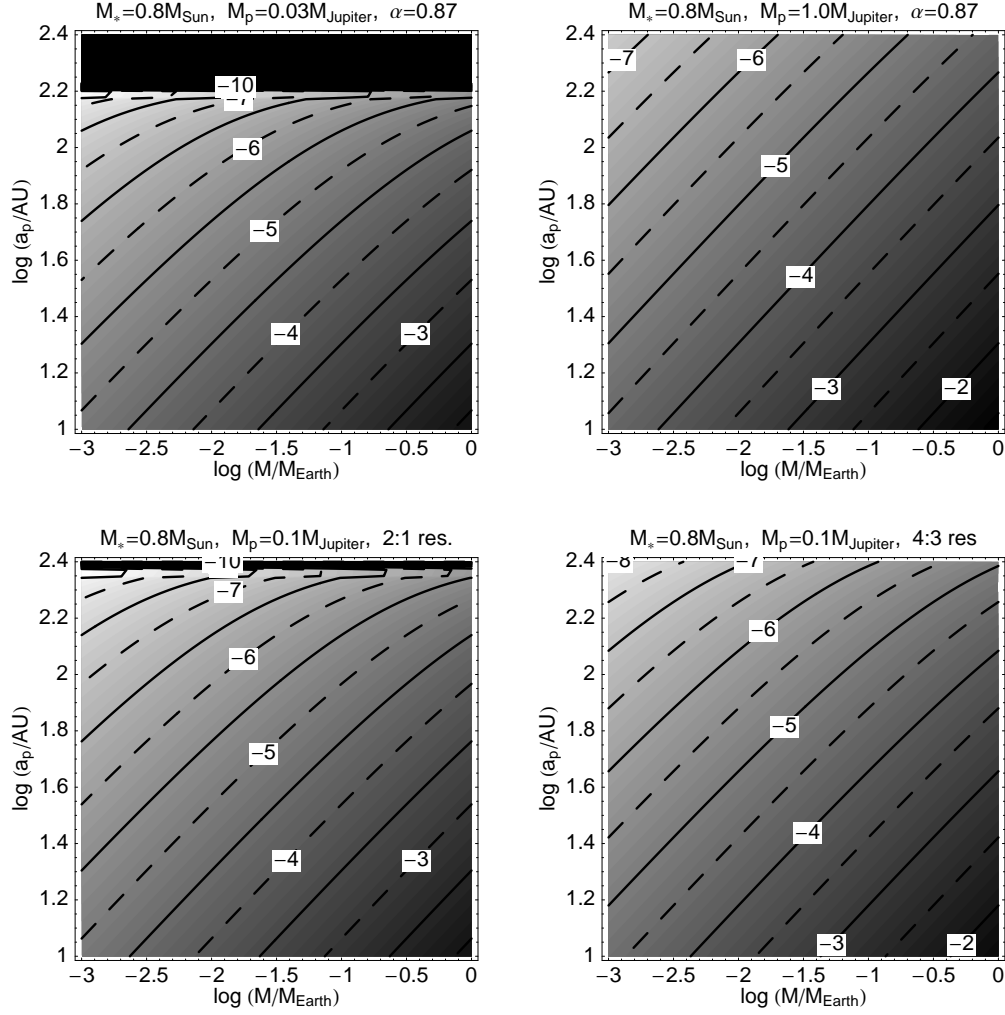
Figure 4.17: Contour plots of the normal optical depth of the resonant clumps τ in scenario II, as a function of the planetesimal population mass $\mathfrak{M}$ and the planet's distance from the star. In each panel $\alpha = 0.87$, $M_* = 0.8 M_\odot$ and $\dot{M}_* = 30 \dot{M}_\odot$. Top left and right: A 3:2 resonance for planetary masses of $M_p = 0.03 M_J$ and $M_p = 1.0 M_J$, respectively. Bottom left and right: 2:1 and 4:3 resonance, respectively, of a 0.1 Jupiter mass planet. Contours are labelled with the values of $\log \tau$. Cf. Fig. 4.10 for scenario I.
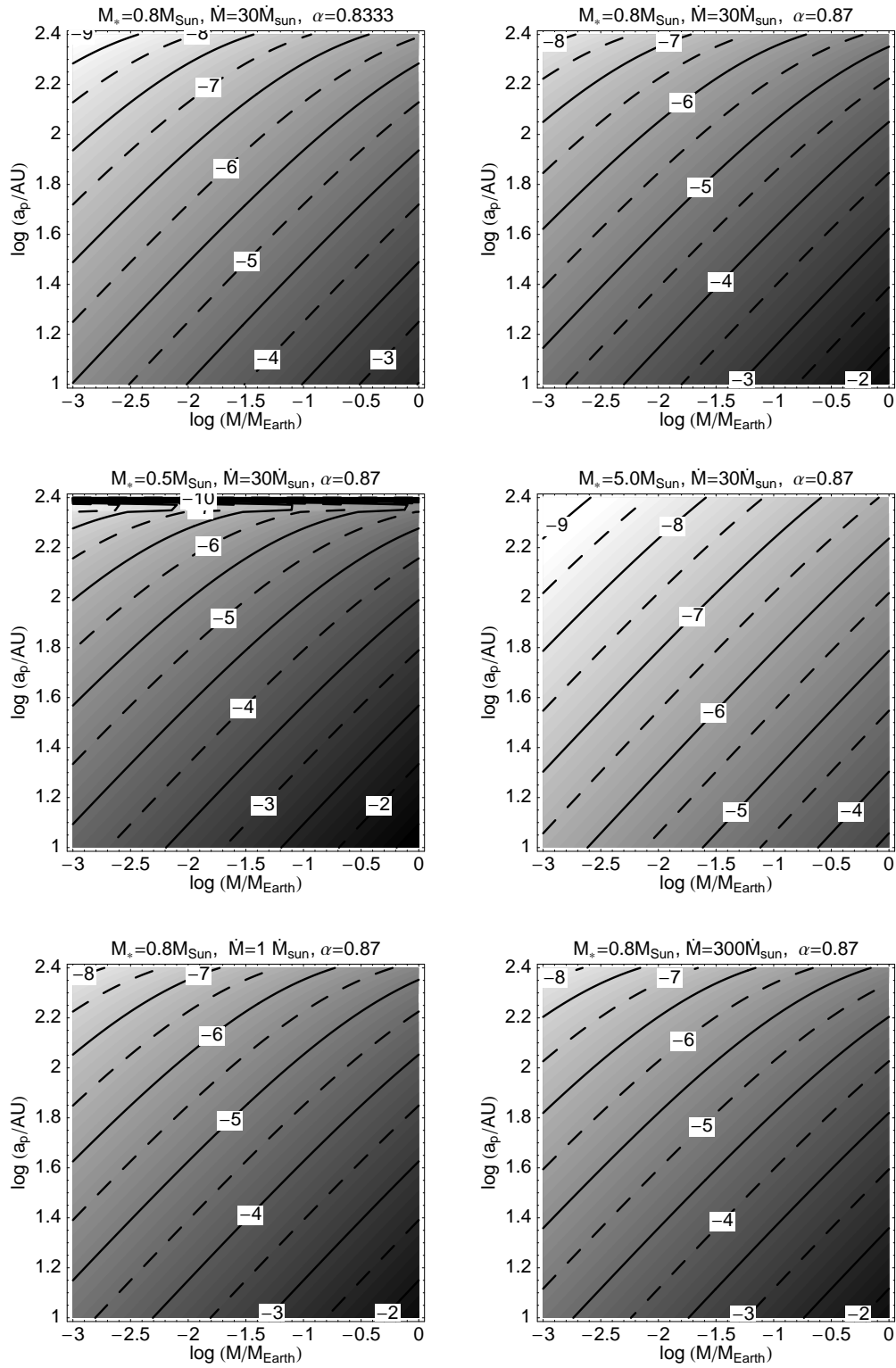
Figure 4.18: Same as Fig. 4.17, but for a 3:2 resonance of a 0.1 Jupiter mass planet each. Top left and right: Dohnanyi's $\alpha = 0.833$ and more realistic $\alpha = 0.87$, both for the same stellar properties. Middle left and right: Two different stellar masses of 0.5 and $5.0 M_\odot$, respectively, for same $\dot{M}_*$ and α. Bottom left and right: Two mass-loss rates of $\dot{M}_* = 1 \dot{M}_\odot$ and $\dot{M}_* = 300 \dot{M}_\odot$, respectively, for same M_* and α.

We consider two cases now: first a star of low activity, e.g. the Sun. There the stellar wind can be neglected and we get an approximation for τ as was found in Krivov et al. (2007),

$$
\begin{aligned}
\tau \;\lesssim\;\; & 4.3 \cdot 10^{-5} \left(\frac{\hat{S}}{0.2}\right)^{-1} \left(\frac{e_{\max}}{0.2}\right)^{-1} \\
\times \;\; & \left(\frac{s_{\max}}{10\ \mathrm{km}}\right)^{-0.39} \left(\frac{\mathfrak{M}}{0.1 M_{\oplus}}\right) \\
\times \;\; & \left(\frac{M_p}{M_J}\right)^{0.31} \left(\frac{M_*}{M_{\odot}}\right)^{-2.14} \left(\frac{a_p}{100\ \mathrm{AU}}\right)^{-2} \left(\frac{p}{p+q}\right)^{4/3}.
\end{aligned} \tag{4.87}
$$

Herein the star's luminosity was replaced with $L_* \propto M_*^4$, for simplicity.

The second case is an active star for which the stellar wind can be of the same order as PR drag. Therefore we have to consider the full (4.86). The approximated optical depth does not depend on the luminosity alone anymore but on the mass-loss rate $\dot{M}_*$ also. Unfortunately the latter cannot be quantified via the stellar mass and remains in the resulting formula for τ,

$$
\begin{aligned}
\tau \;\lesssim\;\; & 4.3 \cdot 10^{-5} \left(\frac{\hat{S}}{0.2}\right)^{-1} \left(\frac{e_{\max}}{0.2}\right)^{-1} \\
\times \;\; & \left(\frac{s_{\max}}{10\ \mathrm{km}}\right)^{-0.39} \left(\frac{\mathfrak{M}}{0.1 M_{\oplus}}\right) \\
\times \;\; & \left(\frac{M_p}{M_J}\right)^{0.31} \left(\frac{M_*}{M_{\odot}}\right)^{-2.14} \left(1 + 4 \cdot 10^{-4}\, \frac{\dot{M}_*}{\dot{M}_{\odot}}\, \frac{L_{\odot}}{L_*}\, \frac{v_{\mathrm{wind}}}{400 km/s}\right)^{-1} \\
\times \;\; & \left(\frac{a_p}{100\ \mathrm{AU}}\right)^{-2} \left(\frac{p}{p+q}\right)^{4/3}.
\end{aligned} \tag{4.88}
$$

All the dependencies seen in Eqs (4.87) and (4.88) can be retraced easily in Figs 4.17 and 4.18.

4.2.6   Simplifications

The additional simplifications for scenario II all concern the modelling of the collisional cascade. That is the central task and most crucial point here.

First we determined u_{crit} by numerical experiments for only the 3:2 resonance, thus we have no information about any p or q dependence. For any set of (M_*, M_p) we had 100 particles only and therefore the numerical noise and resulting error are large. They become even greater due to the very simple power law fit when determining u_{crit} from the u_{eject}.

Later, when considering the loss of material during the cascade, $1 - \Psi$, we take into consideration the final collision only. For the reasons given above that error will be a few percent. According to Nakamura & Fujiwara (1991) the mean velocity of the fragments is $\sim m_{\mathrm{target}}^{-1/6}$, thus $1 - \Psi$ will be much smaller for earlier collisions with larger particles.

We also use only one value for u_0 and γ. In physical systems they will depend on the material, porosity, the mass of the colliders and the collisional velocity. The latter, for example, is proportional to the Keplerian velocity and thus also dependent on the semimajor axis. We do not adjust the slope α of the size distribution when going from $s_{\max}$ to $s_{\min}$, although Durda & Dermott (1997) suggest that this would be necessary.

Finally we assumed a steady state for the colliding, resonant ensemble. We thus ignore that pronounced clumpy structures can also be produced by a so called 'supercollision', meaning the collision and break-up of two very large bodies in the circumstellar disc, (e.g. Wyatt & Dent, 2002; Grigorieva et al., 2007). Kenyon & Bromley (2005) showed that the debris cloud of such a collision is dispersed into a symmetric ring after $\sim 10^4$ years, which is about 35 orbits for the outer planet $a_p = 40 AU$ at ϵ Eridani.

Some smaller simplifications appear in the approximations for $m_{\min}/m_{\max} \ll 1$ in the derivation of the swarm cross section Σ, the choice of a single clump size S and single maximum eccentricity $e_{\max}$.

4.3   Summary

In this chapter we constructed and compared two scenarios aiming to explain clumpy structures in resonant circumstellar discs. Scenario I was transport driven and depended on the optical thickness of the nonresonant background disc, scenario II was collision driven, depending on the amount of dust parent bodies residing in the resonance.

In scenario I the optical depth of the clumps is a function of that of the background, depending heavily on the star's mass-loss rate. This is an observational value, which is only poorly determined and thus a large source of uncertainty for that model, if we want to explain structures of observed discs. We found that around a large star of low mass-loss rate this scenario can create clumps in spite of collisions in discs with a thickness of $\tau_0 \sim 10^{-6}$. For higher mass-loss rates the transport and pumping is more efficient and thus the scenario works for denser discs also. Independent of circumstances, the clumps' thickness is only 10% to 30% of that of the background.

In scenario II the clumps' optical thickness is independent of the background. It depends, however, on the applied cascade model. The dependence on the distance to the star is much stronger than for scenario I, for any set of parameters chosen. There even exists a critical distance a_{crit} where $\tau \equiv 0$. Although the quantitative influence, especially of M_*, M_p or $(p+q) : p$ is strong, there are no qualitative differences there.

If there were a resonant planetesimal population of $10\% M_{\oplus}$ around either the Sun or ϵ Eridani it would produce clumps of $\tau \sim 10^{-4}$ for both stars. That means the influences of the different mass and mass-loss rate annihilate each other.

If we assume a total mass of Plutinos in the Kuiper Belt of approximately $10 M_{\mathrm{Pluto}}$ (following the analysis of Iorio (2007), who found approximately 2% $M_{\oplus}$ of resonant Kuiper Belt Objects), and adjusting the diameter of the largest planetesimal to $s_{\max} \sim$

s_{pluto}, scenario II an optical thickness of the clumps of $\tau \sim 1 \cdot 10^{-6}$. Which results in a brightness difference of about 20% with optical depth of $\tau_0 \sim 10^{-6}$ estimated from dust measurements. The objects of Pluto's size, however, are statistically decoupled. They are too few in number to fit into the kinetic model. If we instead consider the smaller, still coupled, planetesimals and use $s_{\mathrm{max}} = 10 km$, again, we get resonant clumps of the same optical thickness with a total mass of about one Pluto mass or $1.5 \cdot 10^{-3} M_{\oplus}$, respectively, in that size range.

Some quantitative uncertainties of both observations and models not withstanding we are able to explain resonant structures for a large variety of stars and discs in an easy and straigthforward way.

Chapter 5

Conclusion & Outlook

Der Kosmos ist zwar das beständigste unter allen Dingen, diese Beständigkeit umfaßt aber nicht die Lehre, die seiner Erforschung dient.

STANISLAW LEM [1]

5.1 Conclusions

In this work we examined structures in circumstellar debris discs induced by an embedded planet. In doing so, we successfully combined the effects of a mean motion resonance between the planet and disc particles with the effects of mutual collisions among the particles. To achieve this we applied the method of kinetic theory to celestial mechanics.

In the first part we investigated the velocities and rates of mutual collisions of disc particles within a resonance by computing both from distributions of the orbital elements. This way we obtained the collisional velocity and rate as functions of the eccentricities, depending on the integers p and q of the $(p+q) : q$-resonance as well as the libration width A as free parameters.

The collisional velocity V_{imp} is found to be influenced by the resonance very only slightly. For subsets of disc particles with orbital eccentricities $e = e_1$ and $e = e_2$, the collisional velocity $V_{\mathrm{imp}}(e_1, e_2)$ is smallest if $e_1 = e_2$, as expected. It is maximal for collisions between particles with a low and a medium eccentricity. Averaged over both eccentricities from 0 to e_{max}, $V_{\mathrm{imp}}(e_{\mathrm{max}})$ represents the collisional velocity of the whole ensemble of particles with an allowed maximum eccentricity of $e = e_{\mathrm{max}}$. It is almost linear over the whole range of eccentricities. The most remarkable feature is that for small eccentricities $e_{\mathrm{max}} \lesssim 0.4$ the resonance slightly *lowers* the collisional velocity, in contradiction to heuristic arguments, which rather predict a rise here. In all cases considered $V_{\mathrm{imp}}(e_{\mathrm{max}})$ was $\sim e_{\mathrm{max}} \, v_{\mathrm{kepler}}$.

The collisional rate R is more strongly influenced by the resonances, generally having a highly nonlinear dependence on the particles' eccentricities. While the rate $R(e_1, e_2)$ of

---

[1]in: Franz Rottensteiner (Ed.): Quarber Merkur, Suhrkamp, 1979, pp. 33

two sub-ensembles is constant in the nonresonant case (with exception of some small corrections for high eccentricities), it develops a pronounced maximum with growing strength of the resonance, i.e. with decreasing libration width. This means, most notably, that higher eccentricities do not necessarily lead to higher collisional rates. It are rather the intermediate eccentricities for which collisions are most frequent. The maximum of the collisional rate is the more pronounced, the smaller the libration width A is. For a strong resonance, e.g. $A = 0.1\pi$, the collisional rate at its maximum is almost 4 times higher than out of resonance (for 2:1 resonance, at $e_1 = e_2 = 0.38$). The collision rate of the whole disc $R(e_{\max})$, i.e. $R(e_1, e_2)$ averaged over both e_1 and e_2 from 0 to $e_{\max}$, still shows that maximum. It is now somewhat lower than in the unaveraged case: for the same resonance and same libration width the maximum rate is only twice the nonresonant one. As was depicted in Fig. 3.10, increasing the parameter p shifts the maximum of the collisional rate inwards to smaller $e_{\max}$, but does not alter its height. Changing the parameter q, i.e. the order of the resonance, alters both position and height of the maximum. If we increase q – while p is kept fixed – the maximum shifts outwards to larger $e_{\max}$ and at the same time becomes lower. For example, if R_0 is the collisional rate in the nonresonant case and $q = 1$, then the maximum of the rate is $R = 1.87 R_0$ and located at $e_{\max} = 0.23$. If, however, $q = 5$ then the maximum is only $R = 1.13 R_0$ and appears at $e_{\max} = 0.54$ ($p = 3$, $A = 0.1\pi$ in both cases).

The most dramatic influence of a resonance is seen in the case of Trojans ($p = 1, q = 0$). While the velocity is – as in any other case – only changed weakly, the collisional rate rises steeply for strengthening resonance. For $e_{\max} \to 0$ it formally goes to infinity.

All things considered, the collisional behaviour of a resonant debris disc is not very different from that of a nonresonant disc in most cases. The results obtained for collisions in nonresonant, rotationally symmetric discs can be adapted easily to resonant ones.

In the second part of the work we constructed two scenarios aiming to explain the origin of resonant structures. All structures are labelled 'clumps' in general for simplicity. Both scenarios require a planet, which induces resonances in the circumstellar debris disc. And in both of them analytic models are used. They contain the most important effects, but are at the same time kept as simple as possible for this problem. In application to certain planetary systems we found, that the observational and experimental data nowadays available are not sufficient to allow a clear distinction between the two scenarios in the interpretation of the observed structures in debris discs. However, our modelling enables us to explain resonant structures for a variety of stars and discs in a straightforward way.

Scenario I is transport-driven. Here the drag forces of Poynting-Robertson effect and stellar wind bring already existing dust grains to resonant locations, where they are captured into resonance with a certain probability. The dust is assumed to be produced far from the resonance, in a planetesimal belt etc. and not considere here. The properties of the clumps, including their optical depth, are determined by the optical depth of the background disc. The other parameters such as the resonant capture probability and

strength of the stellar wind (especially the mass-loss rate of the star) also influence the efficiency of clump formation heavily.

Scenario I works best for dilute discs around stars with low mass-loss rates. Although for denser discs and higher mass-loss rates the particles might still be captured into resonance, the collisions happen so fast and shorten the lifetime so much, that the resonant dust grains do not develop perceptible eccentricities. In these cases the resonant ensemble cannot form clumpy structures but forms a thin, bright ring. We find that the collisional timescales of the resonant ensemble hardly depend on the size of the particles, but have a power law dependence on the optical depth of the background disc. In dilute discs, i.e. for low optical depth, the drag and resonant pumping timescales are faster than the collisional ones for any set of parameters. Here scenario I will create pronounced clumps. For a denser debris disc, collisions take over and smear the clumps out. The position of that turning point depends on the luminosity and mass-loss rate of the star as well as the grain size and probability of capture of the dust grain into resonance.

Scenario II is collision-driven. Here a number of larger bodies resides in the resonance. Their way into the resonance is not considered here. They might have been placed there e.g. by an earlier planet migration. These larger, resonant bodies collide amongst each other and break up in a cascade-like process. This way the dust is produced already within the resonance. In contrast to scenario I the actual dust production is considered here. To quantify the amount of produced dust we describe the velocities and size distributions of the fragments. We consider the loss of material from the resonance by radiative blow-out as well as by collisional scattering and construct a model for the collisional cascade.

Scenario II works best in discs with a considerable number of resonant dust parent bodies available, i.e. where there is a well populated, resonant planetesimal belt. In this model the optical depth of the resonant structures does not depend on that of the background disc or any timescales. It is instead proportional to the mass of available dust parent bodies.

In this scenario the model for the collisional cascade has a strong influence on the efficiency of clump formation. The influence of assumed collisional velocity or material strength of the colliders, however, is minor.

Application of scenarios I and II to the debris disc host star ϵ Eridani shows that we cannot clearly determine which of the two scenarios is responsible for the clumps. With the available data both are able to explain the observed structures. In scenario I a background optical depth of the observed value of $\tau_0 \sim 10^{-4}$ leads to an enhancement of that optical depth of 25% in the presence of clumps. Equally dense clumps can be created by scenario II with a planetesimal mass in resonance of $\sim 0.1 M_\oplus$, which is reasonable for a debris disc with a size and optical depth like that of ϵ Eridani.

Applying both scenarios to the Solar System, the result is similar. Assuming about ten Pluto masses in Pluto-sized bodies residing in the Plutino group (3:2 resonance with Neptune) of the Kuiper Belt scenario II produces a clump optical depth of $\tau \approx 1 \cdot 10^{-6}$,

which is of the same order of magnitude as that of the background disc, $\tau_0 \sim 10^{-6}$, estimated from dust measurements. For such a background scenario I creates resonant clumps which are not quite as dense as those by scenario II, $\tau \approx 8 \cdot 10^{-7}$. As it is already difficult to quantify by observations the background τ_0 itself, it is impossible so far to measure such small differences between the background disc and resonant structures. Comparing the efficiencies and predictions of scenarios I and II both of them could be at work in the Kuiper Belt of our Solar System.

5.2   Outlook

In future the kinetic model of a colliding, resonant disc shall be refined by using more realistic distributions for the orbital elements. For example, the eccentricity distribution of asteroid populations in the Solar System is known to be far from uniform, it rather peaks near e_{max}. Effects of a three dimensional motion should also be considered. However, to do so a considerable portion of the analytic calculations has to be replaced by numerical ones, since in a full 3D formulation the collision condition has implicit solutions only.

The – in all likelihood – oversimplified models in scenario I and II shall be made more realistic. Scenario I would benefit from a size-dependent particle distribution, $n(s)$. This is because the smaller the particles are, the brighter they are. And because most destructive collisions take place between particles of similar but not quite identical size. A more realistic capture probability, depending then on particle size, planet mass and so on, would allow more realistic settings for the other parameters of the model, too.

In scenario II, use shall be made of the results of Durda & Dermott (1997) by inserting a size dependent slope $\alpha(s)$ in the size distribution, so that the larger particles are no longer underestimated in number and mass. The particles ejected and blown out of the resonance have to be considered. One has to check, if they are removed fast enough so that they really do not contribute to the clumps' optical depth at all.

With the inclusion of these refinements, however, we will have to leave behind the simple analytic structure of our models which we were aiming at in the first place.

Bibliography

Absil, O., di Folco, E., Mérand, A., et al., Circumstellar material in the Vega inner system revealed by CHARA/FLUOR, Astron. Astrophys., 452, 237. 2006

Arakawa, M., Maeno, N., Higa, M., Iijima, Y.-i., & Kato, M., Ejection velocity of ice impact fragments, Icarus, 118, 341. 1995

Augereau, J. & Beust, H., The AU Mic debris ring. Density profile and dynamics of the dust, Astron. Astrophys., 455, 987. 2006

Augereau, J.-C., in ASP Conf. Ser. 321: Extrasolar Planets: Today and Tomorrow, 305–316, 2004

Aumann, H. H., Beichman, C. A., Gillett, F. C., et al., Discovery of a shell around Alpha Lyrae, Astrophys. J., 278, L23. 1984

Beaugé, C. & Ferraz-Mello, S., Capture in exterior mean-motion resonances due to Poynting-Robertson drag, Icarus, 110, 239. 1994

Beichman, C. A., Bryden, G., Gautier, T. N., et al., An Excess Due to Small Grains around the Nearby K0 V Star HD 69830: Asteroid or Cometary Debris?, Astrophys. J., 626, 1061. 2005

Beichman, C. A., Bryden, G., Rieke, G. H., et al., Planets and IR excesses: Preliminary results from a Spitzer/MIPS survey of solar-type stars, Astrophys. J., 622, 1160. 2005

Benz, W. & Asphaug, E., Catastrophic Disruptions Revisited, Icarus, 142, 5. 1999

Bouwman, J., Lawson, W. A., Dominik, C., et al., Binarity as a Key Factor in Protoplanetary Disk Evolution: Spitzer Disk Census of the η Chamaeleontis Cluster, Astrophys. J., 653, L57. 2006

Burns, J. A., Lamy, P. L., & Soter, S., Radiation forces on small particles in the Solar System, Icarus, 40, 1. 1979

Campo Bagatin, A., Cellino, A., Davis, D. R., Farinella, P., & Paolicchi, P., Wavy size distributions for collisional systems with a small-size cutoff, Planet. Space Sci., 42, 1079. 1994

Chiang, E. I. & Jordan, A. B., On the Plutinos and Twotinos of the Kuiper Belt, Astron. J., 124, 3430. 2002

Davis, D. R. & Farinella, P., Collisional Evolution of Edgeworth-Kuiper Belt Objects, Icarus, 125, 50. 1997

Decin, G., Dominik, C., Malfait, K., Mayor, M., & Waelkens, C., The Vega phenomenon around G dwarfs, Astron. Astrophys., 357, 533. 2000

Deller, A. T. & Maddison, S. T., Numerical Modeling of Dusty Debris Disks, Astrophys. J., 625, 398. 2005

Dell'Oro, A., Marzari, P. P. F., Dotto, E., & Vanzani, V., Trojan collision probability: a statistical approach, Astron. Astrophys., 339, 272. 1998

Dell'Oro, A. & Paolicchi, P., Statistical properties of encounters among asteroids: A new, general purpose, formalism, Icarus, 136, 328. 1998

Dermott, S. F., Jayaraman, S., Xu, Y. L., Gustafson, B. A. S., & Liou, J.-C., A circumsolar ring of asteroidal dust in resonant lock with the Earth, Nature, 369, 719. 1994

Dohnanyi, J. S., Collisional model of asteroids and their debris, J. Geophys. Res., 74, 2531. 1969

Durda, D. D. & Dermott, S. F., The collision evolution of the asteroid belt and its contribution to the zodiacal cloud, Icarus, 130, 140. 1997

Everhart, E., Implicit single-sequence methods for integrating orbits, Celest. Mech. Dynam. Astron., 10, 35. 1974

Everhart, E. 1985, in Dynamics of Comets: Their Origin and Evolution, ed. A. Carusi & G. B. Valsecchi (Dordrecht, Reidel), 185–202

Fiedler, S., Multiplanetensysteme und Staubscheiben (Diplomarbeit), 2007

Fitzgerald, M. P., Kalas, P. G., Duchêne, G., Pinte, C., & Graham, J. R., The AU Microscopii Debris Disk: Multiwavelength Imaging and Modeling, Astrophys. J., 670, 536. 2007

Freistetter, F., Krivov, A. V., & Löhne, T., Planets of β Pictoris revisited, Astron. Astrophys., 466, 389. 2007

Gallardo, T., Atlas of the mean motion resonances in the Solar System, Icarus, 184, 29. 2006

Giblin, I., Martelli, G., Farinella, P., et al., The Properties of Fragments from Catastrophic Disruption Events, Icarus, 134, 77. 1998

Gladman, B., Michel, P., & Froeschlé, C., The Near-Earth Object Population, Icarus, 146, 176. 2000

Gold, T., Resonant orbits of grains and the formation of satellites, Icarus, 25, 489. 1975

Greaves, J. S., Holland, W. S., Jayawardhana, R., Wyatt, M. C., & Dent, W. R. F., A search for debris discs around stars with giant planets, Mon. Not. Roy. Astron. Soc., 348, 1097. 2004

Greaves, J. S., Holland, W. S., Moriarty-Schieven, G., & Jenness, T. e., A dust ring around ϵ Eridani: Analog to the young Solar system, Astron. Astrophys., 506, L133. 1998

Greaves, J. S., Holland, W. S., Wyatt, M. C., et al., Structure in the ϵ Eridani Debris Disk, Astrophys. J., 619, L187. 2005

Greenberg, R., Orbital interactions: A new geometrical formalism, Astron. J., 87, 184. 1982

Grigorieva, A., Artymowicz, P., & Thébault, P., Collisional dust avalanches in debris disks, Astron. Astrophys., 461, 537. 2007

Guenther, D. B. & Demarque, P., The stellar seismology of epsilon Eridani, Astrophys. J., 301, 207. 1986

Hatzes, A. P., Cochran, W. D., McArthur, B., et al., Evidence for a Long-Period Planet Orbiting ε Eridani, Astrophys. J., 544, L145. 2000

Heap, S. R., Lindler, D. J., Lanz, T. M., et al., STIS Coronagraphic Observations of Beta Pictoris, Astrophys. J., 539, 435. 2000

Holland, W. S., Greaves, J. S., Zuckerman, B., et al., Submillimetre images of dusty debris around nearby stars, Nature, 392, 788. 1998

Iorio, L., Dynamical determination of the mass of the Kuiper Belt from motions of the inner planets of the Solar system, Mon. Not. Roy. Astron. Soc., 375, 1311. 2007

Jackson, A. A. & Zook, H. A., A solar system dust ring with the Earth as its shepherd, Nature, 337, 629. 1989

Jancart, S., Lemaitre, A., & Letocart, V., The Role of the Inclination in the Captures in External Resonances in the Three Body Problem, Celest. Mech. Dynam. Astron., 86, 363. 2003

Jewitt, D. C., Submillimeter constraints on dust near Lindroos' POST T Tauri stars, Astron. J., 108, 661. 1994

Kadono, T., Arakawa, M., & Mitani, N. K., Fragment velocity distribution in the impact disruption of thin glass plates, Physical Review E, 72, 045106. 2005

Kalas, P., Deltorn, J.-M., & Larwood, J., Stellar encounters with the β Pictoris planetesimal system, Astrophys. J., 553, 410. 2001

Kalas, P., Liu, M. C., & Matthews, B. C., Discovery of a large dust disk around the nearby star AU Microscopii, Science, 303, 1990. 2004

Kenyon, S. J. & Bromley, B. C., Prospects for Detection of Catastrophic Collisions in Debris Disks, Astron. J., 130, 269. 2005

Kirkwood, D. 1867, Meteoric astronomy: a treatise on shooting-stars, fireballs, and aerolites (Philadelphia, J. B. Lippincott & co.)

Krivov, A. V., Löhne, T., & Sremčević, M., Dust distributions in debris disks: Effects of gravity, radiation pressure and collisions, Astron. Astrophys., 455, 509. 2006

Krivov, A. V., Mann, I., & Krivova, N. A., Size distributions of dust in circumstellar debris disks, Astron. Astrophys., 362, 1127. 2000

Krivov, A. V., Queck, M., Löhne, T., & Sremčević, M., On the nature of clumps in debris disks, Astron. Astrophys., 462, 199. 2007

Krivov, A. V., Sremčević, M., & Spahn, F., Evolution of a Keplerian Disk of Colliding and Fragmenting Particles: A Kinetic Model and Application to the Edgeworth-Kuiper Belt, Icarus, 174, 105. 2005

Kuchner, M. J. & Holman, M. J., The Geometry of Resonant Signatures in Debris Disks with Planets, Astrophys. J., 588, 1110. 2003

Kuchner, M. J., Reach, W. T., & Brown, M. E., A Search for Resonant Structures in the Zodiacal Cloud with COBE DIRBE: The Mars Wake and Jupiter's Trojan Clouds, Icarus, 145, 44. 2000

Lagrange, A.-M., Backman, D. E., & Artymowicz, P., in Protostars and Planets IV, ed. V. Mannings, A. P. Boss, & S. S. Russell (University of Arizona Press, Tucson), 639–672, 2000

Lazzaro, D., Sicardy, B., Roques, F., & Greenberg, R., Is there a planet around beta Pictoris? Perturbations of a planet circumstellar dust disk. 2: The analytical model, Icarus, 108, 59. 1994

Lecavelier des Etangs, A., Scholl, H., Roques, F., Sicardy, B., & Vidal-Madjar, A., Perturbations of a Planet on the beta Pictoris Circumstellar Dust Disk. 3. Time scale of collisional destruction versus resonance time scale, Icarus, 123, 168. 1996

Liou, J.-C. & Zook, H. A., Comets as a source of low eccentricity and low inclination interplanetary dust particles, Icarus, 123, 491. 1996

Liou, J.-C. & Zook, H. A., Evolution of interplanetary dust particles in mean motion resonances with planets, Icarus, 128, 354. 1997

Liou, J.-C. & Zook, H. A., Signatures of the Giant Planets Imprinted on the Edgeworth-Kuiper Belt Dust Disk, Astron. J., 118, 580. 1999

Liou, J.-C., Zook, H. A., Greaves, J. S., & Holland, W. S., Does Planet Exist in ε Eridani? A Comparison Between Observations and Numerical Simulations, LPSC XXXI, LPI, Houston, TX, abstract No. 1416, 2000

Liou, J.-C., Zook, H. A., & Jackson, A. A., Orbital Evolution of Retrograde Interplanetary Dust Particles and Their Distribution in the Solar System, Icarus, 141, 13. 1999

Liu, M. C., Substructure in the Circumstellar Disk Around the Young Star AU Microscopii, Science, 305, 1442. 2004

Löhne, T., Krivov, A. V., & Rodmann, J., Long-Term Collisional Evolution of Debris Disks, ArXiv e-prints, 710. 2007

Lovis, C., Mayor, M., Pepe, F., et al., An extrasolar planetary system with three Neptune-mass planets, Nature, 441, 305. 2006

Marcy, G. W., Cochran, W. D., & Mayor, M., Extrasolar Planets around Main-Sequence Stars, Protostars and Planets IV, 1285. 2000

Marzari, F., Scholl, H., & Farinella, P., Collision Rates and Impact Velocities in the Trojan Asteroid Swarms, Icarus, 119, 192. 1996

Marzari, F. & Vanzani, V., Dynamical evolution of interplanetary dust particles, Astron. Astrophys., 283, 275. 1994

Meyer, M. R., Backman, D. E., Weinberger, A. J., & Wyatt, M. C., in Protostars and Planets V, ed. B. Reipurth, D. Jewitt, & K. Keil, 573–588, 2007

Morbidelli, A., Brown, M. E., & Levison, H. F., The Kuiper Belt and its Primordial Sculpting, Earth Moon and Planets, 92, 1. 2003

Moro-Martín, A., Carpenter, J. M., Meyer, M. R., et al., Are Debris Disks and Massive Planets Correlated?, Astrophys. J., 658, 1312. 2007

Mouillet, D., Larwood, J. D., Papaloizou, J. B., & Lagrange, A.-M., A planet on an inclined orbit as an explanation of the warp in the β Pictoris disc, Mon. Not. Roy. Astron. Soc., 292, 896. 1997

Murray, C. D. & Dermott, S. F., Solar System Dynamics (Cambridge Univ. Press), 1999

Nakamura, A. & Fujiwara, A., Velocity distribution of fragments formed in a simulated collisional disruption, Icarus, 92, 132. 1991

Nakamura, A. M., Cratering of asteroids and small bodies, Adv. Space Res., 29, 1221. 2002

Ozernoy, L. M., Gorkavyi, N. N., Mather, J. C., & Taidakova, T. A., Signatures of Exosolar Planets in Dust Debris Disks, Astrophys. J., 537, L147. 2000

Pagano, I., Linsky, J. L., Carkner, L., et al., HST/STIS Echelle Spectra of the dM1e Star AU Microscopii Outside of Flares, Astrophys. J., 532, 497. 2000

Queck, M., Krivov, A. V., Sremcevic, M., & Thebault, P., Collisional Velocities and Rates in Resonant Planetesimal Belts, Celest. Mech. Dynam. Astron.. 2007

Quillen, A. C., Reducing the probability of capture into resonance, Mon. Not. Roy. Astron. Soc., 365, 1367. 2006

Quillen, A. C. & Thorndike, S., Structure in the ϵ Eridani dusty disk caused by mean motion resonances with a 0.3 eccentricity planet at periastron, Astrophys. J., 578, L149. 2002

Raphael, H., The Spectrum of ϵ Eridani, Publ. of the Astron. Soc. of the Pacific, 49, 264. 1937

Reach, W. T., Franz, B. A., Weiland, J. L., et al., Observational Confirmation of a Circumsolar Dust Ring by the COBE Satellite, Nature, 374, 521. 1995

Reche, R., Beust, H., Augereau, J. C., & Absil, O., On the observability of resonant structures in planetesimal disks due to planetary migration, Astron. Astrophys.. 2008, in press.

Reidemeister, M. 2007, Statistik von Resonanzeinfängen (Diplomarbeit)

Rhee, J. H., Song, I., Zuckerman, B., & McElwain, M., Characterization of Dusty Debris Disks: The IRAS and Hipparcos Catalogs, Astrophys. J., 660, 1556. 2007

Safronov, V. S. 1969, Evolution of the Protoplanetary Cloud and Formation of the Earth and Planets (Nauka, Moscow (in Russian). [English translation: NASA TTF-677, 1972]

Saumon, D., Hubbard, W. B., Burrows, A., et al., A Theory of Extrasolar Giant Planets, Astrophys. J., 460, 993. 1996

Smith, B. A. & Terrile, R. I., A circumstellar disk around β Pictoris, Science, 226, 1421. 1984

Smith, K., Güdel, M., & Audard, M., Flares observed with XMM-Newton and the VLA, Astron. Astrophys., 436, 241. 2005

Strom, S. E., Astrophysics - Early Stages of Star Formation, Nature, 364, 99. 1993

Strubbe, L. E. & Chiang, E. I., Dust dynamics, surface brightness profils, and thermal spectra of debris disks: The case of AU Mic, Astrophys. J., 648, 652. 2006

Su, K. Y. L., Rieke, G. H., Misselt, K. A., et al., The Vega Debris Disk – A Surprise from Spitzer, Astrophys. J., 628, 487. 2005

Telesco, C. M., Fisher, R. S., Wyatt, M. C., et al., Mid-infrared images of β Pictoris and the possible role of planetesimal collisions in the central disk, Nature, 433, 133. 2005

Thébault, P. & Doressoundiram, A., Colors and collision rates within the Kuiper belt: Problems with the collisional resurfacing scenario, Icarus, 162, 27. 2003

Thébault, P. & Augereau, J.-C., Collisional processes and size distribution in spatially extended debris discs, Astron. Astrophys., 472, 169. 2007

Thébault, P., Augereau, J.-C., & Beust, H., Dust production from collisions in extrasolar planetary systems. The inner β Pictoris disc., Astron. Astrophys., 408, 775. 2003

Thébault, P. & Brahic, A., Dynamical influence of a proto-Jupiter on a disc of colliding planetesimals, Planet. Space Sci., 47, 233. 1998

Weidenschilling, S. J. & Jackson, A. A., Orbital resonances and Poynting-Robertson drag, Icarus, 104, 244. 1993

Wisdom, J., Chaotic behavior and the origin of the 3/1 Kirkwood gap, Icarus, 56, 51. 1983

Wood, B. E., Müller, H.-R., Zank, G. P., & Linsky, J. L., Measured Mass-Loss Rates of Solar-like Stars as a Function of Age and Activity, Astrophys. J., 574, 412. 2002

Wyatt, M. C., Resonant Trapping of Planetesimals by Planet Migration: Debris Disk Clumps and Vega's Similarity to the Solar System, Astrophys. J., 598, 1321. 2003

Wyatt, M. C., The insignificance of P-R drag in detectable extrasolar planetesimal belts, Astron. Astrophys., 433, 1007. 2005

Wyatt, M. C., Dust in Resonant Extrasolar Kuiper Belts: Grain Size and Wavelength Dependence of Disk Structure, Astrophys. J., 639, 1153. 2006

Wyatt, M. C. & Dent, W. R. F., Collisional processes in extrasolar planetesimal discs — dust clumps, Mon. Not. Roy. Astron. Soc., 334, 589. 2002

Wyatt, S. P. & Whipple, F. L., The Poynting-Robertson effect on meteor orbits, Astrophys. J., 111, 134. 1950

Appendix A

List of Symbols/Units

a	semimajor axis
a_p, a_{res}	planetary, resonant semimajor axis
A	libration width of resonance
α	slope of Dohnahyi distribution
AU	Astronomical Unit, $1.5 \cdot 10^{13} cm$
B	modified β, $B = 2GM_*\beta/(ca^2)$
$\beta_{\mathrm{PR}}, \beta_{\mathrm{wind}}$	PR drag over gravity ratio, stellar wind drag over gravity ratio
β	combination of all drag forces, $\beta_{\mathrm{PR}} + \beta_{\mathrm{wind}}$
c	speed of light, $3 \cdot 10^{10} cm/s$
$\delta(.)$	Dirac delta distribution
$\Delta^{(k)}(.)$	Δ-integral of order k, see Ch. 3
e	numerical eccentricity of the orbit, referred to as 'eccentricity' only
$e_{\mathrm{max}}, e_{\mathrm{res}}$	maximum eccentricity of the ensemble, max. ecc. possible in resonance
ϵ	semi-opening angle of the disc
G	gravitational constant
γ	fracturing exponent of the collisional outcome ($\hat{=}$ material strengh)
h	scale height of disc, $h = 2a \sin \epsilon$
I	intensity (of light, stellar wind)
L_*	stellar luminosity
$L_\odot$	solar luminosity, $4 \cdot 10^{33} erg/s$
λ, λ_p	mean longitude, mean longitude of planet
$\overline{\lambda}$	mean longitude with respect to planet
m	mass of a single particle

$m_{\min}, m_{\max}$	mass of smallest and largest particle within ensemble
M	mean anomaly (angle)
M_*	stellar mass
$\mathfrak{M}$	total planetesimal mass
$M_\odot$	solar mass, $2 \cdot 10^{33} g$
$\dot{M}_*$	stellar mass loss rate
$\dot{M}_\odot$	solar mass loss rate, $2 \cdot 10^{-14} M_\odot/\text{year}$
M_p	planetary mass
$M_J, M_\oplus$	Jupiter mass, $1.9 \cdot 10^{30} g \approx 300 M_\oplus$, Earth mass, $5.9 \cdot 10^{27} g$
$n(.)$	number density of particles
$\dot{n}^+$	drift rate of particles
N	number of particles
$\mathcal{N}$	prefactor of Dohnanyi distribution
ω	argument of pericentre
$\overline{\omega}$	argument of pericentre with respect to planet
p	resonance parameter
pc	parsec = parallactic second, $206\,265 AU$
p_{res}	probability of capture into resonance
$\phi(.)$	normalized density distribution
Φ, Φ_0	resonant argument, centre of libration
Ψ	kept fraction of material after coll. cascade
q	resonance parameter, order of the resonance
r	distance circumstellar object - star
$\mathbf{r}$	position vector in real/physical space
$R(.)$	collisional rate
ρ	density of particle
$s, s_{\min}, s_{\max}$	diammetre of particle, minimum, maximum size within ensemble
$S, \hat{S}$	size of resonant clump, size relative to background annulus
S_0	size of background annulus
σ	collisional cross section of single particle
Σ	collisional cross section of swarm of particles
t	time
T	lifetime of particle

$T_{\mathrm{drag}}, T_{\mathrm{res}}$ time to drift through resonance, resonant pumping time

$T_{\mathrm{coll}}, T_{\mathrm{coll}}^0$ collisional lifetime within resonance, with background disc

τ, τ_0 optical depth of resonant clumps, of background disc

θ true longitude

u_{eject} velocity of ejection of individual fragments during collision

u_{crit} critical ejection velocity for staying in resonance

u_0 mean velocity of fragments after collision

v_{kepler} circular Keplerian velocity, $\sqrt{GM_*/a}$

$\mathbf{v}$ velocity vector in real/physical space

V, V_0 interaction volume within resonance, with background disc

Appendix B

Relative Velocity at Collision

Here we give the derivation of the explicit form of $V_{imp}(e_1, \theta_1, e_2)$, Eq. (3.24). Eq. (3.22) is only valid in the individual frame of each particle. To compare two colliding particles the velocity with respect to the inertial frame is needed. For particle #1 this is

$$
\mathbf{v}_1 = \begin{pmatrix} \cos(\overline{\omega}_1 + \theta_1) & -\sin(\overline{\omega}_1 + \theta_1) \\ \sin(\overline{\omega}_1 + \theta_1) & \cos(\overline{\omega}_1 + \theta_1) \end{pmatrix} \cdot \mathbf{v} \tag{B.1}
$$

$$
= \sqrt{\frac{GM}{a(1 - e_1^2)}} \begin{pmatrix} -e_1 \sin \overline{\omega}_1 - \sin(\overline{\omega}_1 + \theta_1) \\ e_1 \cos \overline{\omega}_1 + \cos(\overline{\omega}_1 + \theta_1) \end{pmatrix}, \tag{B.2}
$$

and likewise for particle #2. From now on we will omit the prefactor $\sqrt{GM/a}$ as it is identical for both colliders. The difference (3.23) of both, with the collision condition (3.17) for $\overline{\omega}_2$ inserted, is

$$
\mathbf{v}_1 - \mathbf{v}_2 = \begin{pmatrix} \dfrac{-e_1 \sin \overline{\omega}_1 - \sin(\overline{\omega}_1 + \theta_1)}{\sqrt{1 - e_1^2}} - \dfrac{-\sin(\overline{\omega}_1 + \theta_1) - e_2 \sin(\overline{\omega}_1 + \theta_1 - \theta_2)}{\sqrt{1 - e_2^2}} \\ \dfrac{e_1 \cos \overline{\omega}_1 + \cos(\overline{\omega}_1 + \theta_1)}{\sqrt{1 - e_1^2}} - \dfrac{\cos(\overline{\omega}_1 + \theta_1) + e_2 \cos(\overline{\omega}_1 + \theta_1 - \theta_2)}{\sqrt{1 - e_2^2}} \end{pmatrix}. \tag{B.3}
$$

We replace $\cos \theta_2$ according to (3.18) now and calculate the scalar product of (B.3) with itself, being the square of the norm, i.e. the square of the relative velocity. After thorough arithmetics it can be written as

$$
(\mathbf{v}_1 - \mathbf{v}_2)^2 = \frac{2}{(1 - e_1^2)W} \big[W + e_1^2 W + 2e_1 W \cos \theta_1
$$

$$
- (1 - e_2^2)(1 + e_1 \cos \theta_1)^2 - e_1 e_2 (1 - e_1^2) \sin \theta_1 \sin \theta_2 \big] \tag{B.4}
$$

$$
\text{with } W = \sqrt{(1 - e_1^2)(1 - e_2^2)}. \tag{B.5}
$$

Finally replacing the remaining θ_2 with the solution from Eqs (3.19) and (3.20) and

extracting the root we get the two branched relative velocity of the colliders,

$$
\begin{aligned}
|\mathbf{v}_1 - \mathbf{v}_2|^{\pm} &\equiv V_{imp}^{\pm}(e_1, \theta_1, e_2) \\
&= \left[\frac{2}{(1 - e_1^2)W} \left(W + e_1^2 W + 2e_1 W \cos\theta_1 - (1 - e_2^2)(1 + e_1 \cos\theta_1)^2 \right. \right. \\
&\quad \left. \left. \pm\, e_1 e_2 (1 - e_1^2) \sin\theta_1 \sqrt{1 - \frac{(e_1^2 - e_2^2 + (1 - e_1^2)e_1 \cos\theta_1)^2}{(1 - e_1^2)^2\, e_2^2}} \right) \right]^{1/2}
\end{aligned}
\tag{B.6}
$$

Persönliche Danksagung

Ehrenwörtliche Erklärung

Ich erkläre hiermit ehrenwörtlich, daß ich die vorliegende Arbeit selbständig, ohne unzulässige Hilfe Dritter und ohne Benutzung anderer als der angegebenen Hilfsmittel und Literatur angefertigt habe. Die aus anderen Quellen direkt oder indirekt übernommenen Daten und Konzepte sind unter Angabe der Quelle gekennzeichnet.

Weitere Personen waren an der inhaltlich-materiellen Erstellung der vorliegenden Arbeit nicht beteiligt. Insbesondere habe ich hierfür nicht die entgeltliche Hilfe von Vermittlungs- bzw. Beratungsdiensten (Promotionsberater oder andere Personen) in Anspruch genommen. Niemand hat von mir unmittelbar oder mittelbar geldwerte Leistungen für Arbeiten erhalten, die im Zusammenhang mit dem Inhalt der vorgelegten Dissertation stehen.

Die Arbeit wurde bisher weder im In- noch Ausland in gleicher oder ähnlicher Form einer anderen Prüfungsbehörde vorgelegt.

Die geltende Promotionsordung der Physikalisch-Astronomischen Fakultät ist mir bekannt.

Ich versichere ehrenwörtlich, daß ich nach bestem Wissen die reine Wahrheit gesagt und nichts verschwiegen habe.

Jena, den 07.02.2008

Martina Queck